TECHNISCHE UNIVERSITÄT MÜNCHEN

Fakultät für Chemie

Lehrstuhl für Theoretische Chemie

First-Principles Microkinetic and Computational Screening Study on Doping as a Means to Improve the Deacon Process at RuO$_2$

DISSERTATION

Zhen Yao

Garching bei München, October 2018

TECHNISCHE UNIVERSITÄT MÜNCHEN

Fakultät für Chemie

Lehrstuhl für Theoretische Chemie

First-Principles Microkinetic and Computational Screening Study on Doping as a Means to Improve the Deacon Process at RuO₂

Zhen Yao

Vollständiger Abdruck der von der Fakultät für Chemie der Technischen Universität München zur Erlangung des akademischen Grades eines

Doktors der Naturwissenschaften

genehmigten Dissertation.

Vorsitzender: Prof. Dr. Harald Oberhofer

Prüfer der Dissertation:

1. Prof. Dr. Karsten Reuter

2. Prof. Dr. Ulrich K. Heiz

Die Dissertation wurde am 13.11.2018 bei der Technischen Universität München eingereicht und durch die Fakultät für Chemie am 14.12.2018 angenommen.

All work presented in this dissertation was performed between October 2013 and November 2017 at the Chair of Theoretical Chemistry of the Technische Universität München under the supervision of Prof. Dr. Karsten Reuter.

I confirm that this is my own work and I have documented all sources and material used.

Zhen Yao

October 2018, Munich

Abstract

Chlorine is widely used in many chemical industries which produce HCl as byproduct. For a sustainable operation, recycling HCl back to high purity Cl_2 is therefore mandatory. RuO_2 shows unique activities for the corresponding oxidative Deacon process, i.e. the catalytic oxidation of HCl to chlorine and water ($4HCl + O_2 \rightarrow 2Cl_2 + 2H_2O$). Both experiment and theoretical simulations have long been committed to deepening and elaborating the Deacon reaction mechanism, and to finding solutions to improve the catalyst reactivity. Therefore, our work here focuses on the in-depth mechanistic studies of the Deacon process and its dependence on a possible doping.

We firstly contribute to this endeavor by analyzing the Deacon reaction network on a $RuO_2(110)$ model catalyst with microkinetic simulations. Specific targets are the role of the trench-like surface geometry of $RuO_2(110)$, as well as the identification of the rate-limiting steps under varying operation conditions. For this, we establish microkinetic models by employing both first-principles and empirically determined rate constants. Through comparison, the most reasonable microkinetic model as well as its related rate-determine step is determined.

Next, we start to seek solutions for the improvement of Deacon catalyst on its activity and stability. One possible route to further improve this performance is a deliberate doping of the oxide matrix. We perform a density-functional theory (DFT) based computational screening study over a wide range of transition metal dopants and use a three-dimensional descriptor matrix to evaluate the rate-controlling Cl desorption energy, the dopant surface segregation energy, as well as the dopant stability against precipitation into bulk oxide grains. Our results suggest Cu doping to represent an optimum compromise between stability and catalytic activity enhancement.

Finally, we work toward a Cu-doped $RuO_2(110)$ microkinetic model. Extensive DFT calculations are employed to determine the energy barriers and calculate the rate constants of elementary reaction steps. The reaction mechanism on the modified surface is studied with the formation of several energy diagrams, which are later compared with those over pure $RuO_2(110)$. Through this comparison, we discuss a possible effect of doping on the rate-controlling step.

Zusammenfassung

Chlorgas ist eine der industriell wichtigsten Chemikalien, mit weitgehendem Einsatz vor allem in Industriezweigen, die HCl als Nebenprodukt generieren. Das Recycling von HCl zurück zu hochreinem Cl_2 ist dabei notwendig um eine nachhaltige Operation zu gewährleisten. Die katalytische Oxidation von HCl zu Chlorgas und Wasser erfolgt über den sogenannten Deacon Prozess, für den RuO_2 eine einzigartige Aktivität vorweist. Experimente sowie theoretische Simulationen wurden lange Zeit eingesetzt, um das Verständnis über den Deacon Reaktionsmechanismus zu vertiefen und Lösungen zu suchen um die Katalysatorreaktivität zu verbessern. Diese Arbeit fokussiert auf tiergehende mechanistische Studien des Deacon Prozesses und seiner Abhängigkeit von eingesetzten Dotanden.

Wir beginnen unseren Beitrag zu diesem Bestreben durch eine Analyse des Deacon Reaktionsnetzwerkes auf einem $RuO_2(110)$ Modellkatalysator mithilfe mikrokinetischer Simulationen. Im Speziellen wird die Rolle der graben-ähnlichen Oberflächengeometrie von $RuO_2(110)$ untersucht, sowie raten-bestimmende Schritte unter variierenden operativen Bedingungen. Zu diesem Anlass entwickeln wir mikrokinetische Modelle durch Einsatz von first-principles und empirisch bestimmten Ratenkonstanten. Durch Vergleich ermitteln wir das beste mikrokinetische Modell sowie den entsprechenden ratenbestimmenden Schritt.

Anschließend werden Lösungen zur Verbesserung der Aktivität und Stabilität des Deacon Katalysators gesucht. Eine mögliche Route zur Verbesserung der Leistung ist die Dotierung der Oxidmatrix. Dichtefunktionaltheorie (DFT) basierte Screening Studien werden durchgeführt über eine große Breite an Übergangsmetall-Dotanden. Hierbei wird eine drei-dimensionale Deskriptormatrix eingesetzt um die raten-bestimmende Cl Desorptionsenergie, die Dotanden-Segretationsenergie sowie die Dotandstabilität gegenüber Precipitation zu bulk Oxidkörnern zu bestimmen. Diese Untersuchungen zeigen, dass Cu Dotanden einen optimalen Kompromiss zwischen Stabilität und katalytischer Aktivitäts-Verbesserung darstellen.

Zuletzt werden grundlegende Schritte in Richtung eines microkinetischen Modells für eine Cu-dotierte $RuO_2(110)$ Oberfläche gelegt. First-principles DFT Rechnungen wer-

den eingesetzt um Energiebarrieren und Ratenkonstanten von Elementarschritten zu berechnen. Der Reaktionsmechanismus auf der modifizierten Oberfläche wird im Detail anhand von Energiediagrammen untersucht, inklusive eines direkten Vergleichs zur Energetik auf der reinen RuO_2(110) Oberfläche. Dieser Vergleich deutet einen Wechsel des ratenbestimmenden Schrittes durch die Dotierung an.

TABLE OF CONTENTS

Chapter 1

Introduction

1.1 Research background

Chlorine, as one of the most important chemicals in the world, is essential to the chemical industry as well as to everyday life. Chlorine is a key building block for the manufacturing of crucial industrial chemicals and consumer products. Through its unique chemical properties, chlorine contributes to our quality of life in an exceptional range of ways. To most people, it is well known for cleansing our everyday water, but it is also extensively used in many other fields, including healthcare, construction, transport, food, electronics, textiles, cosmetics, telecommu- nications, and leisure activities. Chlorine also has an important presence in sustain- ability and energy efficiency. The chlorine tree in Figure 1.1 shows dozens of applications of chlorinated products. It is noteworthy that nearly one-third of products do not contain chlorine, but the production of these chlorine-free end materials is highly dependent on chlorine industry.[1,2]
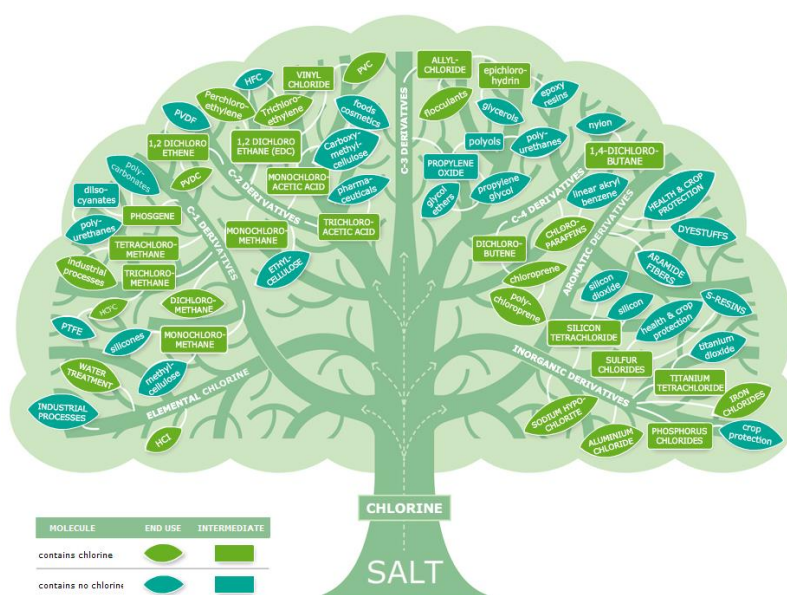

Figure 1.1 The chlorine tree (reproduced with permission of Euro Chlor).[1]

Chlorine is a highly reactive element in its pure form, which practically does not exist as Cl_2 in nature, but it exists in combination with a variety of other forms, and there are also several man-made chlorinated compounds.[3-5] Worldwide, nearly 65 million tons of Cl_2 are produced annually. According to Euro Chlor, which is the European federation representing the chloralkali industry, about 9.1 million tons of chlorine were produced by Europe in 2016, with Germany being the most important stakeholder with more than half of the European production (5.2 million tons). The demand for increasing the chlorine production capacity is highly expected in the coming years. Figure 1.2 shows a summary of the applications of chlorine within Europe in 2016. About two-thirds of chlorine usage was in engineering materials, i.e., polymers, resins, and elastomers. Polyvinyl chloride (PVC) manufacturing constituted the main application of chlorine, closely followed by the preparation of isocyanates and oxygenates.[1,6]

European Chlorine Application (2016)

Total number: 9,135 Kilotonnes

- PVC
- Isocyanates & Oxygenates
- Inorganic
- Other Organic
- Solvents & Epichlorohydrin
- Chloromethanes
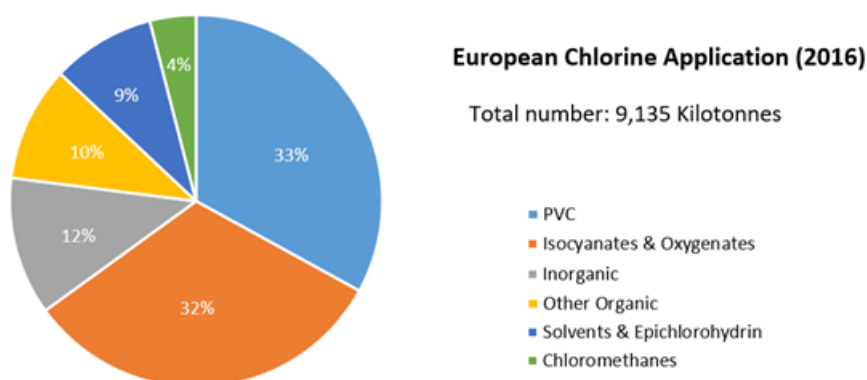
Figure 1.2 European chlorine applications in 2016. Data is obtained from Euro Chlor.[1]

As mentioned above, a large number of Cl_2-derived products do not contain chlorine, such as polyurethanes and polycarbonates, which are representative chlorine-free end materials produced using chlorine chemistry. It can be generally stated that nearly half of the chlorine used in industries ends up forming part of waste byproducts, namely hydrogen chloride (HCl) and chloride salts, during the manufacturing chain.[3,4] Although the byproduct hydrogen chloride gas can be used to produce 35% hydrochloric acid solution or vinyl chloride, its consumption is rather limited. The production of a big amount of byproduct hydrogen chloride has become a serious problem that restricts the development of the chlorine industry. The conversion of waste HCl back to high-purity Cl_2 is therefore highly desirable. As this process is fundamentally important to most industries,[3] and is used extensively throughout the

2

world, even small improvements will have a global economic and environmental impact. Any research breakthrough in chlorine production would be extremely valuable, and this, along with the required research being topical and exciting, motivates our research.

Currently, there are several recycling processes for converting HCl to Cl_2, including electrolysis of HCl,[7-9] direct oxidation of HCl using an oxidizing salt,[10] and catalytic oxidation of HCl.[11,12] The latter is the so-called Deacon process, described as [2]

$$2HCl + \tfrac{1}{2}O_2 \leftrightarrow Cl_2 + H_2O \qquad (\Delta H° = \text{-57 kJ/mol } Cl_2) \qquad (1.1)$$
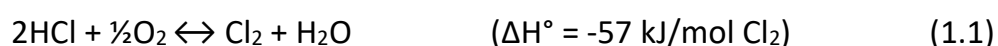
The use of catalysts acts to decrease the energy requirement and with the only byproduct being water, this process is highly sustainable and widely regarded as "green". A range of bulk or supported oxides, and in some cases chlorides of Cu, Cr, Mn, Fe, Ce, Ni and Ru have been used as catalysts in the Deacon process.[3,13-15] However, many of these oxides or chlorides suffer from activity loss and instability. This is due to the corrosive nature of HCl and the volatility of the active metal at process temperatures above 700 K. Bayer[16] and Sumitomo[17] showed that supported RuO_2 catalysts have exceptional stability and improved activity. Due to the improved efficiency, these companies have adopted this new process for Cl_2 production. In our current research, we would investigate and study the mechanistic insights of the RuO_2-based Deacon catalyst to better understand the specific structural and surface electronic properties that contribute to the unique catalytic performance of RuO_2. We hope that, with the aid of our research, a novel Deacon catalyst with better activity and less economic cost will be further designed and developed.

Currently, experimental techniques are always the gold-standard test of a reaction, but they can be expensive and time-consuming. A different insight is nowadays available from a first principles approach, where models of molecular structures are studied by computer simulation. This insight can help us guide the relevant experiments. The combination of these approaches will become the most powerful way forward because, with theoretical-based guidance, experiments will have the maximum likelihood of producing improved catalysts and reactions.

1.2 Current state of research

1.2.1 Previously-established Deacon catalysts

The Deacon process is currently the best available route to convert waste HCl to high-purity Cl_2 (Figure 1.3). Starting with the original HCl oxidation process until the recent times, the industrialization of catalytic HCl oxidation has been hampered by the difficulty to obtain sufficiently active and stable catalysts. Around 1870, the first catalytic process for large-scale Cl_2 production via gas-phase oxidation of hydrogen chloride was established by chemists Henry Deacon and Ferdinand Hurter.[12,18-20] The original Deacon catalyst, $CuCl_2$/pumice, suffered from serious drawbacks and restrict its industrial applications. The disadvantages of using this copper-based catalyst hampered the HCl conversion due to (i) volatilization of the active copper species in the form of chlorides (copper chlorides evaporate at an appreciable rate at temperatures above 673 K); (ii) operational problems such as particle coagulation; and (iii) severe corrosion issues of plant components caused by unreacted HCl in the presence of water. Therefore, the original copper/pumice-based Deacon process has not been commercialised.

With the time coming to the 20th century, the catalytic HCl oxidation continued attracting industrial interest. A later process based on $CuCl_2$-KCl/SiO_2 (Shell-Chlor process) was established by Shell in a fluidised-bed reactor.[13,21,22] Compared to the original Deacon process, the improved stability of this Shell-Chlor catalyst was a result of the molten salt formed by $CuCl_2$-KCl and the lower operating temperature in a fluidised bed in comparison with a fixed bed. Some of the general drawbacks of using copper-based catalysts could be overcome by conducting the chlorination (453-473 K) and oxidation (613-673 K) steps over the $CuCl_2$-KCl catalyst in a circulating dual fluidised-bed reactor system, obtaining nearly full HCl conversion.[3,23] This process reached the pilot scale but was still not commercially utilized probably due to the poor catalyst activity and lifetime.

Later, the Mitsui-Toatsu catalyst (Cr_2O_3/SiO_2) was established by Mitsui Chemicals in a fluidised-bed reactor.[14,24] The stability and low cost of chromium catalyst emphasized a great advantage in comparison with conventional processes. The catalyst operates without melting under the reaction condition (623-673 K). That is, the reaction

proceeds via a redox cycle without going through the chloride-oxide reaction cycle of copper-based catalysts. The process was commercially applied in Japan with a plant that produces 60 kton chlorine per year, but it was discontinued due to the limited installation with only a single plant and environmental concerns associated with the use of chromium metal.[25]

In the last decade of the 20th century, an important breakthrough in catalytic HCl oxidation has been achieved with the development of RuO_2-based materials, i.e. RuO_2/TiO_2-rutile by Sumitomo Chemicals,[17,26] and RuO_2/SnO_2-Al_2O_3 by Bayer.[16,27,28] Their distinctive features are high activity at low temperature and a remarkable stability against (bulk) chlorination. Sumitomo's catalyst was reported to be 50 times more active than Cu, Cr, Fe, Mn, and Ni catalysts, and has been installed for large-scale chlorine recycling (100 kton per year),[2] while Bayer's technology has been successfully piloted and is ready for large-scale manufacturing. Remarkably, the structural properties of the Ru carrier were found to strongly influence the activity and stability of catalyst. The use of bulk, silica, or titania-anatase supported RuO_2 turned out to be either too expensive, or not sufficiently stable under the actual reaction conditions.[29] For example, an examination of RuO_2 supported on SnO_2 showed an unacceptable loss of initial activity (up to 75%) at high temperature, whereas the addition of Al_2O_3 to SnO_2 achieved a stabilizing effect, allowing the catalytic activity to last for several thousand hours.[25]

| Deacon, 1870	Shell, 1960	Mitsui, 1980	Sumitomo, 1999	Bayer, 2006
○ $CuCl_2$/pumice	○ $CuCl_2$-KCl/SiO_2	○ Cr_2O_3/SiO_2	○ RuO_2/TiO_2	○ RuO_2/SnO_2
○ fixed bed	○ fluidised bed	○ fluidised bed	○ fixed bed	○ fixed bed
○ 703-723 K	○ 648-673 K	○ 623-673 K	○ 473-653 K	○ 453-773 K
○ abandoned	○ abandoned	○ commercialised	○ commercialised	○ piloted
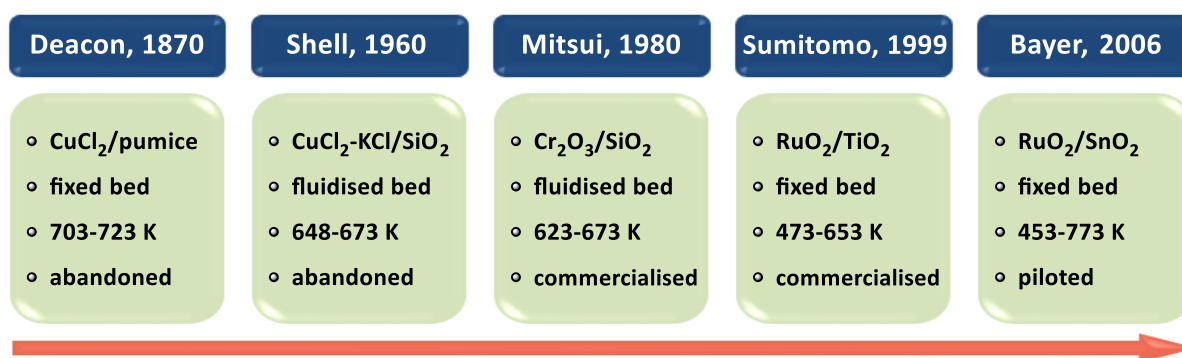
Figure 1.3 Chronological development of Cl_2 production, indicating important milestones from its discovery of Deacon process to present: manufacturing technologies developed to date.[2]

Furthermore, the combination of catalytic and electrolytic technologies for chlorine recycling is also an attractive option.[5] In fact, as processing of the HCl byproduct by

the equilibrium limited Deacon reaction cannot lead to full HCl conversion, the optimized ODC (oxygen-depolarized cathodes)-based electrolysis can complement the catalytic route by fully converting the unreacted HCl to Cl_2.[30,31] We believe that, in the foreseeable future, the design of novel catalysts for HCl oxidation process will still remain an active field of research and satisfy a long-standing industrial need.

1.2.2 Catalytic oxidation of HCl over RuO₂ catalyst

In view of the high potential of RuO_2-based catalytic system, and to prepare the basis for optimization, a solid knowledge of bulk and supported RuO_2 was gathered by means of extensive characterization. Mechanistic and kinetic investigations were carried out following both experimental and theoretical approaches. The well-developed Sumitomo's catalyst is taken as an example to illustrate the unique catalytic performance of RuO_2. The high activity and stability of RuO_2/TiO_2-rutile catalyst was attributed to the "lattice matching" in the film-like growth of RuO_2 on TiO_2-rutile, as opposed to the formation of spherical RuO_2 on TiO_2-anatase. This was depicted using transmission electron microscopy (TEM) images.[2,32] The fact remains that there is little experimental information available on well-defined RuO_2/TiO_2 surfaces, and this emphasizes the need for new insight. Therefore, a first-principles based computational approach with predictive quality proves to be valuable for understanding the mechanism of HCl oxidation reaction over such catalysts.

Density Functional Theory (DFT) studies[4,33] on the catalytic oxidation of HCl over RuO_2(110), the most extended and stable rutile facet, indicated that the reaction starts with the dissociative adsorption of HCl through the surface atomic oxygen, followed by the H removal from HCl, formation of surface water, and recombination of two on-top chlorine atoms on the RuO_2 surface (Figure 1.4). DFT calculations corroborated by experimental techniques[33,34] such as low-energy electron diffraction (LEED) and high-resolution core level shift (HRCLS) attributed the remarkable stability of RuO_2 to the chlorination of the RuO_2 surface through self-limiting replacement of the surface oxygen atom by chlorine. It was shown[34] that the active surface included the chlorine atoms at the bridge positions on the RuO_2(110) surface. The reaction mechanism was

found in several works[33,35,36] to fit a Langmuir-Hinshelwood kinetic model with the recombination of the top-chlorine atoms as the rate-determining step, whereas another study suggested a Mars-van Krevelen mechanism as the catalyst surface undergoes re-oxidation.[4]
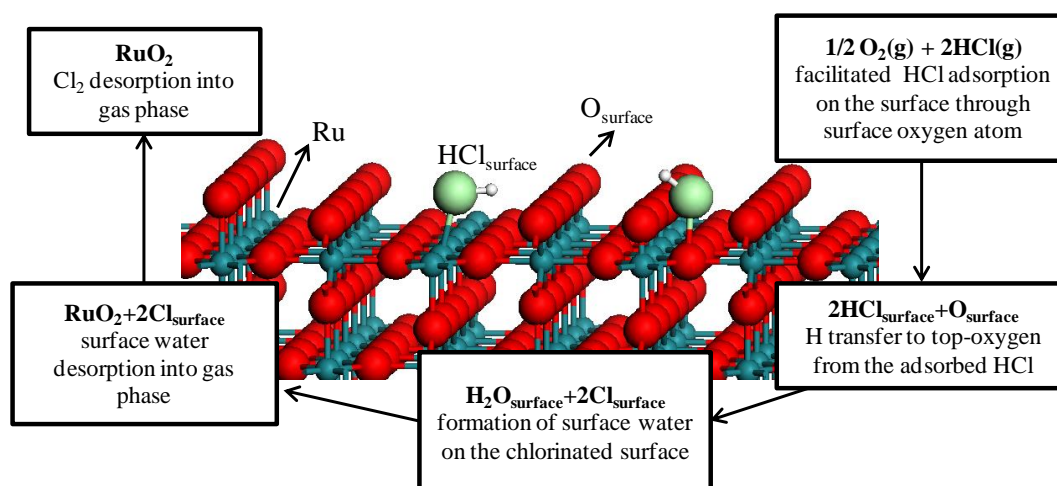
Figure 1.4 The reason for the extraordinary stability of RuO_2 was shown by DFT to be the self-controlling surface chlorination. Several steps are illustrated here for the catalytic oxidation of HCl on the $RuO_2(110)$ surface. (Based on the work by Hess et al.[37])

A recent kinetic study[4] of the HCl oxidation has revealed an enhanced Cl_2 production by increasing the feed ratio of O_2/HCl. It was indicated[29] that dissociative adsorption of HCl required basic sites such as surface oxygen atoms. Since the surface oxygen desorption on $RuO_2(110)$ occurs at temperatures below the actual reaction temperature, the concentration of oxygen atoms on the surface would not be sufficient to dissociate HCl under the reaction conditions. It was therefore suggested that the rate-determining step in the HCl oxidation would instead be the oxygen chemisorption, although the recombination of chlorine was shown to have the highest energy barrier.

A combined DFT and mean-field microkinetic approach[38] compared the activity of a set of rutile transition metal oxides including $RuO_2(110)$, $IrO_2(110)$ and $TiO_2(110)$ for the HCl oxidation reaction. Computational screening of the surfaces under study was performed by defining the dissociative adsorption energy of oxygen on the surface as a descriptor based on the linear energy relations[39] obtained from DFT studies. The

descriptor was employed in the microkinetic modeling of the reaction to provide activity relations for the examined metal oxides. The results indicated that, unlike $RuO_2(110)$, no surface chlorination at the bridge positions occurred on $IrO_2(110)$ and $TiO_2(110)$ surfaces under the reaction condition, pointing to $RuO_2(110)$ being the optimal catalyst out of those considered. The results from this work suggested that metal oxides with "slightly weaker" oxygen bonding to the surface can be more active than RuO_2.

In view of the fact that ruthenium is one of the rarest elements in nature, its high and fluctuating market price becomes the main drawback in utilizing ruthenium as the Deacon process catalyst. Despite the operational advantages of the Ru catalyst, the use of a precious metal is considered as a roadblock for its future widespread use in chlorine production. This issue can be addressed by two main strategies. The first is to find less expensive but comparably stable alternatives to the RuO_2-based catalysts, a promising result of which has been accomplished by the use of CeO_2. With the support of ZrO_2 as carrier, CeO_2 catalyst showed remarkable performance in the HCl oxidation reaction due to its facile oxygen vacancy generation.[40-43] This catalyst has been pilot-tested in technical shape and showed great application prospects. Considering the fact that RuO_2-based Deacon catalysts have been successfully commercialized, the second strategy is to seek a reduction for the amount of ruthenium required and maximize its specific activity. Along this line, a study by Seitsonen et al.[36] revealed that only a thin layer of RuO_2 on TiO_2 support is sufficient to achieve the bulk RuO_2 activity in the Deacon process. Introducing an anionic sub-lattice element such as chlorine into the TiO_2 structure was also shown to facilitate the adsorption of HCl and O_2 onto the surface.[36] These findings may already lead to cost savings by using less RuO_2 in the current commercial process used by Sumitomo. Besides, incorporation of a specific amount of non-precious additives or dopants into RuO_2 may appear as a very promising route, allowing a decrease of Ru catalytic loading while significantly improving the activity and stability of the Deacon catalyst.

1.3 Objectives and outline of the work

This work aims at in-depth mechanistic studies of the Deacon process and its dependence on employed dopant and support. Currently, there is very little information available about a possible effect of doping on the Deacon catalyst activity. In order to fill this gap, a DFT based microkinetic approach will be employed that reliably describes the individual elementary processes and the intricate dependencies within the reaction network. We hope that, with the aid of our research, theoretical modeling and simulations can efficiently and economically guide the design of new Deacon catalysts through doping.

The main content of this thesis is structured into three parts, which are presented in Chapters 3-5.

Chapter 3 shows the microkinetic study of the Deacon reaction on RuO_2(110). With the established microkinetic model, we carried out direct data fitting to limited experimental data and also employed first-principles calculations to calculate the rate constants. Thus, the parameters of the two specific microkinetic models can be obtained using the two above-mentioned methods. Through the comparison of these two sets of models in several aspects, such as fitting with experimental data, surface coverages and wide-range prediction, we finally found the most reasonable microkinetic model and confirmed the rate-determine step as Cl_2 recombination.

Chapter 4 outlines the Deacon reaction on a RuO_2(110) surface modified through dopants. We performed a DFT based computational screening study for a wide range of metal dopant atoms. Based on the results of the previous chapter, we used the rate-controlling Cl desorption energy as a reactivity descriptor. As stability descriptors we employed the dopant surface segregation energy, as well as the dopant thermodynamic stability against precipitation into metal or bulk oxide grains. In the oxygen-rich conditions of the Deacon process, particularly the instability against oxide precipitation represents a strong limitation. In this respect, doping with Cu appears as an optimum compromise between stability and catalytic activity enhancement.

Chapter 5 deals with the establishment of a Cu-doped RuO_2(110) microkinetic model, for which we applied first-principles calculations to calculate the rate constants and obtain the energy barriers of each reaction step. Through the comparison of energy

diagrams of the Deacon process over the Cu-doped $RuO_2(110)$ and pure $RuO_2(110)$ surface, we can determine the rate-controlling step on the modified catalyst surface. Intriguingly, our results indicate a shift in the rate-limiting step upon Cu doping.

As to the other chapters, Chapter 2 introduces the theoretical background of our calculation methods. Chapter 6 is the summary and outlook. Chapter 7 is the appendix part of the thesis.

Chapter 2

Theoretical background

2.1 Density-functional theory (DFT)

DFT is the most crucial and also reliable method for studying chemical reaction models at extended surfaces to date, especially for modeling chemical reactions on heterogeneous catalyst surfaces. As a crucial method for computational quantum mechanical modeling, DFT mainly studies the electronic structure of many-body systems, especially atoms, molecules, and the condensed phases.

Although DFT has its roots in the Thomas-Fermi model for the electronic structure of materials, it was firstly proposed by W. Kohn and P. Hohenberg in the framework of two Hohenberg-Kohn theorems in 1964,[44] and then Kohn and Sham improved the main methods one year later.[45] Since the 1970s, this theory has been widely used for calculations of solid state physics. By the 1990s, the approximation used in the theory has been greatly improved to more accurately simulate the interactions between exchange and correlation. Since DFT calculations in quantum chemistry have always been questioned for their accuracy, the approximation in the theory has been constantly improved and perfected. The following content in part 2.1 is a brief overview of the development of DFT approximation.

DFT addresses the electronic scale. For the stationary state of nuclei and electrons in a physical system, we can describe it with the Schrödinger equation in the Born-Oppenheimer approximation, specifically the time-independent Schrödinger equation.[46] It can be shown as

$$\hat{H}|\psi(r)\rangle = E|\psi(r)\rangle \qquad (2.1)$$

Where E is the electronic energy，$\psi = \psi(r_1, r_2, ..., r_N)$ is the N-electron wave-function, r_i is

the position of the *i* electron, $\hat{H}$ is the Hamiltonian operator (in atomic units):

$$\hat{H} = \sum_{i=1}^{N} \left(-\frac{1}{2} \nabla_{r_i}^2 \right) + \sum_{i=1}^{N} v(r_i) + \sum_{i=1}^{N} \sum_{i<j}^{N} \frac{1}{r_{ij}} \qquad (2.2)$$

Here, *v*(ri) denotes the external potential acting on electron *i*. *v*(r) is usually the potential of nuclear charges.

The most classical method for describing electronic structure is the Hartree-Fock method, which is an approximation for calculating the wave function and the energy of quantum many-body system in stationary states. In the Hartree-Fock method, it is assumed that in the case where the particles are fermions, the exact *N*-body wave function of the system can be approximated by a single Slater determinant of the *N* spin orbits, while in the case of a boson it can be approximated by a single permanent of *N* spin orbitals. Therefore, to find the Hartree-Fock one-electron wave function is now equivalent to solving the eigenfunction equation

$$f(1)\phi_i(1) = \varepsilon_i \phi_i(1) \qquad (2.3)$$

where $f(1)$ is the Fock operator, $\phi_i(1)$ is a set of one-electron wave functions, called Hartree-Fock molecular orbitals, and ε_i is the orbital energy of the molecular orbital $\phi_i(1)$.

An efficient alternative to solving equations 2.1 and 2.2 for multi-electron systems, DFT uses the electronic density instead of the wave function to reduce the original 3*N* variables to three variables, making it more convenient to apply to theoretical concepts and practice.

The theoretical framework of DFT is based on two Hohenberg-Kohn theorems (H-K) proposed by W. Kohn and P. Hohenberg.[44] The first H-K theorem states that the ground state properties of a multi-electron system are uniquely determined by the electron density dependent on three spatial coordinates, while the external potential *v*(r) is determined by the ground-state electron density (ρ) within a trivial additive constant. It is denoted by $E_v[\rho]$ where *v* indicates that this functional depends on the system through the external potential *v*(r). Here, Hohenberg and Kohn introduced a system-independent functional $F^{HK}[\rho]$:

$$F^{HK}[\sigma] = E_v[\rho] - \int \rho(r)v(r)dr \qquad (2.4)$$

The functional $F^{HK}[\rho]$ exists only for v-representable electron densities. We can obtain the energy function according to Equation 2.4:

$$E_v[\rho] = F^{HK}[\sigma] + \int \rho(r)v(r)dr \qquad (2.5)$$

The first Hohenberg-Kohn theorem proves that there is a one-to-one correspondence between the external potential and the ground state density in a multi-electron system. But it gives no form of analysis for the general functional $F^{HK}[\rho]$ or no practical ways to get electron densities of the ground state.

The second Hohenberg-Kohn theorem concerns the latter issue, which defines an energy functional for the system and proves the correct ground state electron density minimizes this energy functional.

Following the first Hohenberg-Kohn theorem, for a correct ground-state electron density $\tilde{\rho}_0$ there exists an associated external potential $\tilde{v}_0$. From $\tilde{v}_0$, Hamiltonian $\tilde{\hat{H}}_0$ and its ground-state wavefunction $\tilde{\psi}_0$ can be constructed. Applying the function $\tilde{\psi}_0$ as a correct function in the variational principle leads to:

$$E_v[\tilde{\rho}_0] = \int \tilde{\rho}_0(r)v_0(r)dr + F_{HK}[\tilde{\rho}_0] < E_v[\rho] \qquad (2.6)$$

It indicates that the density that minimizes the total energy is then the exact ground state density.

The most common application of DFT is realized by the Kohn-Sham method. The intractable many-body problem caused by the interaction of electrons in a static external potential is simplified in the Kohn-Sham DFT [45] as a tractable problem of electrons moving without interaction in an effective potential. The Kohn-Sham formulation centres on mapping the full interacting system with the real potential, onto a fictitious non-interacting system whereby the electrons move within an effective "Kohn-Sham" single-particle potential $v^{KS}(r)$.[45] The Kohn-Sham potential, $v^{KS}(r)$, can be given as

$$v^{KS}(r) = v^{ext}(r) + v^H(r) + v^{XC}(r) \qquad (2.7)$$

Where, $v^H(r)$ is the Hartree potential, and $v^{XC}(r)$ is the exchange-correlation potential.

They can be respectively expressed as follows

$$v^H(r) = \frac{\delta E^H[\rho(r)]}{\delta \rho(r)} = \int \frac{\rho(r')}{\rho(r)} \qquad (2.8)$$

$$v^{XC}(r) = \frac{\delta E^{XC}[\rho(r)]}{\delta \rho(r)} \qquad (2.9)$$

By solving the *N* one-electron Schrödinger equations, we can get the ground state density in the Kohn-Sham method

$$\left[-\frac{1}{2}\nabla^2 + v^{KS}(r) \right] \phi_i(r) = \varepsilon_i \phi_i \qquad (2.10)$$

where ε_i are Lagrange multipliers enforcing the orthonormality of the *N* single-particle states $\phi_i(r)$, and then we can get the density of the non-interacting system

$$\rho(r) = \sum_{i=1}^{N} |\phi_i(r)|^2 \qquad (2.11)$$

The non-interacting kinetic energy $T_s[\rho(r)]$ is therefore given by,

$$T_s[\rho(r)] = -\frac{1}{2}\sum_{i=1}^{N} \int \phi_i^* \nabla^2 \phi_i(r) dr \qquad (2.12)$$

To combine the above equations and define that the density of the non-interacting system is equal to the ground state density of the interacting density, the energy functional is written as

$$F(\rho) = T_s(\rho) + E^H(\rho) + E^{XC}(\rho)$$
$$= -\frac{1}{2}\sum_{i=1}^{N} \int \phi_i^*(r)\nabla^2\phi_i(r)dr + \frac{1}{2}\iint \frac{\rho(r)\rho(r')}{|r-r'|}drdr' + E^{XC}(\rho) \qquad (2.13)$$

The effective potential of KS-DFT includes the influence of external potential and Coulomb interactions between electrons, introduced effectively as exchange and correlation energy (E_{XC}^ρ). It has been known that the treatment of exchange-correlation (E_{XC}^ρ) in KS-DFT is still a big challenge. At present, there is no accurate solution for the exchange-correlation energy E_{XC}. The simplest approximation method is the local density approximation (LDA). The LDA approximates the exchange energy

of the system with the one of a uniform electronic gas (the exchange energy of uniform electronic gas can be accurately solved), while the method of fitting free electronic gas is adopted to deal with the correlation energy.

Here, we can get the XC energy functional of the local density approximation in the non-spin polarization system, which is expressed as follows

$$E_{XC}^{LDA}(\rho) = \int \rho(r)\varepsilon_{XC}^{LDA}(\rho)dr \qquad (2.14)$$

Where ρ is the electronic density and ε_{xc} is the exchange-related energy of each particle of a homogeneous electron gas system corresponding to the charge density ρ.

However, calculations for energy barriers within the LDA are not very accurate.[47]As an improvement, more complex approximation functionals on the basis of the LDA were developed, such as the generalized gradient approximation (GGA) used in our work

$$E_{XC}^{GGA}(\rho) = \int \rho(r)\varepsilon_{XC}^{GGA}(\rho(r), \nabla\rho(r))dr \qquad (2.15)$$

In this dissertation, all calculations are performed by DFT in the plane-wave code CASTEP.[68] In the calculation, the revised GGA functionals PBE [48] and RPBE [49] are applied to deal with electronic exchange and correlation. The interaction between electrons and nuclei is described by ultrasoft pseudopotentials.[69]

2.2 Transition-state theory (TST)

Transition-state theory (TST), also known as absolute rate theory or activated-complex theory,[50] explains the rates of elementary chemical reactions. It assumes a special type of equilibrium, with an equilibrium constant $K^{\ddagger}$, to exist between reactants and activated complexes. This transition-state theory was firstly proposed by Henry Eyring in 1935, and was further developed by M. G. Evans and M. Polanyi.[51,52]

According to this theory, the rate constant is given by

$$k = \frac{k_B T}{h} K^{\ddagger} \qquad (2.16)$$

In which k_B is the Boltzmann constant, and h is the Planck constant.

We introduce the entropy of activation, $\Delta^{\ddagger}S^{o}$, which is the standard molar change of entropy when the activated complex is formed from reactants. The enthalpy of activation, $\Delta^{\ddagger}H^{o}$, is the corresponding standard molar change of enthalpy.

The above rate constant can be expressed as:

$$k = \frac{k_B T}{h} \exp\left(\frac{\Delta^{\ddagger}S^{o}}{R}\right) \exp\left(-\frac{\Delta^{\ddagger}H^{o}}{RT}\right) \qquad (2.17)$$

In thermodynamics, the change in Gibbs free energy, ΔG, is defined as:

$$\Delta G = \Delta H - T\Delta S \qquad (2.18)$$

Then, the equation 2.17 can be also written as

$$k = \frac{k_B T}{h} \exp\left(-\frac{\Delta^{\ddagger}G^{o}}{RT}\right) \qquad (2.19)$$

where $\Delta^{\ddagger}G^{o}$ is the Gibbs energy of activation, which is the standard molar Gibbs energy change for the conversion of reactants into the activated complex.

2.3 Search for transition-state

The transition state is defined as the state corresponding to the highest potential energy along the reaction coordinates. In the path of the reaction between the initial and final arrangement of atoms or molecules, there is an intermediate configuration in which the potential energy has a maximum value. The configuration corresponding to this maximum is called the activated complex, and its state is regarded as the transition state.

One of the challenging difficulties of multi-scale simulation of heterogeneous catalysis based on first-principles is to determine the transition state. In this thesis, we mainly obtain the accurate transition state by the following two methods, which are shown in parts 2.3.1 and 2.3.2.

2.3.1 Nudged-elastic band (NEB)

The nudged elastic band (NEB) is one of the most common methods to find saddle points or the minimum energy path (MEP) when the reactants and products are given. This method is carried out by the optimization of several intermediate images along the reaction path in a constrained manner. In this process, each image finds the lowest possible energy and remains equally spaced from the adjacent image. This constrained optimization is achieved by adding artificial spring forces along the band between images and by projecting out the component of the force due to the potential perpendicular to the band.

In the nudging elastic band NEB method,[53-55] a string of images is created and connected by springs to represent the reaction path from the reactant configuration (R) to the product configuration (P) in discrete form. The NEB calculation can be initiated by an interpolation along the straight line between the reactant, R, and the product, P, to obtain the images. An optimization algorithm is applied to relax the images down towards the MEP.

The string of images can be denoted by [R_0, R_1, R_2, ..., R_N] where R_0 represents the initial state (R) and R_N represents the final state (P). N-1 intermediate images are adjusted by the optimization algorithm and minimized with respect to the intermediate images, R_1, ..., R_N. This simulates an elastic band consisting of N-1 beads and N springs with a spring constant, and the whole band is strung between two fixed endpoints.[56] The images along the NEB are relaxed to the MEP through a force projection scheme in which the potential energy is perpendicular to the band and the spring force is along the band.

Here, for these projections, the tangent along the path $\hat{\tau}$ is defined as the unit vector of the higher energy adjacent image.[57] To avoid the direction from abruptly changing, we use a linear interpolation between vectors in adjacent images at the extremum.

This upward tangent can avoid the artificial kink in the high-force region along the path and thus improve the stability of NEB.[57]

So the NEB force on image i, which contains two independent components, can be written as

$$F_i^{NEB} = F_i^{\perp} + F_i^{S\|} \qquad (2.20)$$

in which $F_i^{\perp}$ denotes the component of the force due to the potential perpendicular to the band,

$$F_i^{\perp} = -\Delta(R_i) + \Delta(R_i) \cdot \hat{\tau}_i \hat{\tau}_i \qquad (2.21)$$

and $F_i^{S\|}$ is the spring force parallel to the band,

$$F_i^{S\|} = k(|R_{i+1} - R_i| - |R_i - R_{i-1}|)\hat{\tau}_i \qquad (2.22)$$

In this final expression, R_i is the position of the image and k is the spring constant.

2.3.2 Linear and quadratic synchronous transit (LST/QST) methods

The use of the linear synchronous transit method (LST) is to search for a maximum along a linear path between reactants and products. The quadratic synchronous transit method (QST) serves as an improvement for the LST approach. QST searches for a maximum along a parabola connecting reactants and products and also for a minimum in all directions perpendicular to the parabola.[58]

In the initial LST method,[59] we obtained the ideal set of structures that connect reactants and products by linear interpolation of the distance between all pairs of atoms of reactants and products. It can be shown as

$$r_{ab}^i(f) = (1-f)r_{ab}^R - fr_{ab}^P \qquad (2.23)$$

Here, r_{ab}^R and r_{ab}^P are the inter-nuclear distances between atoms a and b in the reactant and product, respectively, and f is an interpolation parameter that varies

between 0 and 1. The result excessively specifies the geometry of the system. Therefore, the transit path is defined by using a molecular geometry with inter-atomic distances, which are as close as possible to the ideal values. We can obtain the ideal values by minimizing the below function S

$$S(f) = \frac{1}{2}\sum_{a \neq b} \frac{\left(r_{ab} - r_{ab}^i(f)\right)^2}{\left(r_{ab}^i(f)\right)^4} + 10^{-6} \sum_{\xi = x,y,z} \sum_{a} \left(\xi_a - \xi_a^i(f)\right)^2 \qquad (2.24)$$

in which ξ_a is the actual coordinate, and ξ_a^i is the interpolated Cartesian position of an atom. The function S is always larger than or equal to zero. When $f = 1$ or $f = 0$, this function is minimized by constructing the reactants and products. The maximum estimate of LST can be further improved by minimizing the geometry in the control of the constant p, which can be expressed as below

$$P = \frac{d_R}{d_R + d_P} \qquad (2.25)$$

where d_R is the distance between the reactant and any other geometry of the molecule defined through

$$d_R^2 = \frac{1}{N} \sum_{a} \left(\xi_a - \xi_a^R\right)^2 \qquad (2.26)$$

And d_P can be shown as the similar expression. The obtained geometry (p_m) can be used on its own as an improved guess for the transition state, or the geometry (p_m) can also be carried out for the QST calculation. For the latter case in which the predicted transition state calculated by QST, the energy maximum can be obtained by the quadratic interpolation along reactants, products, and p_m.

LST/QST is a computational algorithm that combines LST and QST to find transition states in the CASTEP program. It performs a single linear synchronous transmission (LST) and then repeats conjugate gradient minimization and quadratic synchronous transmission (QST) maximization until the transition state is found. The flow diagram of this method is shown in Figure 2.1.
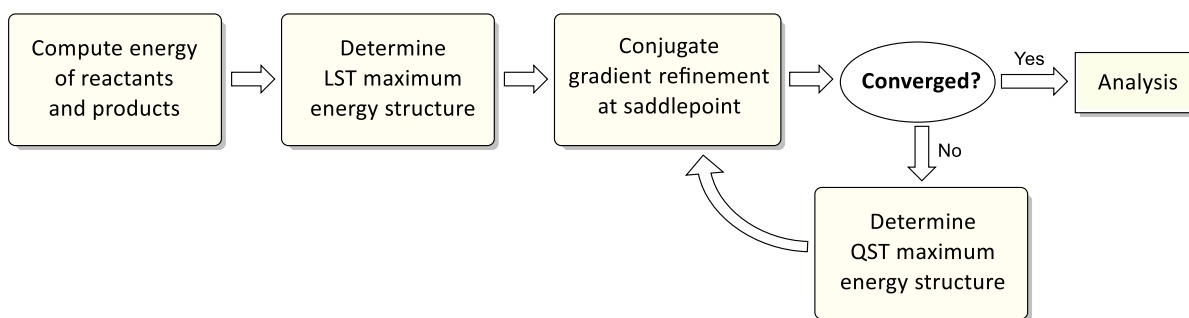
Figure 2.1 Flow diagram of the LST/QST algorithm.

Here, the criterion of convergence is the residual force tolerance specified by the user. "Analysis" indicates that a frequency analysis is conducted in the transition state structure to prove the validity of the transition state structure.[60]

As shown in the figure, we first calculate the energies of reactants and products. According to the two obtained energy points, we search for the maximum along the LST path. Once the maximum value is confirmed, the conjugate gradient (CG) optimization of the structure will be carried out. Subsequently, we need to determine whether the calculation is converged or not. If the residual force is lower than the specified tolerance, it is regarded as converged and can be further analyzed. If not, a new maximum needs to be searched along the QST path connecting reactants, products, and the current optimal transition state structure. In this case, we need to start a new CG optimization loop until we achieve convergence. It is noteworthy that the vibrational spectrum of the predicted transition state structure should have exactly one mode with a negative vibrational frequency ν_{TS} once convergence is reached. Moreover, the corresponding eigenmode shows the direction in which the system following the minimum energy reaction path should develop from the saddle point as the transition state is characterized by saddle points on the energy hypersurface.

Chapter 3

Microkinetics of the Deacon process over RuO$_2$(110) surface

3.1 Introduction

In a standard chemical engineering approach, properties of chemical reactions are manipulated on a macroscopic scale by the design of the reactor. The intrinsic reaction rates of the employed catalyst are predicted using microkinetic models, which are mostly based on crude measurements taken over a limited range of operating conditions. This approach falls short for systems that must operate under severe experimental conditions for which measurements are limited, time-consuming and expensive. Therefore, chemical industries have a pressing need for a more reliable prediction of production rates for converting reactants into desired products.

To improve the predictions, it is highly desired to utilize a better kinetic model that covers a wide range of operating conditions. The obstacle lies with the understanding and control of the chemical reaction that occurs on the surface of the catalyst, as well as the reactor design. This is why multiscale modeling paves the way for a breakthrough, especially for heterogeneous catalytic systems.

Our work in this chapter addresses microkinetic modeling for the Deacon process, i.e. catalytic oxidation of HCl to produce high purity Cl$_2$. The reaction mechanism of the Deacon process is complex, and experiments are critical to get a feel for the reaction. The situation is aggravated by the harsh operating conditions – due to the corrosive nature of reactants and products,[15] which severely limits the availability of experimental data. Although RuO$_2$-based catalysts have shown exceptional activity and stability under these reactive conditions,[26] ruthenium as a precious metal, is very expensive and shows limited availability. Considering the scale of chlorine production,[3,4] the design and utilization of more convenient and economical Deacon

catalysts with the same or better level of activity and stability would have a significant impact on chlorine industrial production. For example, incorporation of non-precious additives or dopants into RuO_2 catalysts is supposed to be a very promising route.

In order to achieve this ambitious goal, the first task is to identify the regions over which a catalyst is expected to have higher activity. The oxidation reaction of HCl on a RuO_2 catalyst needs to be better understood. To this end, we compare macro- and microkinetic models and validate them to the extent that experiments are available. Our approach emphasizes the inclusion of microscopic insight into the reaction mechanism as well as the link between surface science and the widely-used empirical-based modeling of reaction kinetics. The outcome is a foundation to guide experimental measurements - always the gold standard for results - which will accelerate research progress by narrowing down the scope of time-consuming and expensive experiments. In short, we hope that the theoretical modeling can efficiently and economically guide the catalyst design.

3.2 Methodology

Here, we present a mechanistic microkinetic study for the Deacon reaction based on a Langmuir-Hinshelwood-Hougen-Watson (LHHW) microkinetic approach. In the LHHW-based microkinetics, the reaction can be disassembled into several elementary steps, within the main underlying assumption that (at least) one of the elementary steps in the mechanism is intrinsically slow. Thus, this step would act as the rate-determining step (r.d.s.). The other processes are assumed to be fast and in partial equilibrium. As the overall reaction rate is expressed based on the rate of the chosen rate-determining step, the rate expression would then depend on the choice of this elementary step. In order to resolve the consequent multiplicity[61] arising in the rate expressions, microscopic insights into the reaction mechanism, and dedicated experimental verifications are also required.[62]

Previous studies on the catalytic oxidation of HCl over RuO_2(110) surface suggested that the reaction can be structured into five steps.[4,15,38] It starts with the dissociative adsorption of HCl, which occurs by H removal through an adsorbed O atom on the surface, forming an on-top Cl species and an OH group (Step 1). The reaction is

proceeded by the recombination of two hydroxyl groups resulting in the formation of surface water species (Step 2), the recombination of two on-top Cl and the consequent desorption of Cl_2 (Step 3), and the desorption of water from the surface (Step 4). The final step is the dissociative oxygen adsorption for surface regeneration (Step 5). The individual elementary steps involved in the Deacon process, with a vacant active site denoted by *, are summarized in the below Table 3.1. Although the above elementary steps appear quite simple, the complexity of the real process is large due to the distinct nature of the oxygen species on the surface and the different oxygen and chlorine coverage.[15]

Table 3.1 Elementary steps of the Deacon process.

Step	Surface Reaction
1	$HCl + O* + * \rightleftharpoons Cl* + OH*$
2	$OH* + OH* \rightleftharpoons H_2O* + O*$
3	$Cl* + Cl* \rightleftharpoons Cl_2 + 2*$
4	$H_2O* \rightleftharpoons H_2O + *$
5	$O_2 + 2* \rightleftharpoons 2O*$

Several research works on the mechanism of the Deacon process were found to fit a Langmuir-Hinshelwood kinetic model with the recombination of the top-chlorine atoms as the rate-determining step,[15,36,63] while another study by Pérez-Ramírez et al. suggested a Mars-van Krevelen type of kinetics where the surface undergoes re-oxidation.[4] An enhanced Cl_2 production was revealed by increasing the feed ratio of O_2/HCl. Over et al. recently found that the dissociative adsorption of HCl required basic sites such as surface oxygen atoms.[29] Since the surface oxygen desorption on $RuO_2(110)$ occurs at temperatures below the actual reaction temperature, the concentration of oxygen atoms on the surface would not be sufficient to dissociate HCl under the reaction conditions. Therefore, it suggested that the rate-determining step in the Deacon process would instead be the oxygen chemisorption (Step 5), although the recombination of chlorine (Step 3) was shown to have the highest energy barrier. In a Langmuir-Hinshelwood-based kinetic model proposed by Studt et al., both O_2

dissociation and Cl-Cl recombination processes were proposed to equally control the reaction rate.[38]

In this study, we established and compared three LHHW-like microkinetic models, in which the assumption of the rate-determining step (r.d.s.) varies for each model. The choices of the elementary step(s) considered in these models as the r.d.s. include: (i) the O_2 dissociation, (ii) the Cl-Cl recombination, and (iii) both the O_2 dissociation and the Cl-Cl recombination processes. These three assumptions are abbreviated to "O_2-diss. Model", "Cl_2-recom. Model", and "O_2-diss. & Cl_2-recom. Model", respectively. The parameters associated with each kinetic model are estimated within two approaches. First, fitting the corresponding reaction model to the available experimental data, in which the surface coverage of each of the reaction species is represented by an ordinary differential equation (ODE). The model parameters (rate constants) are estimated by solving the corresponding set of ODEs simultaneously through minimizing an objective function defined as the weighted sum of squares of the difference between the experimental pressures of the reaction species and those estimated by the kinetic model. The minimization is performed by using the Nelder-Mead simplex (direct search) method. The kinetic models are validated to the extent to which experiments are available.

3.2.1 Langmuir-Hinshelwood-Hougen-Watson (LHHW) kinetic models

Eley-Rideal or Langmuir-Hinshelwood kinetics are generally utilized to describe heterogeneously catalytic reactions. The former kinetic model depicts the reaction of a chemisorbed molecule directly with a gas phase molecule, while the latter implies that all species are adsorbed on the surface before the reaction.[64] In this work, the approach of the mechanistic microkinetic study for the Deacon process is derived from the latter kinetic model.

For an equilibrium elementary step in the surface reactions, the adsorbed molecules A and B on the surface react with each other to generate products C and D (e.g. step 1 and 2 in Table 3.1).

$$v_A A^* + v_B B^* \underset{k_-}{\overset{k_+}{\rightleftharpoons}} v_P P^* + v_Q Q^* \qquad (3.1)$$
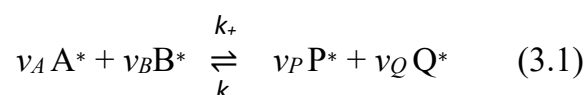
Here, A and B are reactant chemical species, P and Q are product species, and v_A, v_B, v_P, and v_Q are the stoichiometric coefficients of the respective reactants and products. k_+ and k_- stand for the forward and reverse rate constants, respectively.

For the above reaction (3.1), the forward reaction rate can be written as

$$r_{forward} = k_+ \left[A^*\right]^{v_A} \left[B^*\right]^{v_B} \qquad (3.2)$$

In addition, the backward reaction rate can be written as

$$r_{backward} = k_- \left[P^*\right]^{v_P} \left[Q^*\right]^{v_Q} \qquad (3.3)$$

Where $[X^*]$ represents the concentration of the surface species X^*, and v_i is the stoichiometric factor.

Since at equilibrium forward and backward rates are equal, we have

$$k_+ \left[A^*\right]^{v_A} \left[B^*\right]^{v_B} = k_- \left[P^*\right]^{v_P} \left[Q^*\right]^{v_Q} \qquad (3.4)$$

The ratio of the rate constants is thus also a constant and is known as equilibrium constant

$$K = \frac{k_+}{k_-} = \frac{\left[P^*\right]^{v_P} \left[Q^*\right]^{v_Q}}{\left[A^*\right]^{v_A} \left[B^*\right]^{v_B}} \qquad (3.5)$$

In the LHHW model, the total reaction rate can be expressed as the reaction rate of the rate-determining step. If the rate-determining step is expressed as

$$aA + bB \rightarrow cC + dD \qquad (3.6)$$
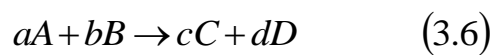
where the lowercase letters (a, b, c, and d) represent stoichiometric coefficients, while the capital letters represent the reactants (A and B) and the products (C and D).

The rate equation is an equation that links the reaction rate with the concentrations or pressures of the reactants and constant parameters (normally rate coefficients and partial reaction orders). Thus, the reaction rate is generally given by a power law such as

$$r = k(T)[A]^a[B]^b \qquad (3.7)$$

For gas phase reactions, the rate is often alternatively expressed by partial pressures. In equation 3.7, $k(T)$ is the reaction rate coefficient or rate constant, which includes all the parameters that influence the reaction rate except for concentration. Among the parameters affecting the reaction rate, temperature is normally taken into account as the most important factor and expressed by an Arrhenius equation

$$k = A \cdot \exp\left(-\frac{E_a}{RT}\right) \qquad (3.8)$$

Here, A is the Arrhenius coefficient. The activation energy, E_a, can be evaluated from the variation in reaction rate coefficients as a function of temperature (within the validity of the Arrhenius equation). It may further depend on sorption processes and hence coverages.[64]

As already discussed in this chapter, the key point in the utilization of an LHHW kinetics model is to determine the slowest elementary step, i.e. the rate determining step (r.d.s.) in the mechanism of the Deacon process. The overall reaction rate is then mainly expressed according to the rate-determining step. The remaining steps are relatively fast and hence equilibrated, so that they will no longer be taken into account. Three assumptions of the LHHW kinetic model can be obtained based on the previous analysis: (i) O_2 dissociation as r.d.s; (ii) Cl-Cl recombination as r.d.s; and (iii) both of the above two steps are simultaneously assumed to be r.d.s. Each r.d.s. assumption can be represented by a corresponding rate expression.

$$r = k p_{O_2} \left(K_O p_{HCl}^{-2} p_{Cl_2} p_{H_2O} + K_{OH} p_{HCl}^{-1} p_{Cl_2}^{0.5} p_{H_2O} + K_{Cl} p_{Cl_2}^{0.5} + K_{H_2O} p_{H_2O} + 1 \right)^{-2} \qquad (3.9)$$

If the O_2 dissociation step is assumed to be the rate-determining step, we can obtain the first LHHW kinetic model (O_2-diss. model), the overall reaction rate of which can be expressed as (see Appendix A for the details):

where k represents the forward rate constant, K_i represents the equilibrium constant of step i (i = 1, 2, 3, 4). In the above formula 3.9, $K_{Cl} p_{Cl_2}^{0.5}$ and $K_{H_2O} p_{H_2O}$ can be thought as the product inhibition terms, and the other two terms of K_O and K_{OH} are considered to be the reactant promoting factors (see formula 3.10).

$$K_O = K_1^{-2} K_2^{-1} K_3^{-1} K_4^{-1}, \qquad K_{OH} = K_1^{-1} K_2^{-1} K_3^{-0.5} K_4^{-1},$$

$$K_{Cl} = K_3^{-0.5}, \qquad\qquad K_{H_2O} = K_4^{-1} \qquad (3.10)$$

If the Cl_2 recombination process is proposed to be the rate-determining step, we can also obtain the second LHHW kinetic model (Cl_2-recom. model), which can be expressed as:

$$r = \frac{K' * P_{HCl}^2 * P_{O_2}^{0.5}}{P_{H_2O} * \left(1 + K_O * P_{O_2}^{0.5} + K_{OH} * P_{H_2O}^{0.5} * P_{O_2}^{0.25} + K_{Cl} * P_{HCl} * P_{O_2}^{0.25} * P_{H_2O}^{-0.5} + K_{H_2O} * P_{H_2O}\right)^2} \qquad (3.11)$$

In the above formula,

$$K' = k * K_1^2 * K_2 * K_4 * \sqrt{K_5}, \qquad K_O = \sqrt{K_5}, \qquad K_{OH} = \sqrt{\frac{\sqrt{K_5}}{K_2 * K_4}},$$

$$K_{H_2O} = \frac{1}{K_4}, \qquad K_{Cl} = K_1 * \sqrt{K_2 * K_4 * \sqrt{K_5}} \qquad (3.12)$$

Inspired by the work of Studt et al.,[38] we also developed a third LHHW kinetic model (O_2-diss. & Cl_2-recom. model), in which both the O_2 dissociation and Cl_2 recombination are assumed as the rate-determining steps. This third LHHW kinetic model can be written as follows:

$$r = k_5 p_{O_2} (K_O p_{HCl}^{-2} p_{O_2} p_{H_2O} + K_{OH} p_{HCl}^{-1} p_{O_2}^{0.5} p_{H_2O} + K_{Cl} p_{O_2}^{0.5} + K_{H_2O} p_{H_2O} + 1)^{-2} \qquad (3.13)$$

The above coefficients K_O, K_{OH}, K_{Cl}, and K_{H2O} in formula 3.13 indicate

$$K_O = K_1^{-2} K_2^{-1} k_3^{-1} K_4^{-1} k_5 \qquad K_{OH} = K_1^{-1} K_2^{-1} k_3^{-0.5} K_4^{-1} k_5^{0.5}$$

$$K_{Cl} = k_3^{-0.5} k_5^{0.5} \qquad\qquad K_{H_2O} = K_4^{-1} \qquad (3.14)$$

In the most common way of reaction kinetic study, especially in industrial applications, model parameters (i.e. rate constants) are estimated by fitting the derived rate expression to a set of experiments. However, due to the severe operational conditions, the available experimental data are rather limited and available only over a narrow range of operational conditions. This limits the predictability of the proposed model

over a wider range. Meanwhile the rate-determining step may also change. To circumvent this limitation, the model parameters in our present studies are completely obtained from first-principles calculations, as summarized in Table 3.2. A comparison of these calculated values with the data obtained by fitting the rate expression to the available experimental results has been carried out (see the results in the discussion part). The model prediction and the fit to the experimental results in the above three cases are illustrated in Figures 3.2-3.4.

3.2.2 Theory-based reaction model

In this approach, the reaction mechanism was scrutinized microscopically on the $RuO_2(110)$ surface. Extensive theoretical and experimental studies on $RuO_2(110)$ [29,65,66] have revealed that two prominent active sites play a different role in the reactivity of this surface. The left of Figure 3.1 exhibits the full view of a (1x2) surface unit-cell slab of $RuO_2(110)$ as used for the DFT calculations, while the right shows the $RuO_2(110)$ surface from the top, illustrating these two sites denoted as "br" and "cus".

DFT calculations corroborated by experimental techniques[35,63] such as low-energy electron diffraction (LEED) and high-resolution core level shift (HRCLS) attributed the remarkable stability of RuO_2 to the chlorination of the RuO_2 surface through self-limiting replacement of the surface oxygen atom by chlorine. It was shown that the active surface included the chlorine atoms at the bridge positions on the $RuO_2(110)$ surface,[34,35,37] which stabilizes the oxide surface against reduction under the reactive conditions. The coverage of the corresponding "br" sites was claimed to result in a one-dimensional reactivity along the cus rows. In the reaction mechanism considered in the present work as summarized in Table 3.2, we would thus explicitly refer to the "cus" site as the catalytic active site, with the corresponding binding and barrier energies calculated based on the cus sites.
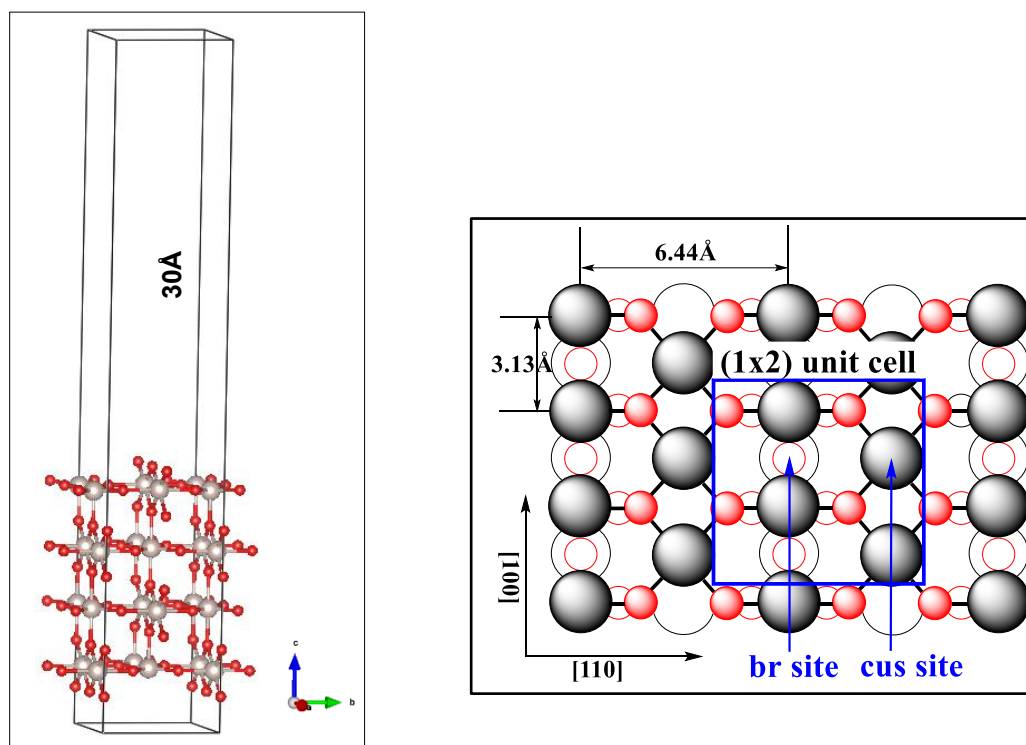
Figure 3.1 Left: full view of the (1x2) surface unit-cell slab of RuO_2(110) as used for the DFT calculations, also showing the vacuum separation between the periodic slab images. Right: top view of the RuO_2(110) surface illustrating the location of the prominent br(idge) and coordinatively unsaturated (cus) adsorption sites offered by the O-poor termination. The blue solid rectangle shows the size of the employed (1x2) surface unit-cell. Large gray spheres represent Ru atoms, small red spheres represent O atoms.

Table 3.2 Elementary steps considered in the Deacon reaction with the DFT calculated activation barriers, E_{forw}/E_{backw}, for the forward and backward reactions, respectively.

Process	$\Delta E_{forw}/\Delta E_{backw}$ (eV)	
	This work	Literature
Reactant adsorption/desorption		
$HCl + O* + * \rightleftharpoons Cl* + OH*$	0.0/1.1	0.0/1.0[a]
$O_2 + 2* \rightleftharpoons 2O*$	0.0/2.0	0.0/2.0[b]
Product formation/desorption/re-adsorption		
$OH* + OH* \rightleftharpoons H_2O* + O*$	0.3/0.3	0.2/-[a]
$Cl* + Cl* \rightleftharpoons Cl_2 + 2*$	2.0/0.0	1.6/-[a]
$H_2O* \rightleftharpoons H_2O + *$	1.1/0.0	0.9/-[a]

[a] Reference 4.   [b] Reference 67.

3.2.3 First-principles rate constants

First-principles rate constants are calculated following the approach by Reuter and Scheffler[65] relying on kinetic gas theory for the adsorption and desorption processes, and harmonic transition state theory (HTST) for diffusion processes. The non-activated adsorption rate is expressed as the rate by which the particles impinge on the unit-cell area, A_{uc}. The sticking coeffcient, $\tilde{S}_{st,i}(T)$, gives the fraction of the impinging particles of species i that stick to a vacant site at a certain temperature, taking into account the non-equivalent sites within the unit cell,

$$r_{st,i}^{ads}(T, p_i) = \tilde{S}_{st,i}(T)\frac{p_i A_{uc}}{\sqrt{2\pi m_i k_B T}} \qquad (3.15)$$

where p_i is the partial pressure of the species i, k_B is the Boltzmann constant, and m_i is the particle mass. Here, the pre-factors $\tilde{S}_{st,i}(T)$ for O_2 and HCl are roughly approximated to one.[65]

The desorption rate is calculated assuming equilibrium between the adsorption and desorption processes,

$$\frac{r_{st,i}^{ads}(T, p_i)}{r_{st,i}^{des}(T)} = \exp\left(\frac{\Delta G_{st,i}(T, p_i)}{k_B T}\right) \approx \exp\left(\frac{\mu_{gas,i}(T, p_i) - E_{st,i}^b}{k_B T}\right) \qquad (3.16)$$

where $\Delta G_{st,i}(T, p_i)$ denotes the change in the Gibbs free energy of the species i between the gas phase and the adsorbed states. It is approximated by the difference between the chemical potential of the species i in its pure (single-phase) form in the gas phase, $\mu_{gas,i}(T, p_i)$, and its corresponding binding energy on the surface, $E_{st,i}^b(T)$.

The diffusion (hopping) rate of the species i from one site ($_{st}$) to the adjacent site ($_{st'}$) is approximated by,

$$r_{st,st',i}^{diff}(T) \approx \left(\frac{k_B T}{h}\right)\exp\left(-\frac{\Delta E_{st,st',i}^{diff}}{k_B T}\right) \qquad (3.17)$$

where $E_{st,st',i}^{diff}$ is the diffusion barrier of the species i from one site ($_{st}$) to the adjacent site ($_{st'}$).

Employing this approach, the ingredients required to establish a first-principles-based kinetic model are the binding energies (E_b) of the reactive species on the $RuO_2(110)$ surface, as well as the barrier energies (ΔE) of the individual elementary steps. The latter were calculated using the linear and quadratic synchronous transit (LST/QST) methods.[60]

The calculations were carried out using DFT as implemented in the plane-wave code CASTEP.[68] The revised generalized gradient approximation (GGA) functional of Perdew, Becke, and Ernzerhof (RPBE)[49] was used for treating electronic exchange and correlation. Ultrasoft pseudopotentials[69] were employed for the description of the electron-nuclear interaction. The surfaces were modeled as slabs consisting of (1×2) unit cells within periodic boundary conditions, consisting of 4 layers and separated by 30 Å of vacuum as is shown in Figure 3.1 (left view). The atomic positions of the two topmost layers were allowed to fully relax. The calculations were performed using an energy cut-off of 450 eV, a Brillouin zone (BZ) integration over a (6×6×1) Monkhorst-Pack grid with 18 k-points. Convergence criteria for total energy, force, and displacement were 2×10^{-5} eV/atom, 5×10^{-2} eV/Å and 1×10^{-3} Å, respectively.

The calculated DFT binding energies of the stable surface species at 1/2 monolayer (ML) coverage on a (1×2) stoichiometric $RuO_2(110)$ surface are summarized in Table 3.3. These values are in close agreement with the reported values in the literature with one exception with respect to the binding energy of the surface H_2O species. We report a much lower binding energy for the adsorption of H_2O on the cus site compared to the one reported by Hess et al.[37]. Experimental studies[63,70] suggest a desorption temperature of 400 K and above for the desorption of water from $RuO_2(110)$. The large binding energy of H_2O reported by Hess et al.[37] is completely inconsistent with these experiments.

Table 3.3 DFT binding energies (E_b) of different surface species involved in the Deacon reaction. Shown are the values for the adsorption and the desorption on/from the cus sites at a 1/2 monolayer (ML) coverage of a (1x2) stoichiometric RuO_2(110) surface, as depicted in Figure 3.1. Hydrogen adsorbs on top of an oxygen atom, denoted as H@O* (1 eV = 96 kJ/mol).

Surface species	E_b(eV)	
	This work	Literature
O*	-1.1	-1.1[a],-0.8[b]
H@O*	-1.3	-
Cl*	-1.4	-1.6[c]
H2O*	-1.1	-4.2[d]

[a] Reference 65.   [b] Reference 71.   [c] Reference 35.   [d] Reference 37.

3.3 Results and discussion

3.3.1 Fitting vs. theory-based prediction

As mentioned above, we obtained three different LHHW kinetic models for the Deacon reaction over the RuO_2(110) surface, each formula of which involves five corresponding parameters except for the partial pressure of reactants and products. Thus, the determination of these five parameters becomes critical to the accuracy of these kinetic models, which in turn is the prerequisite to properly analyze and understand the microscopic mechanism for the Deacon reaction over the RuO_2(110) surface within this approach.

In general, the model parameters can be obtained by either applying kinetic models to fit the limited experimental data, or using a theory-based method for direct calculation. Table 3.4 summarizes the estimated model parameters by fitting the three LHHW models to the experimental data reported by Teschner et. al[36] over a RuO_2/SnO_2-Al_2O_3 catalyst at T = 573 K, 1 bar and a 1:1 feed molar ratio of O_2/HCl. Here, in Table 3.4 we only list three sets (1 to 3) of data for each model to reflect the feasibility and diversity of the method. The three obtained sets of parameters are based on fitting the model with different initial guesses for the rate constants. All sets result in very good fits to the available experimental data. However, the spread in the obtained parameters immediately shows that these are merely effective parameters without any microscopic meaning. Therefore, as an alternative, we used equations 3.11 to 3.13 to directly calculate the rate constants involved in the corresponding LHHW models from first-principles. Table 3.4 compares the fitted parameters to these directly calculated ones. In the following text, we plotted each LHHW model with the parameters obtained through the above two different methods for detailed comparison.

Table 3.4 Model parameters corresponding to the individual elementary steps in the Deacon reaction mechanism shown in Table 3.1 assuming three different r.d.s.(s). Multiple sets (1 to 3) of the reported parameters are estimated by fitting each model to the available experiments[36] carried out on a $RuO_2/SnO_2-Al_2O_3$ catalyst at T = 573 K, P = 1 bar and a 1:1 feed molar ratio of O_2/HCl. The estimated parameters for each model are compared to those obtained theoretically using DFT calculations.

	Model Parameters			
	Set 1	Set 2	Set 3	DFT
O_2-diss. Model		r.d.s.: $O_2 + 2* \leftrightarrow 2O*$		
K_1	1.00e1±0.13	5.40e-1±0.00	3.00e-2±0.00[a]	2.10e-2
K_2	1.53e1±0.08	5.39e1±1.33	7.18e2±0.08	5.74e1
K_3	1.01e-7±0.00[a]	4.36e-8±0.00[a]	5.55e-8±0.00[a]	3.34e-3
K_4	1.00e2±0.04	1.00e2±0.01	3.12e2±0.02	2.32e2
$K_{5,rds}$	1.24e3±10.02	3.06e3±5.18	3.00e3±4.27	3.87e3
Cl_2-recom. Model		r.d.s.: $2Cl* \leftrightarrow Cl_2 + 2*$		
K_1	3.57e1±0.09	1.95e-1±0.00[a]	2.35e-2±0.00[a]	2.10e-2
K_2	6.40e-3±0.00[a]	6.68e-1±0.00[a]	5.25e0±0.00[a]	5.74e1
$k_{3,rds}$	8.47e0±0.00[a]	8.67e-1±0.00[a]	1.02e0±0.00[a]	3.10e-3
K_4	9.56e0±0.00[a]	6.12e0±0.00[a]	1.97e0±0.00[a]	2.32e2
K_5	5.00e-4±0.00[a]	1.86e-1±0.00[a]	2.15e0±0.00[a]	3.29e3
O_2-diss.&Cl_2-recom. Model		r.d.s.: $O_2 + 2* \leftrightarrow 2O*$ and $2Cl* \leftrightarrow Cl_2 + 2*$		
K_1	1.00e1±0.13	5.40e-1±0.00	3.00e-2±0.01	2.00e-2
K_2	1.53e1±0.08	5.39e1±1.33	7.18e2±0.08	5.74e2
$k_{3,rds}$	1.01e-7±0.00[a]	4.36e-8±0.00[a]	5.55e-8±0.00[a]	3.34e-3
K_4	1.00e2±0.04	1.00e2±0.01	3.12e2±0.02	2.32e2
$k_{5,rds}$	1.24e3±10.02	3.06e3±5.18	3.00e3±4.27	3.87e3

[a] *The associated standard error ≤ e-10.*

Figure 3.2 depicts an exemplary illustration of the experimentally measured reactant and product distributions over time where the LHHW model with the Cl_2 recombination step as r.d.s. is fitted to these experimental data. The results shown in Figure 3.2 compare the model fit to the experiments when set 1 of the estimated rate constants listed in Table 3.4 is used, with the case where the rate constants are directly calculated using DFT. In this figure, parameters, whether estimated by data fitting or theoretically obtained by DFT calculations, are substituted into the O_2-diss. model and both fit very well with the experiments.[36]
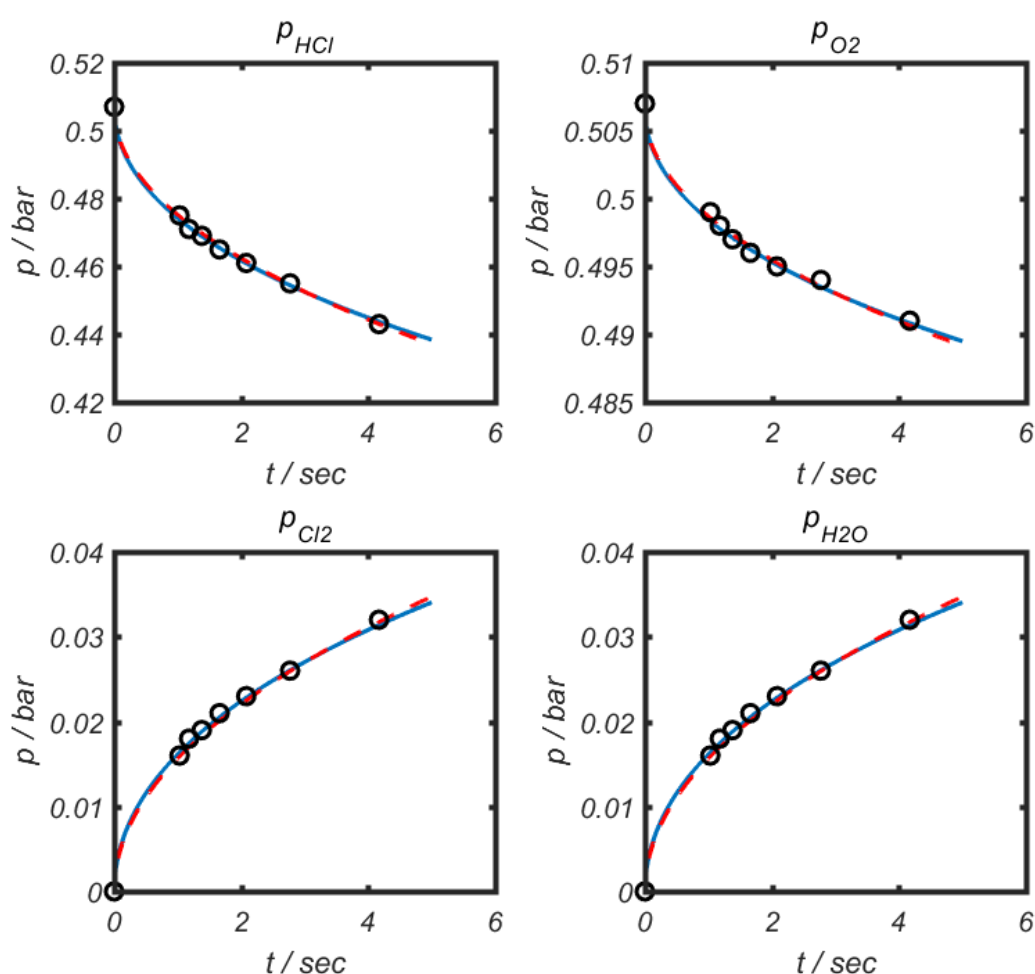

Figure 3.2 The LHHW Cl_2-recom. model as described in section 3.2.1 reproducing the Deacon reaction measurements[36] (open circles) on a RuO_2/SnO_2-Al_2O_3 catalyst at T = 573 K and 1 bar: (red dashed line) model parameters are estimated by fitting to the experimental data (set 1) in Table 3.4; (blue solid line) the parameters are directly calculated using DFT.

As seen in Figure 3.2, both approaches in estimating the rate constants in the LHHW kinetic model (with the assumption of the Cl_2 recombination step as the reaction rate-determining step) are perfectly consistent with the observed experiments. The results of the other two models, in which the O_2 dissociation step or both the O_2 dissociation and Cl_2 recombination processes are assumed as r.d.s., can similarly reproduce the measurements, shown in Figure 3.3 and 3.4, respectively. The estimated sets of parameters reported in Table 3.4 for each model can, thereby, change even by several orders of magnitude since they are based on different sets of initial conditions (see the details of the models in the Appendix).
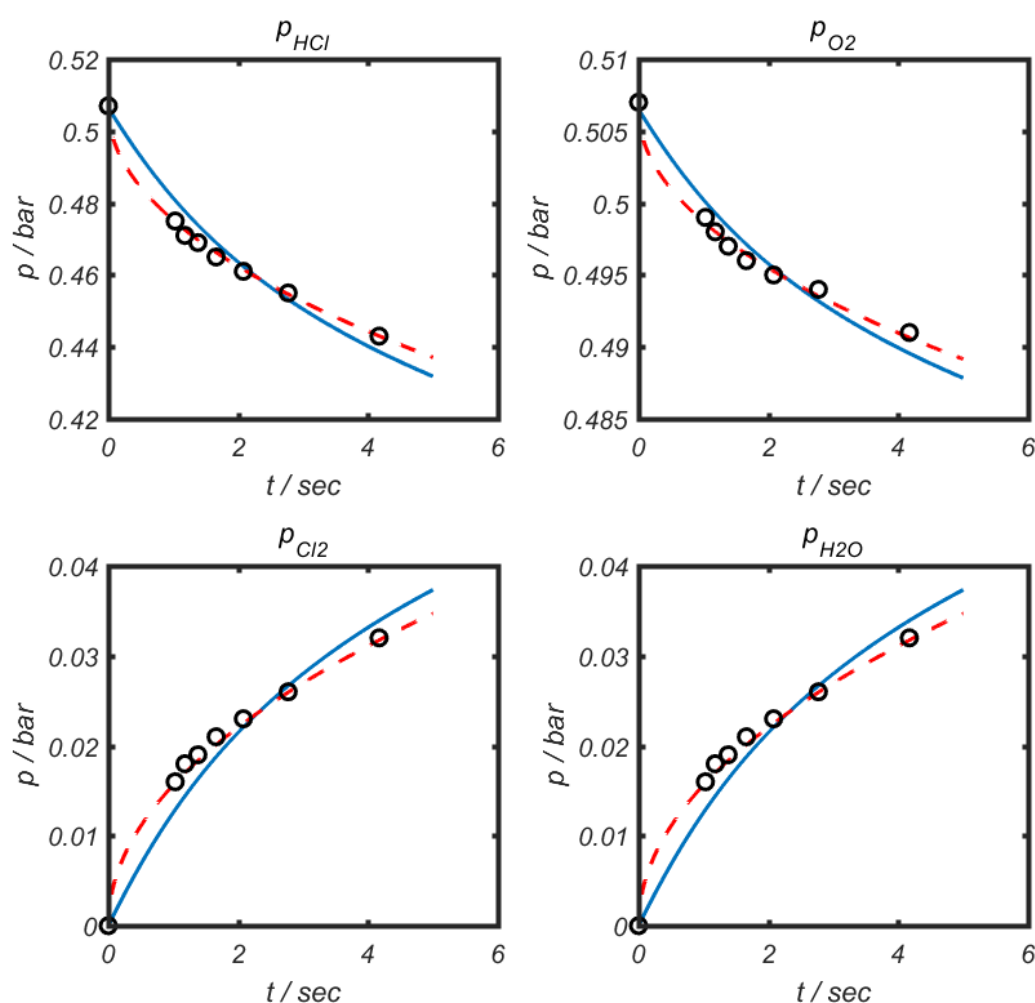
**Figure 3.3** The LHHW O_2-diss. model as described in section 3.2.1 reproducing the Deacon reaction measurements[36] (open circles) on a RuO_2/SnO_2-Al_2O_3 catalyst at T = 573 K and 1 bar: (red dashed line) model parameters are estimated by fitting to the experimental data (set 1) in Table 3.4; (blue solid line) the parameters are directly calculated using DFT.

Using DFT-based rate constants for the two latter models, however, does not provide a reasonable prediction of the experiments compared to the second model in which the Cl_2 recombination is the r.d.s. in the mechanism. Figure 3.3 illustrates the obtained prediction of the LHHW model with Cl_2 recombination as r.d.s., while Figure 3.4 depicts the comparison of our results using both the O_2 dissociation and Cl_2 recombination processes as r.d.s.. Compared with the model estimated by data fitting, the latter two DFT-based models are slightly different from experimental data.
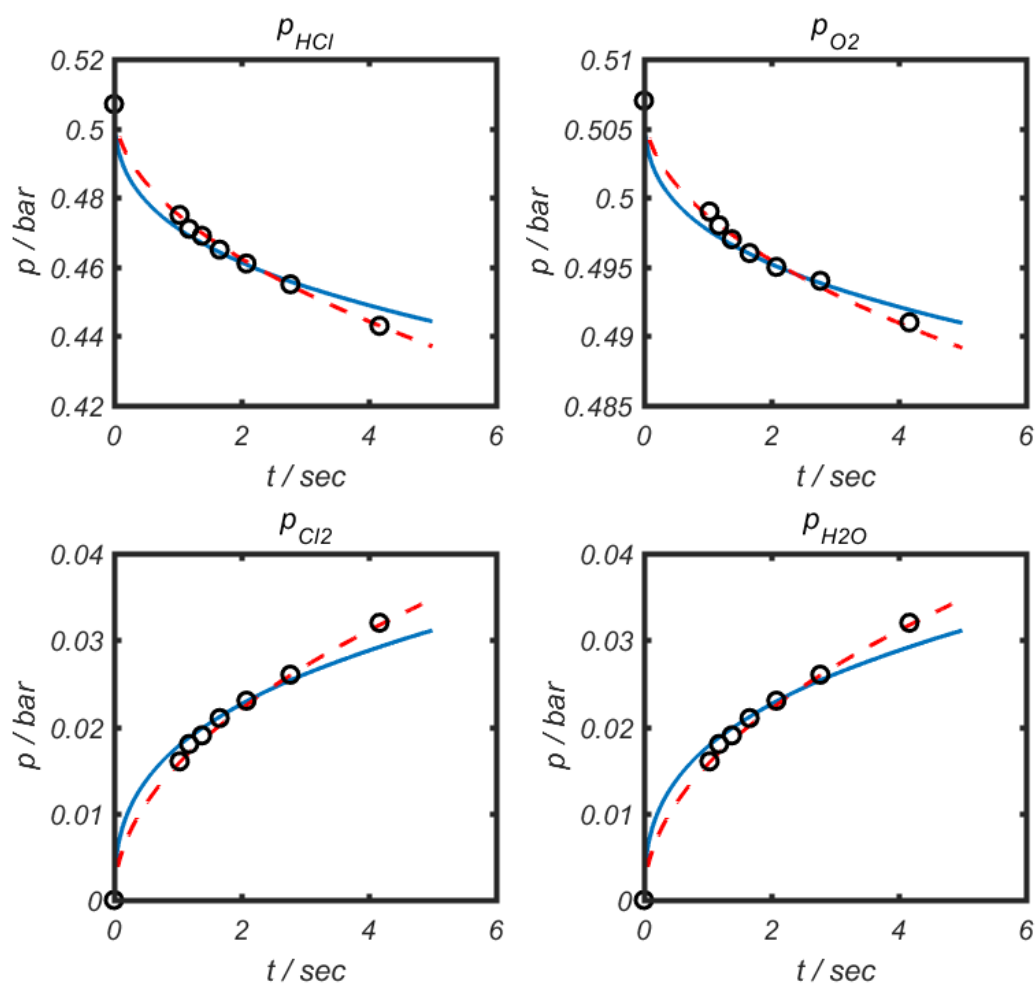

Figure 3.4 The LHHW O_2-diss. & Cl_2-recom. model as described in section 3.2.1 reproducing the Deacon reaction measurements[36] (open circles) on a $RuO_2/SnO_2-Al_2O_3$ catalyst at T = 573 K and 1 bar: (red dashed line) model parameters are estimated by fitting to the experimental data (set 1) in Table 3.4 ; (blue solid line) the parameters are directly calculated using DFT.

As can be seen in Figure 3.3, DFT-based parameters incorporated into the O_2-diss. model does not reproduce the experimental results. The same observation holds for the third LHHW model examined, with both the O_2 dissociation and Cl_2 recombination processes as r.d.s., shown in Figure 3.4. In these two cases, DFT-based parameters as the model input result in a significant deviation with the results from experiments. Therefore, among the three above-mentioned LHHW micro-kinetic models with the model parameters estimated from data fitting or DFT theoretical calculations, the second LHHW kinetic model, i.e. Cl_2 recombination as the rate-determining step, seems to provide the most robust agreement with the limited experimental data.

In our studies, we also determined the variation in the occupation of the active sites (*, O, OH, Cl, and H_2O) at the RuO_2/SnO_2-Al_2O_3 catalyst surface during the experiments. Figure 3.5 depicts an exemplary illustration for their changes over reaction time, where the second LHHW kinetic model (Cl_2 recombination step as r.d.s.) is applied and the relevant parameters are calculated by DFT. Figure 3.5 indicates that the surface coverage of chlorine atoms (ϑ_{Cl*}) nearly occupies all the catalyst surface sites, whereas the surface coverage of the other four species are quite small (less than 2%), especially to ϑ_{O*} and ϑ_{OH*}. As the reaction proceeds, the coverage of chlorine atoms (ϑ_{Cl*}) has a small decrease, which is similar to the surface coverage of active vacancies (ϑ_*), ultimately staying at zero. These results also indicate that the surface sites are almost entirely occupied during the whole reaction process and almost no vacancy remains. Meanwhile, the surface coverage of another three species is relatively increased. The extremely low surface coverage of O* and OH* species can be explained by the fact that these two surface species proceed immediately to the next reaction process when they are adsorbed on the surface, reflecting that the reaction rate of the corresponding step is relatively fast. This is also consistent with the reaction rate constants obtained from DFT calculations in Table 3.4, which yield the smallest rate constant for the second process (i.e. the chlorine recombination step)

We further calculated the rate constants of the steps associated with surface oxygen atoms by DFT. The rate constants of the first step (dissociative adsorption of HCl near an oxygen atom, and the basic center abstraction of the H atom to form OH), the second step (two OH groups form a water molecule) and the fifth step (the dissociative adsorption of O_2) are 2.10e-2, 5.74e1 and 3.29e3, respectively. The rate constants of these three steps, especially the latter two steps, are relatively large in comparison to

the other elementary steps (cf. the reaction rate constant of Cl_2 recombination is 3.10e-3). The same situation occurs in the other two cases. Due to the high surface coverage of chlorine atoms and very few surface vacancies, it can be finally determined that the Cl_2 recombination step is rate-limiting, which is in agreement with the conclusion from the experimental results.[36]
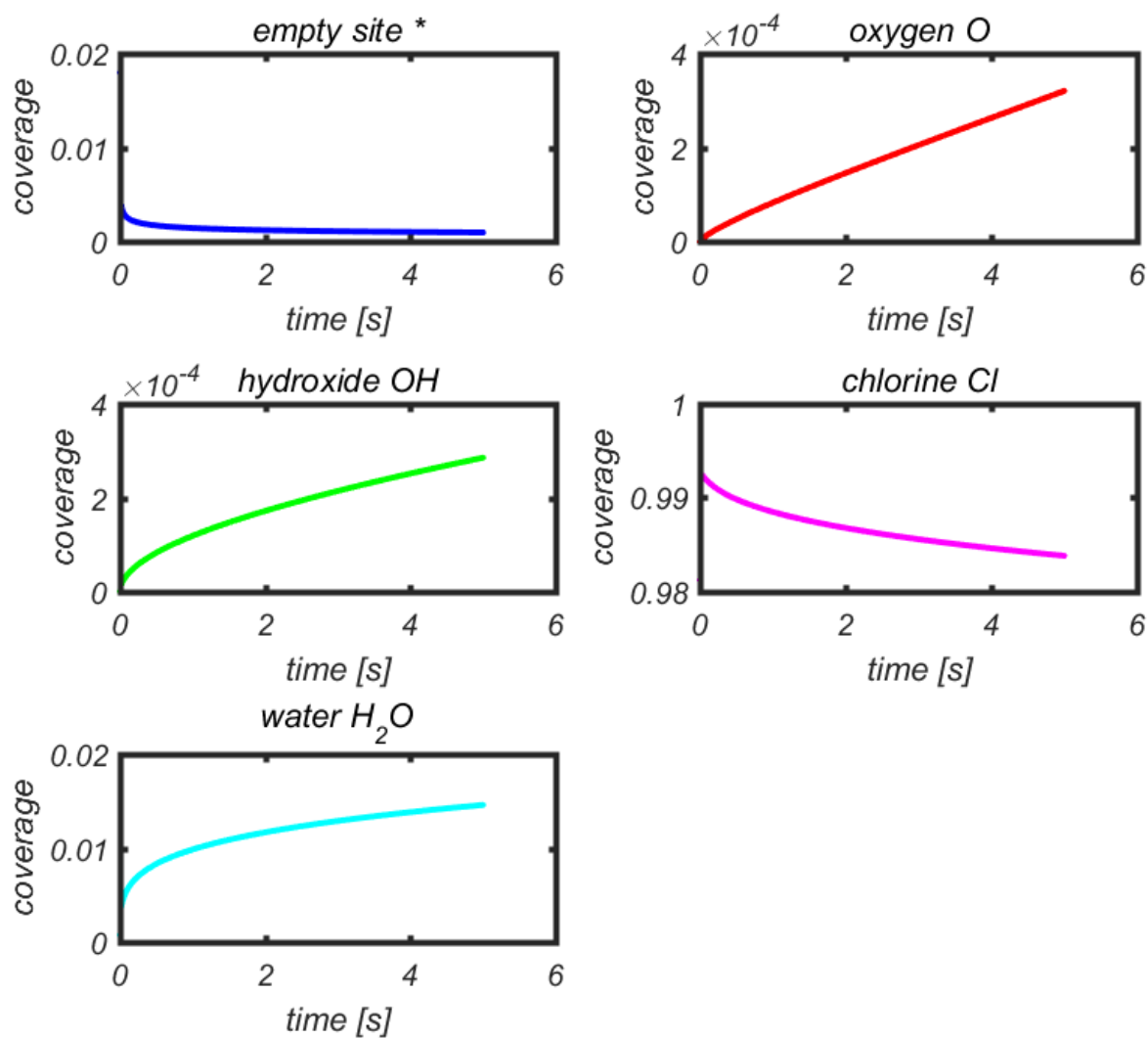

Figure 3.5 Coverage changes of the individual surface species (*, O, OH, Cl, and H_2O) varying with time for the LHHW Cl_2-recom. model, in which the parameters are directly calculated using DFT. It reproduces the Deacon reaction measurements[36] on a RuO_2/SnO_2-Al_2O_3 catalyst at T = 573 K and 1 bar.

3.3.2 Wide-range prediction

Our analysis of the fitting & theory prediction indicated, no matter whether the rate constants were estimated by data fitting or obtained theoretically from first-principles calculations, the second LHHW microkinetic model (Cl_2 recombination step as r.d.s.) reaches the best match to the experiments. However, our understanding of the microscopic mechanism of the Deacon process is still rather limited due to the scant experimental data available. Considering the applicability of the model, which would be more interesting for industry, we want to carry out more research on scaling it up and conducting the reaction in a wider range of operational conditions.

In order to afford a deeper and more precise analysis of the microscopic reaction mechanism for the Deacon Process over RuO_2(110) surface, we generate 2D-plots of rate and surface coverages over a wide range of reactants partial pressures from 10^{-2} to 10^2 bar at different reaction temperatures (e.g. 573 K, 673 K, etc.). Two types of information are included in the 2D-plots: the activity map and surface coverage. The surface distribution of each individual reaction species is described by a time-dependent ordinary differential equation (ODE), which is summarized in Appendix-C. The ODEs are implicitly solved within a small integration tolerance of 10^{-6}, which was chosen due to the significant stiffness of the model. It results from the wide variation in the range of barrier energies associated with the elementary steps involved in the reaction. Full convergence of the mean-field simulations is ensured by systematic evaluation of the errors associated with each simulation step.
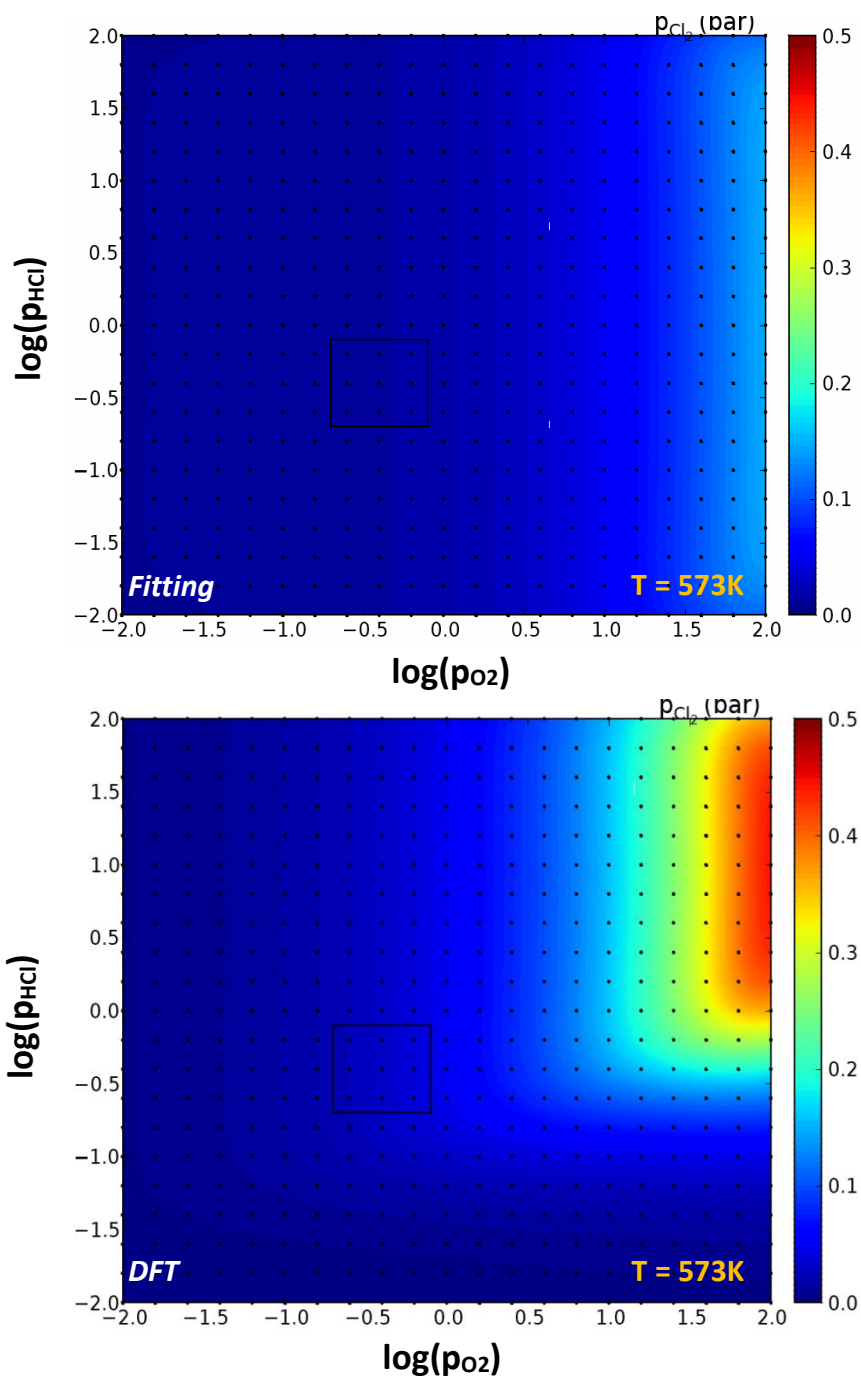
Figure 3.6 Results of the LHHW Cl_2 recombination model prediction with respect to the product formation (p_{Cl2}) when applied to a wide range of reactants partial pressures from 10^{-2} to 10^{2} bar at T = 573 K: (top) the model parameters are estimated by fitting to the available experiments and then employed for the entire range of pressures; (bottom) the parameters at each partial pressure in the plot are calculated accordingly using DFT. The black rectangle indicates the region for which reported experiments are available.[36]

In this study, we have scaled up the three above-mentioned microscopic kinetic LHHW models and obtained two-dimensional maps of the activity and surface coverage at 573 K and 673 K. Here, a 2D-figure of the second LHHW micro-kinetic model (Cl_2-recom.

Model, at T = 573 K) is provided as an example, the activity map of which is shown in Figure 3.6. In the top figure, the model parameters are estimated by fitting to the available experiments; and in the bottom one, the parameters are the rate constants resulting from DFT-based calculations. Specifically, the barriers entering this model are the ones shown in Table 3.3, which do not comprise any Cl-Cl interactions apart from those intrinsically contained in the Cl_2 desorption process barriers with PBE functional value of $E_b = 2.0$ eV. The active region according to experiments are marked by the black rectangle. From the above figure, it can be seen that higher partial O_2 pressure would lead to higher activity.

If we only checked the experimental range shown in the black box of Figure 3.6, very little difference can be observed between the two activity maps. However, when the partial pressures of HCl and O_2 increased, the difference of the two maps becomes obvious. In particular, DFT-calculated rate constants are used as model parameters to fit the second LHHW micro-kinetic model, the activity map of which is much closer to the experimental results.[4,36] It can be concluded from Figure 3.6 that higher partial pressure of chlorine would be helpful to achieve higher activity for chlorine gas generation. Our results are in line with expectations as the reaction is assumed to be controlled by the surface Cl atoms, which indirectly confirms that O_2 dissociation is the rate control step of the reaction.

Figure 3.7 illustrates the surface coverages of the most abundant surface intermediates on $RuO_2(110)$ at 573 K and over the same range of pressures shown in Figure 3.6. The corresponding parameters in the kinetic model applied the rate constants from DFT calculations. Similar results are also achieved at 673 K (not shown). We found that only O and Cl species are populated at the surface in an appreciable amount under the reaction conditions. Including the pressure range representative of the recent experiments, the figure of surface coverage predicts a coverage of more than 90% Cl species, with the remaining 10% covered with O species. On average, essentially all active sites are populated in the relevant reaction conditions. The low population of O species is thereby not a result of the on-going surface reactions, which would deplete O species faster than they can be replenished from the gas phase. Instead, it results from the weak O binding, which even in the complete absence of the HCl reactant would not sustain a much larger O population at the elevated temperatures of the Deacon process.

We have already mentioned that the two adsorption br and cus sites act differently in the formation of Cl_2. However, in our models these sites are not differentiated. In Figure 3.7, we can see that the surface coverage of Cl species is not sensitive to the partial pressure of the reactant O_2, and is mainly affected by the partial pressure of HCl. As long as the partial pressure of HCl reaches a certain level above 0.03 bar ($p_{HCl} \approx 10^{-1.5}$ bar), the surface coverage of Cl species will come to more than 40%, regardless of how the p_{O2} is. Therefore, the Cl species take up the majority during the entire reaction process. On the contrary, when p_{HCl} exceeds a certain amount with its increase, the coverage of O species is no longer affected by p_{O2}, but instead, the value is greatly reduced or even negligible. The depletion of O species is not due to oxygen desorption but water formation, the latter of which requires surface hydrogen from the preceding HCl dissociation processes, and therefore, the O coverage is sensitive to the HCl partial pressure. Moreover, the mean-field micro-kinetics indicates a 100% occupation of Cl species, and consequently zero percent coverage of O species on the active sites. This observation is beyond expectations of our kMC simulation results, which predict a coverage of 70% Cl_{cus} species and around 40% Cl_{br} species (unpublished results). It is therefore likely that the difference in the distribution of the surface species observed between the kMC and MF models is due to the underlying assumption of the rapid mixing of the species in the latter or the neglecting of the lateral interactions. Since the br site on the $RuO_2(110)$ surface is often occupied by O atoms with strong binding, the fact that the population of O coverage takes up only about 10% indicates that many of the O atoms at the br sites are replaced by Cl, confirming the presence of Cl_{br} under near-ambient reaction conditions. This so-called (self-)chlorination of the $RuO_2(110)$ surface has been testified by many experimental results[4,36,37] and theoretical predictions.[38,72]
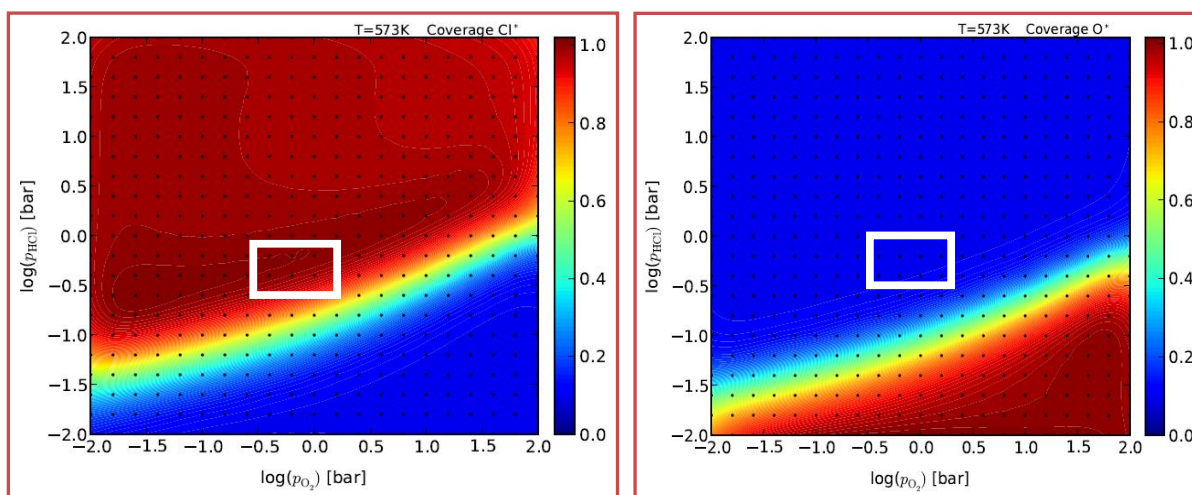
Figure 3.7 LHHW kinetic results for surface coverages (active site denoted by *) with the rate constants obtained using DFT over a range of partial pressures from 10^{-2} to 10^2 bar at T = 573 K, assuming both Cl*-Cl* recombination process with PBE functional value of E_b = 2.0 eV and Cl_2 recombination process as r.d.s. The white box marks pressure conditions employed in recent experimental studies.[4,36]

The surface coverages of the remaining OH, H_2O species and vacant sites are not explicitly shown here. At the elevated temperatures, we obtain a negligible water coverage on the surface, which is consistent with the experimentally reported surface water desorption temperatures around and above 400 K.[63,70,73] The surface population of OH species on the surface active sites is also found to be almost zero within the studied range of operating conditions. The negligible surface coverages of the H_2O, OH species, and active vacant sites have been also reflected in the previous Figure 3.5.

Combining Figure 3.6 and Figure 3.7, we observe that Cl* maintains the maximum surface coverage due to the lowest reaction rate of the Cl recombination step. With the small surface population of O*, the increase of Cl_2 production needs to amplify the feed O_2/HCl ratio, which is consistent with the experiments. According to our calculations, it can be predicted that the increase of the O surface coverage at high p_{O2} will lead to an increase of the reaction rate. There is a certain difference between our results obtained on the assumption underlying the mean-field microkinetics and that based on the kMC analog simulations. Any differences in comparison to the results of the kMC model arise thus out of the neglect of potential diffusion limitations at the

trench-like $RuO_2(110)$ surface[67,74] and the neglect of the additional Cl-Cl lateral interactions. The LHHW microkinetic modeling is restricted to the mean-field approach,[36,38] which is not able to account properly for the configurational control of the Deacon Process. Instead, the kMC simulations are highly required in order to better understand the catalytic activity as well as reaction mechanism.

3.4 Conclusion

In this work, we obtained three LHHW micro-kinetic models of the Deacon reaction at the $RuO_2(110)$ surface, each of them corresponding to a different rate-determining step. Multiple kinetic parameter sets can be obtained by fitting these rate equations to experimental data, all resulting in a full agreement with the limited set of data available. The fitted rate constants do not have any microscopic meaning, but merely represent effective parameters. As an alternative, we therefore used first-principles theory to determine the rate-determining step.

Employing corresponding first-principles calculated rate constants in the three LHHW models, allowed to clearly differentiate that only the LHHW model assuming Cl_2 recombination as the r.d.s. leads to agreement with experiment. We also observed that at typical reaction conditions, the surface is extensively chlorinated; thus, the active material is better described as a surface oxy-chloride.

Chapter 4

First-principles computational screening of dopants to improve the Deacon process over RuO$_2$

4.1 Introduction

As we mentioned in the first chapter, chlorine is regarded as one of the most important raw chemical materials for our daily life and industry production. The significance of using chlorine ranges from cleansing our everyday water to being critical for food, pharmaceuticals, transport, electronics, and telecommunications. Therefore, the oxidation of HCl to produce Cl$_2$ gas with only water as by-product has appeared as a promising and eco-friendly route to chlorine manufacture. Among the current recycling processes for converting HCl to Cl$_2$, catalytic oxidation of HCl, which is also known as Deacon process and initially developed by Henry Deacon in the 19th century,[12] constitutes a fundamentally important type of method for chlorine production in industry, and it has been widely used throughout the world.

Conventional catalysts used for this so-called Deacon process, such as CuO/CuCl$_2$, suffer from rapid activity loss and instability in the corrosive HCl environment at elevated process temperatures above 700 K.[3,75] In recent years, the Deacon catalytic system has been largely improved from the original CuO/CuCl$_2$ to the RuO$_2$-based catalyst, which is currently identified as the best Deacon catalyst owing to its correspondingly higher catalytic activity and thermodynamic stability.[16,17] An important progress towards the industrial production of chlorine was made by Sumitomo Chemicals using this RuO$_2$ catalyst coated on rutile TiO$_2$.[17,26] However, the recent work performed by I. C. Man et al. proved that the catalytic activity of a single RuO$_2$ catalyst may not be easily improved, because its oxygen dissociation energy is already at the optimum.[38,76]

The reaction mechanism on RuO_2 was investigated by us (cf. Chapter 3) and by other research groups to fit a LHHW kinetic model with the recombination of adsorbed Cl atoms to form Cl_2[15,36,63] or Cl-Cl recombination together with O_2 dissociation[38,76] as the rate-determining step(s). In particular, the latter microkinetic work by Studt *et al.* argued that the O-bonding properties of RuO_2 bring this material already very close to optimum catalytic activity.[38] Taking this aspect into account, we suppose that the incorporation of a small amount of non-precious additives or dopants into RuO_2 appears as a promising route. Due to scaling relations between the binding of O* and Cl*[38], such dopants would act similarly on both reaction intermediates and one would specifically aim for dopants that somewhat weaken the interaction with the surface.

Incorporation of dopants into the RuO_2 surface has already provided a good opportunity to enhance the catalytic activity of RuO_2, and been broadly applied to various chemical processes, such as oxygen evolution (OER), hydrogen evolution (HER), and chlorine evolution (CER). For instance, González-Huerta et al. demonstrated that Co-doped RuO_2 catalysts exhibit a significant improvement in catalytic activity towards the OER process in comparison with the undoped system.[77] Krtil et al. found the electrocatalytic performance of RuO_2 electrodes in OER and chlorine evolution significantly affected by Fe-, Ni-, and Zn-dopants.[78-80] And Zhuiykov emphasized the sensing properties of nanostructured Pt-doped RuO_2 electrodes.[81] Considering the above literature results, we realize that a doping strategy on RuO_2 appears as a very promising route as metal dopants can greatly improve the activity of the catalyst.

With this motivation we here embarked on a density-functional theory (DFT) based computational screening study, exploring the effect of a variety of metal dopants for the Deacon process over RuO_2. Focusing on the abundant RuO_2(110) facet, we employ a multi-descriptor approach that evaluates both the dopant effect on the catalytic activity and on catalyst/dopant stability. As an activity descriptor, we use the rate-controlling Cl desorption energy (ΔE_{Cl-des}), which due to the existing scaling relations also assesses the O binding, as well as kinetic barriers to Cl desorption.[38] Meanwhile, stability is an equally important factor. To this end, we calculate the dopant surface segregation energy (ΔE_{Seg}) and the stability against dopant precipitation into bulk metal grains. In the oxygen-rich environment of the Deacon process, it turns out though that the stability against dopant precipitation into bulk oxide grains represents a condition that is much harder to meet. From the metal dopants tested, only Cu is able to fulfill

all stability requirements, while simultaneously inducing the desired weakening of reaction intermediate binding.

4.2 Computational details

All DFT calculations have been performed with the plane-wave pseudopotential code CASTEP (CASTEP-6.0 version).[68] Electronic exchange and correlation were treated within the generalized gradient approximation (GGA) functional[82] due to Perdew, Burke, and Ernzerhof (PBE).[48] The Revised-Perdew-Burke-Ernzerhof (RPBE)[83] functional was also applied to review in the preliminary screening the chlorine (Cl) desorption energy ($\Delta E_{\text{Cl-des}}$) and surface segregation energy (ΔE_{Seg}), vide infra. Bulk calculations and reference calculations for the free molecules (Cl_2, O_2) were carried out in a spin-polarized manner. Surface calculations for $RuO_2(110)$ were performed non-spin-polarized.

Lattice constants of bulk RuO_2, as well as of the various bulk metals and bulk oxides formed by the dopant atoms were fully optimized. In the next part of this chapter, we provide the obtained lattice parameters and bulk oxide heats of formation, as well as the specific computational settings (plane wave cutoff, k-points) that were employed for the different systems. Our theoretical data achieves good agreement with the experimental literature data throughout. Doped bulk lattices were fully optimized until residual forces fell below 0.05 eV/Å. The same ionic relaxation criterion was employed in the surface calculations, under the constraint of a bottom trilayer that was frozen to the optimized bulk positions. Systematic tests indicated a numerical convergence of all energetic formation and segregation energies, as shown in the Eqs. 4.1-4.4 below, to within 50 meV at the employed computational settings.

4.2.1 Preliminary screening: Cl desorption and segregation energy

In our preliminary screening, we performed all the calculations within periodic boundary condition supercells. Free molecules were placed into a rectangular box of

dimensions (13 Å x 11 Å x 10 Å) with Gamma point sampling. $RuO_2(110)$ slabs consisted of four O-(Ru_2O_2)-O trilayers and were separated by 30 Å of vacuum space. There were eight atoms in each atomic layer corresponding to a (1x2) surface unit cell (Figure 4.1) which included two cus (coordinatively unsaturated sites) sites and two br (bridge) sites. We simulated M-doped $RuO_2(110)$ by replacing one Ru atom on the cus or br site with another 22 metals in the surface slab (M = La, Ir, Zr, Pt, Sn, V, Ti, Si , Co, Cu, Cr, Fe, Mn, Ni, Al, Pd, Ce, Zn, Ag, Pb, Ca and K). As shown in Figure 4.2, we restricted the location of the M atom only to the first and third layers of the $RuO_2(110)$ surface slab, with the latter position mimicking bulk-like behavior. All atomic positions within two top trilayers, as well as the adsorbates (two chlorine atoms), were fully relaxed until the residual forces on the atoms were less than 0.05 eV/Å. Brillouin zone integration was carried out on a (6x6x1) Monkhorst-Pack grid, and the plane wave cut-off energy was converged at 450 eV. This approach ensured that the total energies are converged within 0.02 meV per atom.

In light of the limiting nature of the Cl-Cl recombination step in the Deacon process over RuO_2 and the scaling relations between O* and Cl* binding, the Cl desorption energy, $\Delta E_{Cl\text{-}des}$, from the abundant $RuO_2(110)$ facet[84] appears as a suitable reactivity descriptor to assess the effect of metal dopant atoms on the catalytic process. We define this desorption energy as

$$\Delta E_{Cl-des} = \frac{1}{2}\left(E_{M@RuO_2(110)-2Cl} - E_{M@RuO_2(110)} - E_{Cl_2}\right). \quad (4.1)$$

Here, $E_{M@RuO2(110)-2Cl}$ is the total energy of the M-doped $RuO_2(110)$ surface with two adsorbed Cl atoms, $E_{M@RuO2-(110)}$ is the total energy for the corresponding clean (M-doped) $RuO_2(110)$ surface, and E_{Cl2} is the total energy of an isolated Cl_2 gas-phase molecule. In the employed sign convention, a negative $\Delta E_{Cl\text{-}des}$ indicates an exothermic surface adsorption. During our research, we only simulated the dopant metals at sites in the slab surface. For example, the dopant atom replaces one of the surface Ru atoms at the cus or br sites at the first layer.

For a preliminarily fast assessment of the stability of the dopant metal in the $RuO_2(110)$ surface, we assume that the dopant prefers to stay at the $RuO_2(110)$ surface rather than stay inside the bulk. At little additional computational cost, the generated data

for $E_{\text{M@RuO2-(110)}}$ can also be used to evaluate a first dopant stability descriptor, namely the dopant surface segregation energy ΔE_{seg}. This quantity was obtained by evaluating the total energy difference between the dopant atom at the surface and that at the bulk inside as the following:

$$\Delta E_{\text{seg}} = E_{M@RuO_2(110)} - E_{M@RuO_2,\text{bulk}} . \quad (4.2)$$

Here, $E_{\text{M@RuO2}}$, bulk is the total energy of the M dopant atom in the bulk of RuO₂, which we numerically obtain by substituting a Ru atom in the third trilayer of RuO₂(110) slab with a dopant atom. For each ΔE_{seg} calculation, the dopant in the first layer and third layer should be located at exactly the same cus or br sites at the same time. A segregation energy $\Delta E_{\text{seg}} < 0$ hereby indicates a preference for the dopant to segregate to the surface, which means the more negative the value is, the more the   dopant is enriched at the surface.
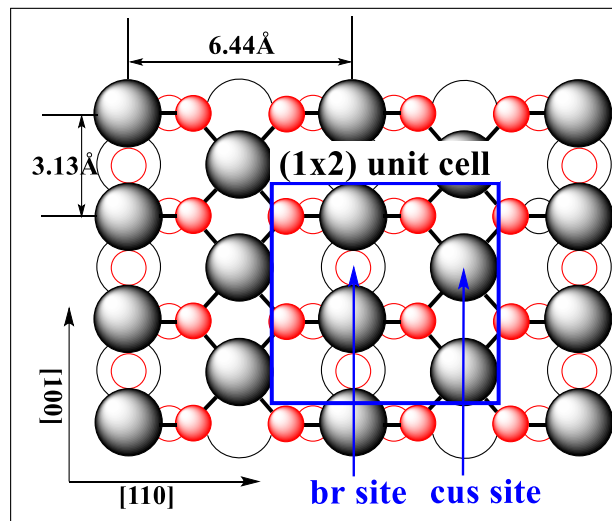

Figure 4.1 Top view of the RuO₂(110) surface, illustrating the location of the prominent br and cus adsorption sites offered by the O-poor termination. The blue solid rectangle shows the size of the employed (1x2) surface unit cell. Large gray spheres represent Ru atoms, small red spheres represent O atoms.
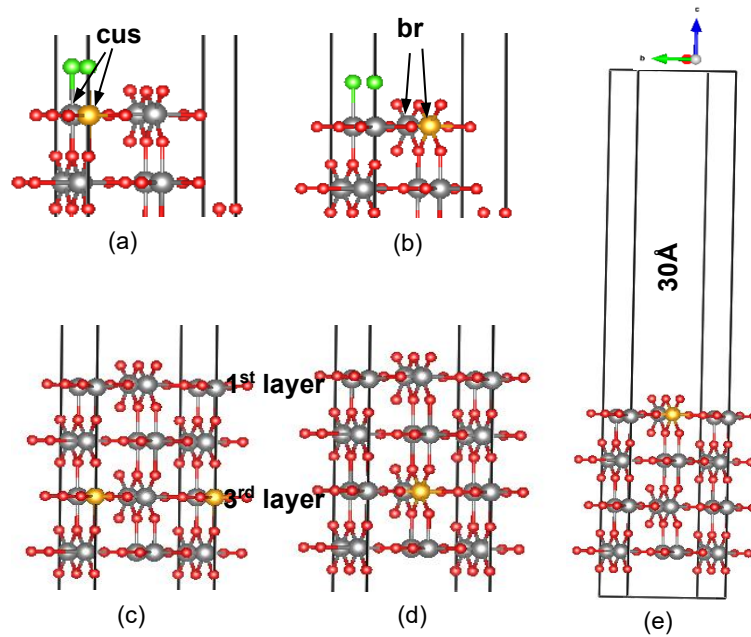
Figure 4.2 The (1x2) slab of the M-doped RuO$_2$(110) surface for DFT calculations (Cl adsorption energy and surface segregation energy). Here, we take copper (Cu) as the dopant for example, i.e. M is copper (Cu). Solid lines represent the limits of the unit cell. Gray spheres represent Ru atoms, red spheres represent O atoms, orange spheres denote Cu atoms, and green ones are Cl atoms. (a) and (b) side view of the Cu-doped RuO$_2$(110) surface showing the two chlorine atoms adsorption over the two neighboring cus sites while the copper atom replaces one of the surface Ru atoms at the one cus or br site, respectively. (c) and (d) side view of the clean Cu-doped RuO$_2$(110) surface while the dopant Cu atom exchanges one Ru atom at cus or br site at the third layer, respectively. (e) Full view of the slab used for the calculations showing the vacuum space between slabs.

4.2.2 Stability considerations

To in-depth evaluate the stability, we focus on some of the most promising metals as dopants on the basis of the preliminary screening. We first assess the stability of the dopant at different bulk cells, that is to say, the dopant in different "concentrations". In our study, concentration represents the dopant impurity related to the host Ru atoms in the slab. We built three supercells of RuO$_2$(110), and their sizes range from (1x1x1), (2x2x2) to (3x3x3). For the M-doped RuO$_2$(110) structures, we utilized one

doped metal atom to replace one Ru atom in the pure RuO_2 bulk cell (Figure 4.3) and then performed the geometry optimization with the utilization of the same plane-wave cutoff energy of 450 eV for pure RuO_2(110) and the relevant doped structures. To obtain the same k-point density in the reciprocal space for bigger supercells, the number of k-points was reduced accordingly. The Brillouin zone integration employed (12x12x18), (6x6x9), and (4x4x6) Monkhorst-Pack k-point mesh for (1x1x1), (2x2x2) and (3x3x3) bulk calculations, respectively.
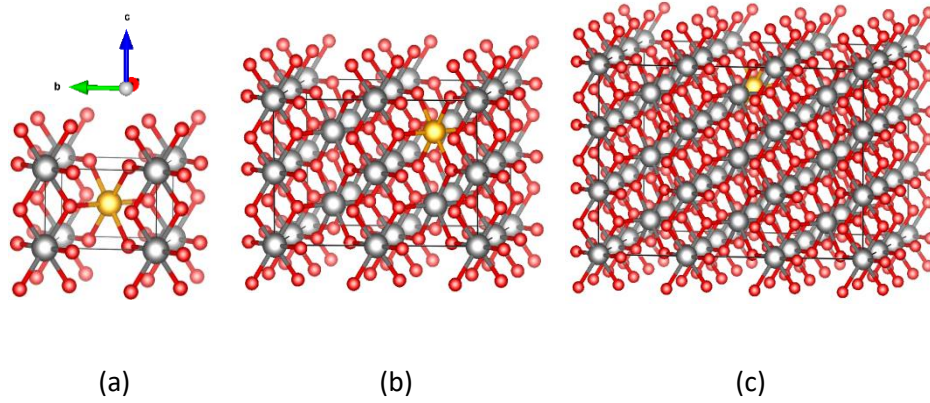
Figure 4.3 Three M-doped bulk RuO_2 supercells. Solid lines represent the limits of the supercell. Gray spheres represent Ru atoms, red spheres represent O atoms, and orange spheres denote the dopant atoms. (a) (1x1x1) unit cell; (b) (2x2x2) unit cell; and (c) (3x3x3) unit cell.

To assess the stability of the doped RuO_2 surface in different dopant concentrations, the bulk formation energies of the M-doped RuO_2 bulk cell were calculated according to Equation 4.3

$$\Delta G_{form,metal} = E_{MRu_{i-1}O_{2i}}^{bulk} - \left[E_{Ru_iO_{2i}}^{bulk} + E_M^{bulk} - E_{RuO_2}^{bulk} + \left(E_{O_2(g)} + \Delta\mu_{O_2}(T,p)\right)\right]. \quad (4.3)$$

Where $E_{MRu_{i-1}O_{2i}}^{bulk}$ represents the total energy of the M-doped RuO_2 supercell, in which one Ru atom has been substitutionally replaced by the dopant atom M. $E_{Ru_iO_{2i}}^{bulk}$ is the total energy of the corresponding undoped RuO_2 bulk supercell. E_M^{bulk} is the total energy of a dopant atom in its bulk metal state, and $E_{RuO_2}^{bulk}$ is the total energy of a primitive RuO_2 bulk cell, i.e. (1x1x1) bulk cell. "i" denotes the number of Ru atoms in the pure RuO_2 bulk cell, and its value is equal to 2 ($2x1^3$), 16 ($2x2^3$), and 54 ($2x3^3$) for the (1x1x1),

(2x2x2) and (3x3x3) bulk supercells, respectively. $E_{O2(g)}$ is the total energy of one isolated O_2 molecular in the gas phase. $\Delta\mu_{O2}$ *(T,p)* is the relative chemical potential of O_2 molecular in the gas phase, which is performed to assess the stability of the similar M-doped rutile TiO_2(110) surface at standard conditions.[85] Here we calculated the bulk formation energy of the doped system at 1 atm pressure and temperature ranges from 300 K to 1000 K. The $\Delta\mu_{O2}(T,p)$ value in different temperatures can be obtained from the previous references.[86,87] According to Equation 4.3, a negative value indicates that the formation is exothermic (stable) with respect to the pure RuO_2 surface. The more negative the $\Delta G_{form,metal}$ value is, the more thermodynamically favorable for doping. Therefore, in the present sign convention, a $\Delta G_{form,metal} < 0$ indicates a thermodynamic preference for the doped state.

In the oxygen-rich environment of the Deacon process phase separation could also proceed into undoped RuO_2 and a bulk dopant oxide. The sign $\Delta G_{form,metal}$ thereby has also been introduced as another important descriptor in our study, to judge the stability of dopant form in rich oxygen condition. Analogous to Equation 4.3 we therefore also assess

$$\Delta G_{form,oxide} = E_{M@RuO_2}^{(3x3x3)} - \left[E_{RuO_2}^{(3x3x3)} + \frac{1}{x} E_{M_xO_y}^{(1x1x1)} - E_{RuO_2}^{(1x1x1)} + \left(1 - \frac{y}{2x} \right)\left(E_{O_2(g)} + \Delta\mu_{O_2}(T,p) \right) \right]$$

That is

$$\Delta G_{form,oxide} = E_{M@Ru_{53}O_{108}}^{bulk} - \left[E_{Ru_{54}O_{108}}^{bulk} + \frac{1}{x} E_{M_xO_y}^{bulk} - E_{RuO_2}^{bulk} + \left(1 - \frac{y}{2x} \right)\mu_{O_2(g)} \right], \quad (4.4)$$

Where $E_{M_xO_y}^{bulk}$ is the total energy of a primitive bulk cell of the oxide M_xO_y formed by dopant M. Here three cases are included: (1) x = 1, y = 2; (2) x = y = 1; (3) x = 2, y = 1. The superscript (1x1x1) and (3x3x3) refer to the corresponding bulk supercells. For example, $E_{M@RuO_2}^{(3x3x3)}$ represents the total energy of the (3x3x3) M-doped RuO_2 bulk supercell, in which one ruthenium atom is replaced by the single one dopant atom on the basis of (3x3x3) pure RuO_2 supercell. Again, $\Delta G_{form, oxide} < 0$ indicates dopant stability.

For the above three metal oxides cases, the expression of $\Delta G_{form,\ oxide}$ can be specifically shown as below:

(1) x = 1, y = 2, M_xO_y is MO_2.

$$\Delta G_{form,oxide}(MO_2) = E_{M@Ru_{53}O_{108}}^{bulk} - \left[E_{Ru_{54}O_{108}}^{bulk} + E_{MO_2}^{bulk} - E_{RuO_2}^{bulk} \right]. \quad (4.4.1)$$

(2) x = y = 1, M_xO_y is MO.

$$\Delta G_{form,oxide} = E_{M@Ru_{53}O_{108}}^{bulk} - \left[E_{Ru_{54}O_{108}}^{bulk} + E_{MO}^{bulk} - E_{RuO_2}^{bulk} + \frac{1}{2}\mu_{O_2(g)} \right]. \quad (4.4.2)$$

(3) x = 2, y = 1, M_xO_y is M_2O.

$$\Delta G_{form,oxide} = E_{M@Ru_{53}O_{108}}^{bulk} - \left[E_{Ru_{54}O_{108}}^{bulk} + \frac{1}{2}E_{M_2O}^{bulk} - E_{RuO_2}^{bulk} + \frac{3}{4}\mu_{O_2(g)} \right]. \quad (4.4.3)$$

$E_{M@Ru_{53}O_{108}}^{bulk}$ Here, is the total energy of a (3x3x3) RuO_2 bulk supercell, in which one Ru atom is substitutionally replaced by the dopant atom M. $E_{Ru_{54}O_{108}}^{bulk}$ is the total energy of the corresponding undoped (3x3x3) bulk supercell, E_M^{bulk} is the total energy of a dopant atom in its bulk metal state, and $E_{RuO_2}^{bulk}$ is the total energy of a primitive RuO_2 bulk cell. The chemical potential of O_2 in the gas phase $\mu_{O_2(g)}(T,p) = E_{O_2} + \Delta\mu_{O_2}(T,p)$ is given by the total energy of an isolated O_2 molecule E_{O_2} and a temperature and pressure dependent part, $\Delta\mu_{O_2}(T,p)$, which we obtain from thermodynamic tables.[85,86] With this definition $\Delta G_{form,metal}$ evaluates the stability of the substitutionally doped system against phase separation into undoped RuO_2 and the bulk dopant metal at the given oxygen environmental conditions. In the present sign convention, a $\Delta G_{form,metal} < 0$ thereby indicates a thermodynamic preference for the doped state.

To ensure the accuracy of the total energies used in the above Equation 4.4, we calculated the heats of formation of metal oxides compared with the experimental data as a pre-verification calculation. The theoretical calculations about the heat of formation of metal oxide are generally associated with the stability of the bulk oxide.[86,88,89]

We already know the stable condition[86,88,89] for a bulk oxide in a pure oxygen gas phase

$$g_{M_xO_y}^{bulk} < xg_M^{bulk} + y\mu_O \qquad (4.5)$$

where $g_{M_xO_y}^{bulk}$ and g_M^{bulk} are the Gibbs free energy per formula unit of the final metal oxide bulk and pure metal bulk, respectively. Here μ_O is defined as $1/2E_{O2(g)} + \Delta\mu_O$ since the oxygen chemical potential is relative to the total energy of an oxygen molecule, so the above Equation 4.5 can be written as

$$\Delta\mu_O \geq \frac{1}{y}\left(g_{M_xO_y}^{bulk} - xg_M^{bulk} - \frac{y}{2}E_{O_2}^{total} \right) = \frac{1}{y}\Delta H_f(T = 0K) \qquad (4.6)$$

Where $E_{O_2}^{total}$ is the total energy of the oxygen gas phase, and ΔH_f (T = 0 K) refers to the heat of formation of the bulk oxide at T = 0 K.[89-91]

In our study, we calculated the heat of formation of bulk oxides by using the total energy as a replacement to the Gibbs free energy in Equation (4.6), neglecting the vibrational and entropic contributions to ΔH_f (T,p).[88,92] So we defined the calculated heat of formation for the bulk oxide as follows.

$$\Delta H_f(T = 0K) = \Delta E_f(cal.) \approx E_{M_xO_y}^{bulk} - xE_M^{bulk} - \frac{y}{2}E_{O_2(g)} \qquad (4.7)$$

Here, ΔE_f (cal.) and ΔE_f (exp.) represent the calculated and experimental heat of formation, respectively.

The original crystal structures of the involved metals and metal oxides in $\Delta G_{form,metal}$ (see Equation 4.3), $\Delta G_{form,oxide}$ descriptor (see Equation 4.4), and ΔE_f (cal.) (see Equation 4.7) were obtained from references,[93,94] and all the geometries were optimized within GGA-PBE. In addition, we employed a suitable plane-wave cutoff energy and k-point set for each metal and metal oxide bulk as confirmed by the convergence test. The set of cutoff energy and k-points in details are listed in Table 4.1.

Table 4.1 k-Points and cutoff energy for metal and oxide bulk calculations.

Metal/Metal Oxide	k-points	$E_{cut\text{-}off}$ / eV
Ag	8x8x8	550
K	12x12x12	450
Cu	10x10x10	650
Zn	22x22x11	550
Ca	8x8x8	650
Ru	11x11x6	650
Ag_2O	6x6x6	450
K_2O	6x6x6	650
KO_2	5x5x4	650
CuO	6x8x6	650
Cu_2O	7x7x7	650
ZnO	7x7x5	650
CaO	6x6x6	650
RuO_2	6x6x9	650

4.3 Results and discussion

4.3.1 Preliminary screening: activity & stability I

As shown in Figure 4.1, the O-poor termination of RuO_2(110) exhibits two prominent high-symmetry adsorption sites. A so-called coordinatively unsaturated (cus) site atop a fivefold O-coordinated surface Ru_{cus} atom, and a bridge (br) site between two fourfold O-coordinated Ru_{br} atoms. Already moderate oxygen pressures are sufficient to stabilize terminal O_{br} atoms at all bridge sites (leading to the stoichiometric RuO_2(110) termination), whereas more O-rich environments are necessary to also have all cus sites occupied with O_{cus} atoms in the O-rich termination.[90,95] Even though there is evidence that Cl is able to partially substitute for O_{br} under reaction conditions,[11,34] we nevertheless consider the cus sites as an adequate active site model for our screening study.[96]

Our work in Chapter 3 confirmed the elementary Cl-Cl recombination step as the rate determining step.[4,36] Therefore it is reasonable to use the Cl desorption energy ($\Delta E_{Cl\text{-}des}$) as a descriptor to evaluate the activity of dopants. Likewise, the dopant surface segregation energy (ΔE_{seg}) of the dopant atom obtained from the DFT calculations could be used to determine whether the dopant prefers to stay at the surface or stay inside the bulk.[97,98] It has been applied as a preliminary index to assess the stability of potential metal dopants in the RuO_2(110) surface. We correspondingly evaluate the Cl_2 desorption energy by adsorbing two Cl atoms at the two empty cus sites in the (1x2) surface unit-cell of a stoichiometrically terminated RuO_2(110) slab. As potential dopants we screen a range of 22 metals (M = La, Ir, Zr, Pt, Sn, V, Ti, Si, Co, Cu, Cr, Fe, Mn, Ni, Al, Pd, Ce, Zn, Ag, Pb, Ca and K), which substitutionally replace either a Ru_{cus} or a Ru_{br} surface atom (Figure 4.2). Based on equations 4.1 and 4.2, the corresponding Cl desorption energy ($\Delta E_{Cl\text{-}des}$) and surface segregation energy (ΔE_{seg}) of the M-doped RuO_2(110) surface are calculated, and two-dimensional cross plots with Cl desorption energy as X-coordinate and dopant surface segregation energy as Y-coordinate are generated to illustrate the doping effect (Figure 4.4).

As already explained in Part 4.2.1, a negative $\Delta E_{Cl\text{-}des}$ value indicates an exothermic surface adsorption, representing high activity of the dopant, while a negative ΔE_{seg} indicates the preference for the dopant to stay at the surface with good stability. Figure

4.4 (a) and (b) shows that most of the crosses locate on the right side of the undoped ruthenium reference line (blue dotted line), indicating that the lowering of ΔE_{Cl-des} away from the undoped reference value is well pronounced when one of the surface Ru atom at the br or cus site is replaced by a dopant metal listed above. These results show that, in most cases, the activity of doped $RuO_2(110)$ in the Deacon process will be higher than pure $RuO_2(110)$. La, Ir, Pb, Cr-doped $RuO_2(110)$, and particularly La-doped $RuO_2(110)$, does not improve the activity, but instead, it greatly reduces the oxidation of HCl. Similarly, when an indium atom was doped into the cus position, it has the same negative effect. The vertical coordinates indicate most of the points are below the blue solid line (ΔE_{Seg} = 0 eV, except Fe, Al, Co, Ni doped at the br site), suggesting that most of these dopants prefer to be enriched at the surface rather than stay inside the middle of the bulk.

The left panel in Figure 4.4 compiles the obtained ΔE_{Cl-des} and ΔE_{seg} descriptor data for the metal dopant atoms replacing a Ru_{cus} surface atom. Compared to the also shown undoped $RuO_2(110)$ surface, almost all of the dopant candidates at Ru_{cus} sites lead to the desired weakening of the surface-Cl bond, which facilitates recombinative Cl_2 desorption. The lowering of ΔE_{Cl-des} away from the undoped reference value is in parts pronounced, and reaches a maximum of 0.8 eV for K. In particular for K, this goes hand in hand with a sizeable preference to segregate to the surface though. A ΔE_{seg} value beyond -7 eV raises first concerns regarding the stability of this dopant, to which we will return in Section 4.3.2. Based on their significant lowering of ΔE_{Cl-des} we nevertheless identify a group of five more promising dopant candidates: Cu, Zn, Ag, Ca, and K.

The right panel in Figure 4.4 shows much smaller decreases of the ΔE_{Cl-des} value (below 0.2 eV) for substitutional doping at Ru_{br} sites. This reveals that the effect of surface dopants is efficiently screened by the metallic character of the $RuO_2(110)$ surface. In a corresponding highly local view of doping, surface dopant atoms represent primarily the second type of dispersed active sites at the catalyst surface for direct coordination. Even though small, the lowering of ΔE_{Cl-des} at Ru surface sites in the immediate vicinity of such surface dopant sites may nevertheless also be a second, decisive factor, recalling that the bonding properties of RuO_2 were already considered near optimum.[63] The surface dopant site and its immediate vicinity may thus serve as areas of improved catalytic activity, which due to the high diffusion barriers at $RuO_2(110)$[90,95]

operate rather decoupled from the remaining undoped parts of the surface. At the quite consistently obtained negative dopant surface segregation energies, the concentration of these areas would be substantially higher than suggested by the nominal bulk doping concentration – as long as this segregation does not extend to demixing and dopant precipitation to which we proceed next.

(a)   (b)
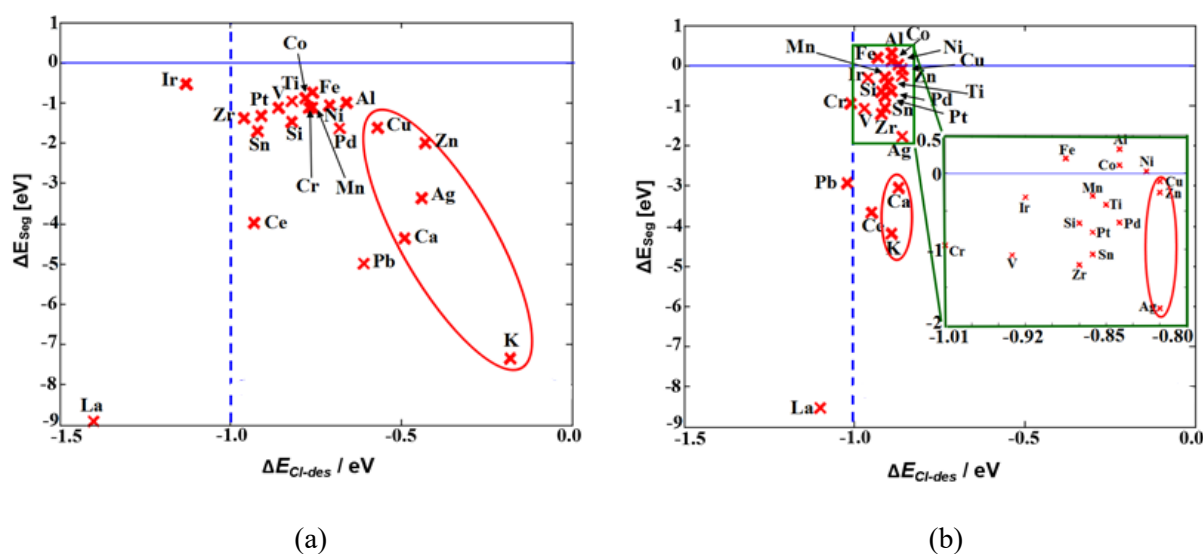
Figure 4.4 Calculated Cl desorption energy, $\Delta E_{Cl\text{-}des}$, and dopant surface segregation energy, ΔE_{seg}, for 22 metal dopant atoms at RuO$_2$(110). The Cl desorption energy at undoped RuO$_2$(110) is shown as blue dotted line. Promising dopants leading to a desired weakening of the Cl-surface bond fall to the right of this line. Five most promising candidates further considered in subsequent screening steps are circled in red (Cu, Zn, Ag, Ca and K). (a) (left panel) Data for substitutional doping at Ru$_{cus}$ site. (b) (right panel) Data for substitutional doping at Ru$_{br}$ site.

Here, it is noteworthy that the Pb-doped RuO$_2$(110) catalytic system shows a significant advantage in terms of activity and stability compared to most other metals, when Pb as the dopant locates at the cus site. However, its activity becomes even lower than the undoped condition when Pd locates at the br site (the point goes to the left-hand side of the Ru reference line). Thus, Pd should not be included in the promising dopant list.

In conclusion, with the two descriptors we can identify promising dopant candidates for the Deacon process over RuO$_2$(110). This points out that five metals (Cu, Zn, Ag, Ca,

and K) show particularly promising behavior either at cus sites or br sites, weakening the rate-determining Cl adsorption while showing an obvious preference to segregate to the surface. Meanwhile, we have also calculated the ΔE_{Cl-des} and ΔE_{seg} for the above 22 doped systems with RPBE xc-functional, which shows the same trend that obtained with PBE xc-functional.

4.3.2 Preliminary screening: activity & stability II

To testify the accuracy of our previous data (ΔE_{Cl-des} and ΔE_{Seg} with GGA-PBE level in part 4.3.1), we selected several metals (Ag, Zn, Cu, Ni, K, Al, Ti) from the above-mentioned 22 metals for substitutional doping of the RuO_2(110) surface, and recalculated their ΔE_{Cl-des} and ΔE_{seg} with the RPBE xc-functional. Taking into account the abundance and price of these metals as well as the calculated results at PBE level, we believe that Cu, Ag, Zn, and Ti are the best choices for substitutional doping at the Ru_{br} atom, while Zn, Ag, Cu, and Al are more promising dopants for substitutional doping at the Ru_{cus} atom. The corresponding energies of the above-mentioned promising dopants at br and cus sites with RPBE xc-functional were further recalculated. The optimized RuO_2 bulk geometry is shown in Figure 4.5. According to the bulk geometry, we can build a (1x2) RuO_2(110) unit surface cell consisting of four O-(Ru_2O_2)-O trilayers, which were separated by 30 Å of vacuum space. The vacuum region of 30 Å ensures the decoupling of the periodic slab images. From the table 4.2 below, we can see that the lattice parameters obtained by using PBE and RPBE xc-functional are quite similar.

Table 4.2 Lattice parameter changes between PBE and RPBE xc-functional

xc-functional	a(Å)	b(Å)	c(Å)
GGA-PBE	6.2560	6.3963	37.0000
GGA-RPBE	6.2556	6.4343	37.0000
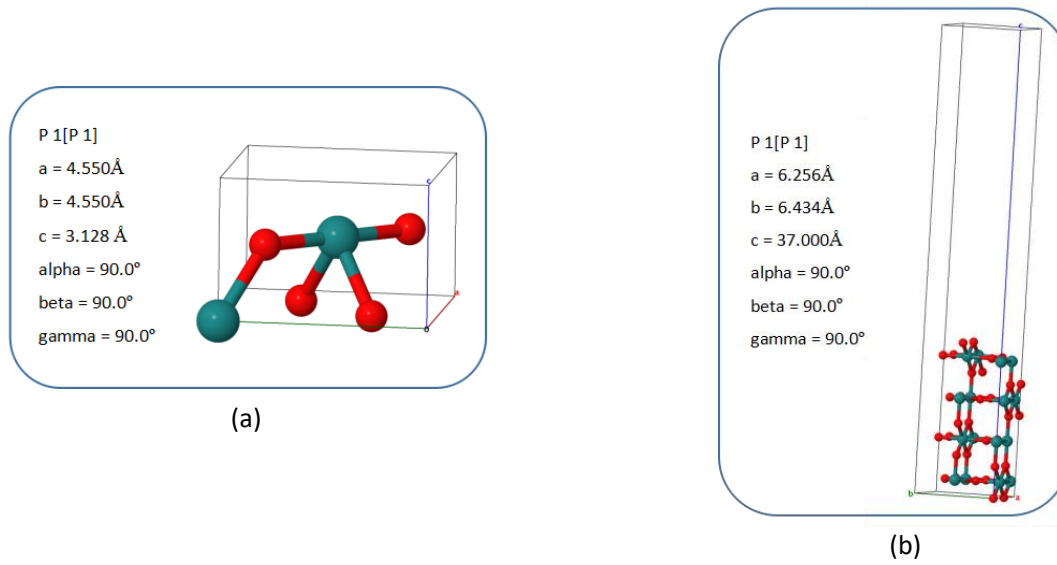
Figure 4.5 (a) The RuO$_2$ bulk geometry; (b) The (1x2) RuO$_2$(110) unit cell. Solid lines represent the limits of the unit cell. Dark blue spheres represent Ru atoms, red spheres represent O atoms.

With the new lattice parameter settings, we used Equation 4.1, 4.2 as well as the following Equation 4.8 to calculate the corresponding energies of M-doped RuO$_2$(110) surface at the RPBE level. Here, M represents Ag, Zn, Cu, Ni, K, Al, or Ti atom. In our DFT calculations, the energy barrier of the Cl$_2$ desorption process is 1.55 eV, which is similar to the results with RPBE functional by N. López et al. (E_d = 1.56 eV in the small p(2x1) supercell)[4] and D. Teschner et al (E_d = 1.54 eV).[36] Since the RPBE values for Cl-Cl recombination energy barrier are close to the reference data, we recalculated the above-chosen seven promising metals from our PBE results to dope the RuO$_2$(110) surface, and compared the difference between PBE and RPBE values. We can also refer to Figure 4.2 for the relevant structures required for calculating the detailed $\Delta E_{Cl\text{-ads}}$ and ΔE_{Seg} using the RPBE xc-functional. The Cl$_2$ desorption energy barrier on the surface including ½ ML dopant metal can be calculated

$$\Delta E_{barrier} = -2\Delta E_{Cl-des} = E_{M @ RuO_2(110)} + E_{Cl_2} - E_{M @ RuO_2(110)-2Cl} \quad (4.8)$$

where $E_{M@RuO2(110)-2Cl}$ is the total energy of the M-doped RuO$_2$(110) surface with two adsorbed Cl atoms, $E_{M@RuO2-(110)}$ is the total energy for the corresponding clean (M-doped) RuO$_2$(110) surface, and E_{Cl2} is the total energy of an isolated Cl$_2$ gas-phase

molecule. The calculated barriers have been used to compare with the experimental data. In the present sign convention, a more positive $\Delta E_{barrier}$ indicates a harder Cl-Cl recombination case.
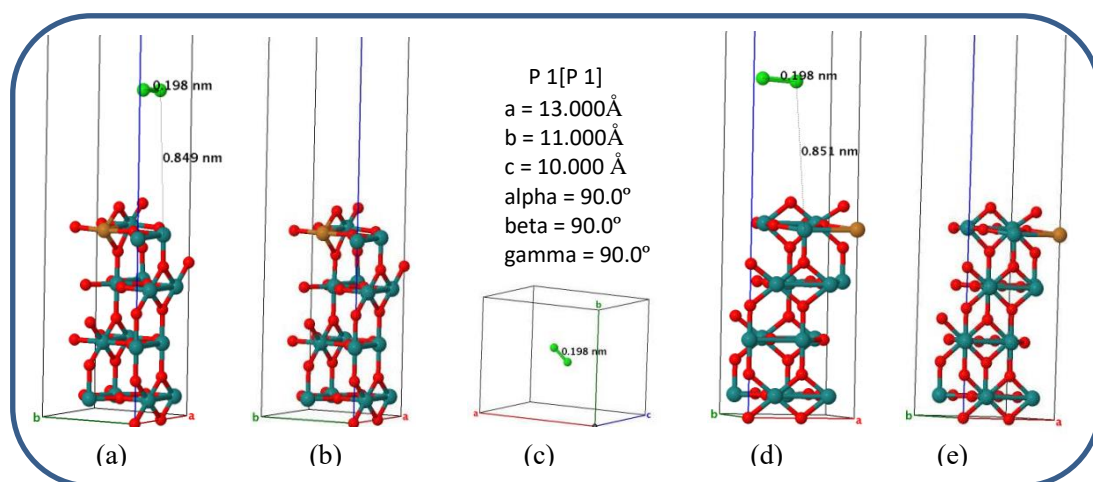
Figure 4.6 (a), (b) and (d), (e): The (1x2) slabs of the M-doped RuO_2(110) surface for Cl_2 desorption energy barrier ($\Delta E_{barrier}$), M is the dopant atom. (c) full view of the chlorine molecule bulk and the relevant lattice parameters. Solid lines represent the limits of the unit cell. Dark blue spheres represent Ru atoms, red spheres represent O atoms, orange spheres denote the dopant atom, and green ones are Cl atoms. The two sets of Figure (a), (b) and (c), (d) side view of the M-doped RuO_2(110) surface while the dopant atom replaces one of the surface Ru atoms at the one br or cus site at the top layer, respectively. (a) and (d) shows an illustration of a chlorine molecule desorbed from the M-doped RuO_2 (110) into the gas sphere. Jmol view.

We can calculate the three energies ($\Delta E_{barrier}$, ΔE_{Cl-des}, and ΔE_{Seg}) at the GGA-RPBE level for the dopant atom at one surface br and cus site, which is shown in Table 4.3 and 4.4, respectively. For $\Delta E_{barrier}$ and ΔE_{Cl-des} calculations, we only simulated the dopant metal to sit at the slab surface, i.e. the dopant atom replaces one of the surface Ru atoms at cus or br site at the top layer. The structures for substitutional doping at cus or br site at the third layer are used for ΔE_{Seg} calculations. From Figure 4.2 and 4.6, we can find the detailed illustrations of each geometry, whose total energy is required in the above DFT calculations. Cu can be still taken as a dopant example to exchange one of Ru_{cus} atoms over the RuO_2(110) surface for calculating $\Delta E_{barrier}$, ΔE_{Cl-des}, and ΔE_{Seg}, which can be shown in Table 4.4 for details.

The final calculated results for substitutional doping at br and cus site with RPBE xc-functional are listed in Table 4.3 and 4.4, respectively. Besides, in these two tables, we also compared the RPBE data with the previous PBE values, and found that the data calculated at the RPBE level is very close to the data at PBE level. No matter the atom dopes at either Ru_{br} site or Ru_{cus} site over the pure RuO_2(110) surface, the whole trend of the energies for these metals does not change. From the two tables we can realize that all the doped systems have lower energy barrier of the Cl-Cl recombination process than the undoped system, which means doping any of the Ag, Zn, Cu, Ni, K, Al, or Ti atom can significantly reduce the original energy barrier of the pure RuO_2(110) system. Substitutional doping of the above five metals at pure RuO_2(110) surface to lead the higher activity has been proved.

Table 4.3 The calculated energy barrier for the Cl-Cl recombination process ($\Delta E_{barrier}$), the Cl desorption energy per chlorine atom desorption (ΔE_{Cl-des}) on the surface including ½ ML dopant and the dopant surface segregation energy (ΔE_{Seg}) between ½ ML dopant on the 1st layer and that on the 3rd layer. (Substitutional doping at Ru$_{br}$ site). CASTEP-6.0, PBE and RPBE xc-functional, 450.00 eV cut-off energy.

Dopant	$\Delta E_{barrier}$ / eV		ΔE_{Cl-ads} / eV		ΔE_{Seg} / eV	
xc-functional	PBE	RPBE	PBE	RPBE	PBE	RPBE
Ru$_{br}$	2.02	1.53	-1.01	-0.77		
Ag	1.72	1.22	-0.86	-0.61	-1.78	-1.81
Zn	1.72	1.23	-0.86	-0.61	-0.26	-0.28
Cu	1.72	1.23	-0.86	-0.62	-0.11	-0.12
Ni	1.75	1.27	-0.87	-0.63	0.02	0.03
K	1.77	1.28	-0.89	-0.65	-4.20	-4.29
Al	1.79	1.31	-0.89	-0.65	0.31	0.32
Ti	1.80	1.31	-0.90	-0.65	-0.42	-0.41

Table 4.4 The calculated energy barrier for the Cl-Cl recombination process ($\Delta E_{barrier}$), the Cl desorption energy per chlorine atom desorption (ΔE_{Cl-des}) on the surface including ½ ML dopant and the dopant surface segregation energy (ΔE_{Seg}) between ½ ML dopant on the 1st layer and that on the 3rd layer.

Dopant	$\Delta E_{barrier}$ / eV		ΔE_{Cl-ads} / eV		ΔE_{Seg} / eV	
xc-functional	PBE	RPBE	PBE	RPBE	PBE	RPBE
Ru$_{cus}$	2.02	1.53	-1.01	-0.77		
Zn	0.88	0.48	-0.43	-0.24	-2.00	-1.96
Ag	0.89	0.52	-0.44	-0.26	-3.37	-3.43
Cu	1.16	0.70	-0.57	-0.35	-1.62	-1.59
Al	1.35	0.89	-0.66	-0.44	-1.00	-0.97
Ni	1.43	0.94	-0.71	-0.47	-1.07	-1.06
Ti	1.67	1.25	-0.82	-0.61	-0.96	-0.95

(Substitutional doping at Ru$_{cus}$ site). CASTEP-6.0, PBE and RPBE xc-functional, 450.00 eV cut-off energy.
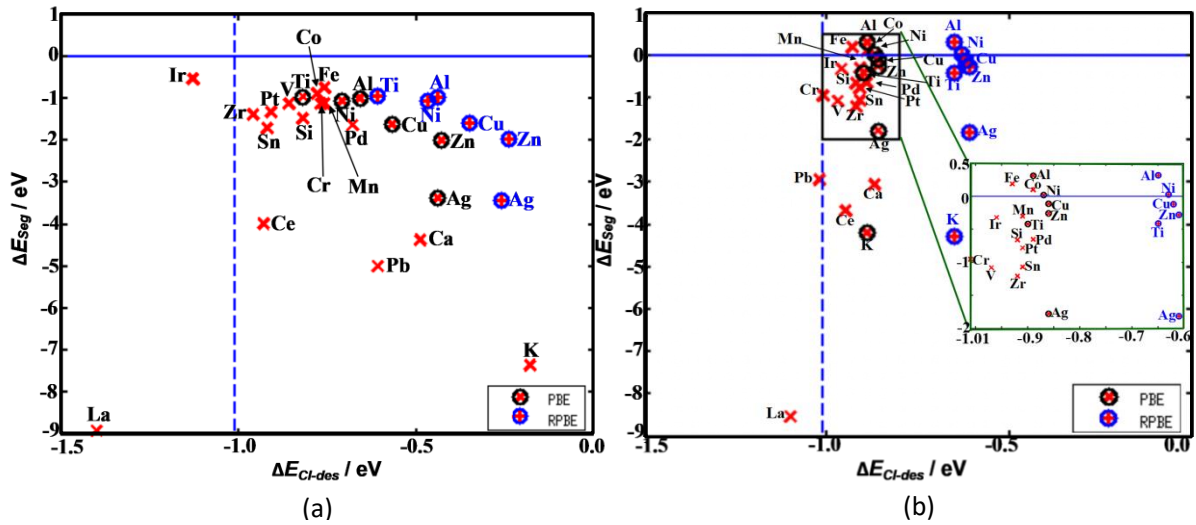
Figure 4.7 Calculated Cl desorption energy, $\Delta E_{\text{Cl-des}}$, and dopant surface segregation energy, ΔE_{Seg}, for 22 metal-doped RuO$_2$(110) surfaces. (1x2) RuO$_2$(110) unit cell, four layers, PBE xc-functional, 450 eV cut-off energy and 6x6x1 k-points. The Cl desorption energy at undoped RuO$_2$(110) is shown as the blue dotted line. We named it as Ru reference line. (a) and (b) panel: Data for substitutional doping at Ru$_{\text{cus}}$ and Ru$_{\text{br}}$ site, respectively. The data are circled in black and blue showing the calculated results with PBE and RPBE xc-functional, respectively.

At the same time, we compared the above-calculated results of $\Delta E_{\text{Cl-des}}$ and ΔE_{Seg} at the RPBE level with the data from Figure 4.4 so that we can get an intuitive comparison between RPBE and PBE levels. As shown in Figure 4.7, PBE values are much closer to the reference line in comparison with RPBE values. The calculated $\Delta E_{\text{Cl-des}}$ at the RPBE level are smaller with an approximate value of 0.2 - 0.3 eV than that at the PBE level. Meanwhile, the results of ΔE_{Seg} value are almost the same in these two figures, no matter whether they are at the RPBE or PBE levels. Even though differences exist, according to the locations of these metals in Figure 4.7, we can notice that the calculated results with the RPBE xc-functional also have the same trend as those with the PBE xc-functional regarding the ranking of activity and stability. Zn, Ag and Cu would be the best choices as the dopant to replace one of the ruthenium atom on the RuO$_2$(110) surface at the RPBE level. Hence, the RPBE values fully confirm the PBE results. We will correspondingly employ the PBE xc-functional in all of our subsequent computational screening steps in order to save computational resources.

65

The above-summarized Table 4.3, 4.4 and Figure 4.7 show that our calculated results at the PBE level stay the same with the data at the RPBE level. Besides, we also assessed the energy difference between a single point energy calculation and geometry optimization calculation. On the basis of the optimized RPBE lattice parameters, we simply took a Ag, Zn, Cu, Ni, K, Al, or Ti atom to dope into the optimized RuO_2(110) surface and did a single point calculation at the RPBE level. Table 4.5 and 4.6 present the comparison results between geometry optimization and single point energy data when the M (M = Ag, Zn, Cu, Ni, K, Al, or Ti) atom is substitutionally doping at Ru_{br} and Ru_{cus} sites, respectively. Only small differences were found between the geometry optimization and single point energy. But the energies calculated with geometry optimization in tables are obviously more accurate than that with the single point energy.

In summary, our results verified that RPBE values have basically the same rationality and accuracy as PBE values through the above comparisons. Last but not least, we conclude that Zn, Ag and Cu would be the best choices as the dopant to replace ruthenium atoms at the RuO_2(110) surface. Considering all these factors, we finally decided to use PBE as the xc-functional for all the subsequent calculations of the 22 doped systems.

Table 4.5 The energy barrier for the Cl_2 desorption process and the Cl binding energy on the surface including ½ ML dopant and the segregation energy between ½ ML dopant on the 1st layer and that on the 3rd layer. (Substitutional doping at Ru_{br} site.) castep version 6.0, RPBE xc-functional, 450.00 eV cut-off energy.

Dopant	$\Delta E_{barrier}$ / eV		$\Delta E_{Cl\text{-}ads}$ / eV		ΔE_{Seg} / eV	
TASK	GeoOpt	SinglePoint	GeoOpt	SinglePoint	GeoOpt	SinglePoint
Ru_{br}	1.55	1.53	-0.77eV	-0.77eV		
Ag	1.24	1.23	-0.62	-0.61	-1.78	-1.91
Zn	1.25	1.24	-0.62	-0.61	-0.33	-0.33
Cu	1.26	1.23	-0.63	-0.62	-0.19	-0.16
Ni	1.29	1.27	-0.64	-0.63	-0.01	0.00
K	1.30	1.27	-0.65	-0.64	-4.39	-4.43
Al	1.32	1.31	-0.66	-0.65	0.28	0.30
Ti	1.32	1.31	-0.66	-0.66	-0.44	-0.45

Table 4.6 The energy barrier for the Cl_2 desorption process and the Cl binding energy on the surface including ½ ML dopant and the segregation energy between ½ ML dopant on the 1st layer and that on the 3rd layer. (Substitutional doping at Ru_{cus} site.) castep version 6.0, RPBE xc-functional, 450.00 eV cut-off energy.

Dopant	$\Delta E_{barrier}$ / eV		$\Delta E_{Cl\text{-}ads}$ / eV		ΔE_{Seg} / eV	
TASK	GeoOpt	SinglePoint	GeoOpt	SinglePoint	GeoOpt	SinglePoint
Ru_{cus}	1.55	1.53	-0.77	-0.77		
Zn	0.45	0.43	-0.22	-0.21	-1.60	-1.97
Ag	0.45	0.44	-0.22	-0.22	-3.05	-3.44
Cu	0.67	0.66	-0.34	-0.33	-1.22	-1.60
Al	0.88	0.88	-0.44	-0.43	-0.57	-0.97
Ni	0.93	0.93	-0.47	-0.46	-0.67	-1.06
Ti	1.16	1.19	-0.58	-0.58	-0.59	-0.95

4.3.3 Depth screening: stability considerations I

Since we have already verified that, in most of the cases, substitutional doping at the RuO$_2$(110) surface with another metal can indeed enhance the Deacon catalytic activity compared to the pure RuO$_2$(110) surface, the stability becomes a very important criterion to assess the accessibility of the dopants. Therefore, in-depth consideration of thermodynamic stability is indispensable. Based on the above calculation results and kinetic analysis, we identified five promising doping candidates and will continue considering their stability in the Deacon process. For this, we will use the combination of thermodynamics and DFT studies to identify the most stable dopant.

For the solid-state dopants in practice, it is difficult to predict the location and quantity of the dopants on the RuO$_2$(110) surface, and ensure the whole concentration to be consistent.[99,100] To a great extent, the concentration of metal dopants always affects the catalytic activity and stability. Therefore, we focus on these five metals (Cu, Zn, Ag, Ca, and K), which exhibit weaker bonding between Cl and surface atom, as well as stronger surface segregation. We will study their stability at different concentrations. In addition, we should notice that the reaction condition (temperature, pressure, etc.) also have a great effect on the Deacon process, especially on the reaction rate of Cl$_2$ production, reaction mechanism, and RuO$_2$ catalytic structure.[4,74]

Through Equation 4.3 we can calculate the bulk formation energies of the five doped systems with different temperatures and concentrations. In all our bulk calculations within the DFT-GGA approach, the optimized lattice constants of the unit cells are obtained and shown in Table 4.7 and 4.8, which are in good agreement with the experimental lattice constants as well as other theoretical data. Besides, our results are even closer to the experiments than the literature data.

Table 4.7 Calculated DFT-GGA and literature a_0, b_0, c_0 lattice parameters (Å) for Ca, Zn, Ag, K, Cu, and Ru metals. The theoretical reference values for Zn and Ru were obtained within the LDA.

Dopant	Experiment[a]		Theory			
			Ref.		This work	
Ca	a_0	5.58	a_0	5.50[b]	a_0	5.53
Zn	a_0	2.66	a_0	2.58	a_0	2.63
	c_0	4.95	c_0	4.79[c]	c_0	5.01
Ag	a_0	4.09	a_0	4.10[d]	a_0	4.14
K	a_0	5.32	a_0	5.30[e]	a_0	5.32
Cu	a_0	3.61	a_0	3.64[f]	a_0	3.63
Ru	a_0	2.71	a_0	2.75	a_0	2.72
	c_0	4.28	c_0	4.37[g]	c_0	4.28

[a] *Reference 93.*   [b] *Reference 96.*   [c] *Reference 101.*   [d] *Reference 102.*   [e] *Reference 103.*
[f] *Reference 104.*   [g] *Reference 105.*

To assess the stability of the dopants with different concentrations, we simulated three different bulk supercells: (1x1x1), (2x2x2), and (3x3x3) bulk cells, as shown in Figure 4.3. The concentration of the doping metal atom (the metal impurities relative to the host Ru atoms in the slab) in (1x1x1), (2x2x2) and (3x3x3) cell is 50% ($MRuO_4$), 6.25% ($MRu_{15}O_{32}$), and 1.85% ($MRu_{53}O_{108}$), respectively. During the bulk calculations, we added the relative chemical potential of molecular O_2, $\Delta\mu_{O2}(T,p)$, in Equation 4.3 instead of only applying the total energy of O_2, which can be only used to evaluate physical quantities at T = 0 K and p = 0 atm. Because of the addition of oxygen chemical potential, we are able to take into account the effect of temperature and pressure while considering the influence of the doping concentration. This allows us to obtain the trends of the bulk formation energy at different temperatures, and better identify the stability of five doped RuO_2 systems. Thus, more insights into the behavior of the M-doped RuO_2 system can be obtained.

In principle, if the $\Delta G_{form,metal}$ value is more negative, it means that the substitutional doping process is more thermodynamically favorable, and the M-doped RuO_2 surface is more stable. Figure 4.8 compiles the calculated $\Delta G_{form,metal}$ data of the five promising doping candidates identified in the previous section. We evaluated their stability over a temperature range from room temperature to 1000 K under standard pressure

condition. Among the five metals, Ag is the only one that exhibits a large positive formation free energy, indicating a thermodynamic instability of substitutional Ag dopants against precipitation into Ag bulk particularly at the elevated temperatures above 700 K employed in the Deacon process.

From Figure 4.8 we realize that the $\Delta G_{form,metal}$ values of each metal dopant become smaller along with the increase of the supercell sizes, indicating that lower doping concentration increase the stability of the M-doped RuO_2 system. For (1x1x1) supercells in Figure 4.8 (a), the $\Delta G_{form,metal}$ values of calcium, zinc, and copper-doped RuO_2 systems are still negative (at temperatures below 700 K). So we can conclude that, with high doping concentration, the three M-doped RuO_2 systems (M is Ca, Zn, and Cu) remain stable at temperatures T < 700 K. Figure 4.8 (b) shows us that the $\Delta G_{form,metal}$ value of potassium changes the most, when the doping concentration of potassium decreases from 50% to 6.25%. The (2x2x2) bulk supercells of the K-doped RuO_2 system remain stable under certain temperatures (T < 700 K). In the same supercell size, the stability of Ca-, Zn-, and Cu-doped RuO_2 systems are correspondingly increased. Similar to (3x3x3) supercells, as shown in Figure 4.8 (c), Cu, K, Zn, and Ca-doped RuO_2 systems are all stable up to 900 K. From Figure 4.8 (a)-(c), the ranking of the negative $\Delta G_{form,metal}$ values is basically ordered as Ag < Cu < K < Zn < Ca. There is only one exception – the bulk formation energy of (1x1x1) K-doped RuO_2 supercell exhibits the most positive value. Hence, regardless of the temperature influence, our results demonstrate that the stability of these five doped RuO_2 cells is ordered as Ag < Cu < K < Zn < Ca. Once the concentration of the dopant K atoms exceeds a certain value, the K-doped RuO_2 surface will become very unstable.

The plot of Figure 4.8 (d) also shows that the bulk formation energies for each M-doped RuO_2 surface become more negative from (1x1x1) to (2x2x2) to (3x3x3) bulk cells. Lines with three different styles in the same color are utilized to show the three supercells of each metal. Specifically, the dashed-dotted line, the dashed line, and the solid line indicates (1x1x1), (2x2x2) and (3x3x3) supercells of each doped system, respectively. From Figure 4.8 (d), we can realize that the stable doped structures are favorably formed at lower concentration, i.e. the stability of the (3x3x3) bulk cell is higher than (1x1x1) or (2x2x2) doped RuO_2 bulk cells. We then separately compared the $\Delta G_{form,metal}$ values of each M-doped system at different concentrations. If the three sets of $\Delta G_{form,metal}$ in one M-doped system are represented by the greater distance between

the corresponding three lines, it indicates that this doped system is very sensitive to the doping concentration, and vice versa. Thus, Figure 4.8 (d) shows that the stability of K, Ca and Ag-doped ruthenium oxide system may strongly depend on the doping concentration, especially for the K-doped system. In contrast, for the Cu- and Zn-doped RuO_2 supercells, the $\Delta G_{form,metal}$ values of (2x2x2) supercell are almost the same as that of (3x3x3) supercell, and very close to (1x1x1) supercell, indicating that the dopant concentration has little effect on Cu and Zn-doped RuO_2 systems among the above five dopants. This suggests Cu and Zn-doped RuO_2 systems as particularly stable and robust. Furthermore, although the stability of the Ca-doped system can be significantly influenced by concentration, its bulk formation energy value is always at a minimum level, no matter how the concentration changes. It is beneficial for the catalyst design to keep the stability with different doping concentrations; therefore, calcium cannot be excluded.

In addition, the obtained data also show that the stability of doped structures is reduced along with the increase of temperature. The general experimental temperature for Deacon process over the RuO_2(110) surface is around 600 K to 700 K.[4] Deactivation of the RuO_2 catalyst may occur due to RuO_2 sintering,[106] or the formation of volatile RuO_4 at very high temperature (> 673 K).[107] Considering these side reactions, the bulk formation energies of M-doped RuO_2 should still be negative at the general Deacon reaction temperature (around 600 K to 700 K). Figure 4.8 shows us that, even at the lowest concentration or at the room temperature, the $\Delta G_{form,metal}$ value of Ag-doped RuO_2 system is positive, indicating that Ag is unsuitable as a dopant, owing to its poor stability at the RuO_2 surface. The $\Delta G_{form,metal}$ calculated for Cu just straddles the zero line at 700 K, shown in Figure 4.8 (a). So for Cu doping, it is stable when the reaction happens below 700 K. With decreasing doping concentration, the Cu-doping system maintains stable up to increasingly higher temperatures. For instance, $\Delta G_{form,metal}$ is still negative at 800 K in the (3x3x3) bulk supercell, which indicates that the Cu doping is sensitive to the change of reaction temperature but still remains stable at the general Deacon reaction temperature, even as high as 800 K.

We notice that, in the definition of $\Delta G_{form,metal}$ in Equation 4.3, configurational entropic contributions are neglected. At realistic doping concentrations, configurational entropic contributions could additionally stabilize the doped state. However, systematic test calculations describing the bulk doping in (2x2x2) supercells indicate

that the energetics captured in Equation 4.3 represents already those of diluted dopants quite faithfully – even though the nominal dopant concentration in the employed (3x3x3) bulk supercells corresponds to 1,85%. For all of the five dopants, the formation energies calculated on the basis of the (2x2x2) supercell energetics are higher (< 0.2 eV for Cu, Zn, Ag, Ca; 0.7 eV for K) than those reported in Figure 4.8 (c) on the basis of the (3x3x3) supercell energetics. This reflects overall repulsive dopant-dopant interactions at corresponding distances. This trend continues when using very small (1x1x1) bulk supercells, which thus also excludes an agglomeration tendency of the dopants inside RuO_2 bulk.

We can conclude that, except Ag, all the above metals are thermodynamically favorable in the low doping concentration and under a wide range of temperatures (even higher than 800 K). In addition, no matter how the doping concentration changes, the bulk formation energies of Cu-, Zn- and Ca-doped RuO_2 supercells are always negative, indicating that their stability are always preferred. For potassium as a dopant, it has excellent stability in low concentrations, but it becomes extremely unstable at high doping concentrations. Therefore, we can exclude Ag and K as dopant to the RuO_2(110) surface. Considering the consistent stability, Cu, Zn and Ca are the most preferred dopants, especially in the low doping concentrations.
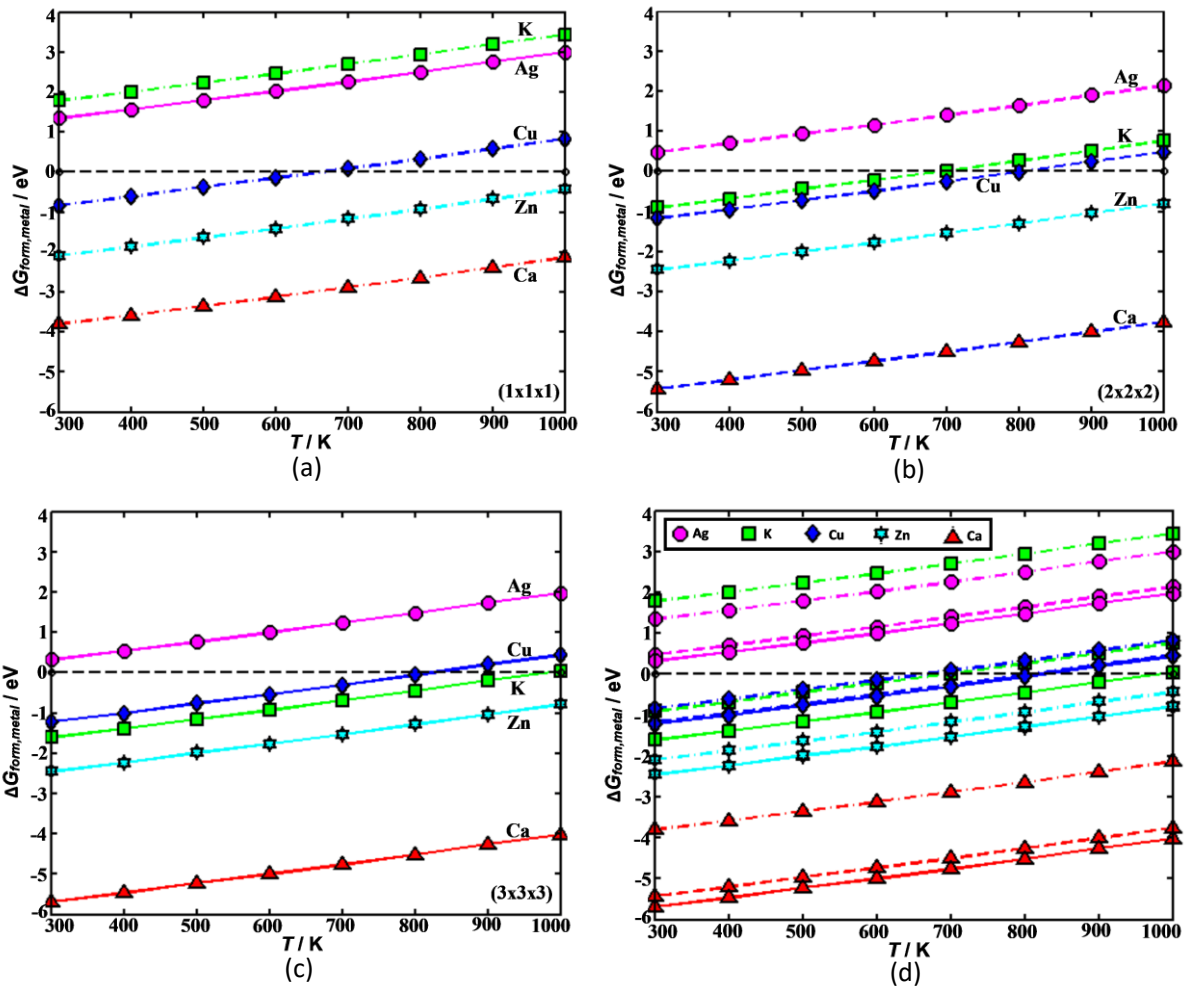
Figure 4.8 (Color online) Formation energies $\Delta G_{form,metal}$, eq. 4.3, at standard oxygen pressure and in the temperature range 300-1000 K. For the considered five dopants, four (Cu, Zn, Ca and K) exhibit negative formation energies up to temperatures relevant for the Deacon process, indicating a thermodynamic stability of these substitutional dopants against precipitation into their bulk metal phase. (a), (b) and (c) panel represents the different bulk supercell sizes. (a) (1x1x1); (b) (2x2x2); (c) (3x3x3); (d) represents the different three bulk supercells in the same panel. In (d), the dashed-dotted line, the dashed line, and the solid line indicates (1x1x1), (2x2x2), and (3x3x3) supercells, respectively.

4.3.4 Depth screening: stability considerations II

In part 4.3.2, the stability of the five mentioned doped surfaces with different concentrations and temperatures was evaluated through comparison of $\Delta G_{form,metal}$ values. In the next stage, we will investigate the stability of dopants at finite oxygen pressures, as this is how the Deacon reaction is always performed. We need to consider that, in the same operational condition, the dopant metal prefers to dissolve into the RuO_2 surface rather than be oxidized by O_2. Here, another similar sign is introduced and shown in Equation 4.4 to judge this preference. In order to ensure the accuracy of the calculated total energies, we first calculated the heats of formation for the bulk metal oxides in the low-temperature limit. We mainly compared the heats of formation, ΔE_f, of the main form oxides of Cu, Zn, Ag, Ca, K and Ru. Compared with the experimental data in Figure 4.9 (the details are shown in Table 4.8), our calculated values and referred values of DFT-GGA are in good agreement, even if there is a certain degree of difference between the calculated heats of formation, $\Delta E_{f(cal.)}$, and the low-temperature limit of the experimental heats of formation, $\Delta E_{f(cal.)}$[108]. The reason for the difference may come from the neglect of the zero-point vibrations, the entropy contributions, and systematic errors of the DFT approach.[92]

Table 4.8 Calculated DFT-GGA and literature bulk properties of metal oxide, M_xO_y. The lattice constant a_0, b_0, c_0, the nearest distance between metal atoms d_{M-M} and oxygen atoms d_{O-O}, as well as the M-O bond length d_{M-O} are listed in units of Å. Here, except for the reference values for K_2O (LDA), KO_2 (LDA), CuO (PW91), all computational results were done at the PBE level.

		a_0, b_0, c_0		d_{M-M}	d_{M-O}	d_{O-O}
CaO	Exp.[a]	4.81		3.40	3.40	2.41
	Cal.(Ref.)[b]	4.81				2.40
	Cal.(present)	4.83		3.42	3.42	2.42
ZnO	Exp.[a]	a_0 3.25	c_0 5.21	3.21	3.21	1.99
	Cal.(Ref.)[c]	a_0 3.29	c_0 5.30			
	Cal.(present)	a_0 3.28	c_0 5.29	3.26	3.26	2.01
Ag_2O	Exp.[a]	4.72		3.34	4.09	2.04
	Cal.(Ref.)[d]	4.91		3.47	4.25	2.13
	Cal.(present)	4.85		3.43	4.20	2.10
K_2O	Exp.[a]	6.44		3.22	4.55	2.79
	Cal.(Ref.)[e]	6.33			4.47	2.74
	Cal.(present)	6.40		3.20	4.52	2.77
KO_2	Exp.[f]	a_0 4.03	c_0 6.70	4.40	1.34	2.68
	Cal.(Ref.)[e]	a_0 3.90	c_0 6.80		1.36	2.72
	Cal.(present)	a_0 3.93	c_0 6.61	4.32	1.35	2.63
CuO	Exp.[g]	a_0 4.68 b_0 3.42 c_0 5.13 β=99.6°		2.88	2.62	1.95
	Cal.(Ref.)[h]	a_0 4.76 b_0 3.42 c_0 5.17 β=99.6°				
	Cal.(present)	a_0 4.73 b_0 3.42 c_0 5.15 β=99.6°		2.90	2.65	1.98
Cu_2O	Exp.[a]	4.27		3.02	3.68	1.84
	Cal.(Ref.)[i]	4.32		3.05	3.74	1.87
	Cal.(present)	4.27		3.04	3.73	1.86
RuO_2	Exp.[a]	a_0 4.52	c_0 3.12	3.55	2.48	1.95
	Cal.(Ref.)[j]	a_0 4.65	c_0 3.23			
	Cal.(present)	a_0 4.52	c_0 3.12	3.55	2.48	1.95

[a] References 93,94.   [b] Reference 109.   [c] Reference 110.   [d] Reference 88.   [e] Reference 111.
[f] Reference 112.   [g] Reference 113.   [h] Reference 114.   [i] Reference 104.   [j] Reference 115.

Table 4.9 Calculated and experimental heats of formation of M_xO_y (M_xO_y = CaO, K_2O, ZnO, RuO_2, KO_2, Cu_2O, CuO and Ag_2O) bulk oxides. The calculated values in this work and that from references are all obtained with DFT-GGA functional.

M_xO_y	CaO	K_2O	ZnO	RuO_2	KO_2	Cu_2O	CuO	Ag_2O
ΔE_f(exp.)[a] /eV	-6.58	-3.75	-3.61	-3.19	-2.93	-1.75	-1.62	-0.32
ΔE_f(cal.)Ref /eV	-5.85[b]	-3.03[b]	-2.82[c]	-3.35[d]	-2.60[b]	-1.24[e]	-1.09[e]	-0.18[f]
ΔE_f(exp.)present /eV	-5.98	-3.27	-2.91	-3.28	-2.53	-1.18	-1.22	-0.18

[a] *Reference 108.*　　　　[b] *Reference 116.*　　　　[c] *Reference 110.*
[d] *Reference 90.*　　　　[e] *Reference 117.*　　　　[f] *References 92.*

We refined the Equation 4.4 for approximating the stability conditions by adding $\Delta\mu_{O2(T,p)}$ to include the entropic conditions. It is already known that the temperature used in the Deacon process over RuO_2 catalysts is generally around 573 K to 673 K, rarely higher than 700 K. So here we mainly compared the descriptor of thermochemistry stability, $\Delta G_{form,oxide}$, of the main oxides of Cu, Zn, Ag, Ca, K at T = 600 K and 700 K. According to the definition of Equation 4.4, a more negative value of $\Delta G_{form,oxide}$ is favorable to be dissolved as the dopant into the RuO_2(110) surface, while a more positive value indicates a preference to form the oxide. All the calculated $\Delta G_{form,oxide}$ values for various metal oxides at T = 600 K and T = 700 K are listed in Table 4.9.

In order to better evaluate the temperature effect on thermochemical stability, we calculated $\Delta G_{form,oxide}$ values of the main oxides of the above five metals from 300 K to 1000 K. Not surprisingly, the stability situation with respect to phase separation of the substitutional dopants into a bulk oxide phase is much less favorable in the O-rich reaction conditions of the Deacon process. As summarized in Figure 4.10, only Cu exhibits negative formation energies $\Delta G_{form,oxide}$ in the relevant temperatures which range from 600 K to 700 K. Lower temperatures instead bring smaller $\Delta G_{form,oxide}$ values and it is then more favorable to dissolve the dopant over the catalytic surface. Furthermore, from Figure 4.10 we can realize that the $\Delta G_{form,oxide}$ values of Ag_2O, ZnO,

CaO, and K_2O remain positive (except K_2O at low temperature), while only the $\Delta G_{form,oxide}$ values of copper oxides are negative, even when the temperature is as high as 800 K. We hereby focus on calculating $\Delta G_{form,oxide}$ for both CuO and Cu_2O. Due to the different bulk oxide stoichiometries, the slopes of their $\Delta G_{form,oxide}$ lines (CuO and Cu_2O) in Figure 4.10 are different. Compared with CuO, Cu_2O exhibits a steeper increase towards positive formation energies at higher temperatures. At the lower O chemical potentials at these temperatures, decomposition into Cu oxide phases with lower O to metal stoichiometry than RuO_2 is simply less and less favorable. Despite the steeper increase of $\Delta G_{form,oxide}$ for Cu_2O along with temperature, it nevertheless remains negative in the targeted temperature range from 600 K to 700 K for the Deacon process. Here, the above-mentioned additional slight stabilization also applies due to the neglected entropy of the doped state. Our calculated results suggest that, among the above-mentioned five candidates, Cu is the most stable metal dopant that can be dissolved into the $RuO_2(110)$ surface rather than be oxidized in rich oxygen condition. Taking the above into consideration, we conclude that Cu is the most promising dopant with the best stability to be dissolved over the $RuO_2(110)$ surface in the Deacon process.

Table 4.10 Calculated $\Delta G_{form,oxide}$ values of M_xO_y (M_xO_y = CaO, K_2O, ZnO, RuO_2, KO_2, Cu_2O, CuO and Ag_2O) bulk oxides. The calculated values in this work are all obtained with the DFT-GGA functional PBE.

| M_xO_y		Ag_2O	K_2O	CuO	Cu_2O	ZnO	CaO
$\Delta G_{form,oxide}$ / eV	(T = 700 K)	0.96	0.58	-0.11	-0.03	0.65	0.48
$\Delta G_{form,oxide}$ / eV	(T = 600 K)	0.78	0.40	-0.23	-0.21	0.53	0.36
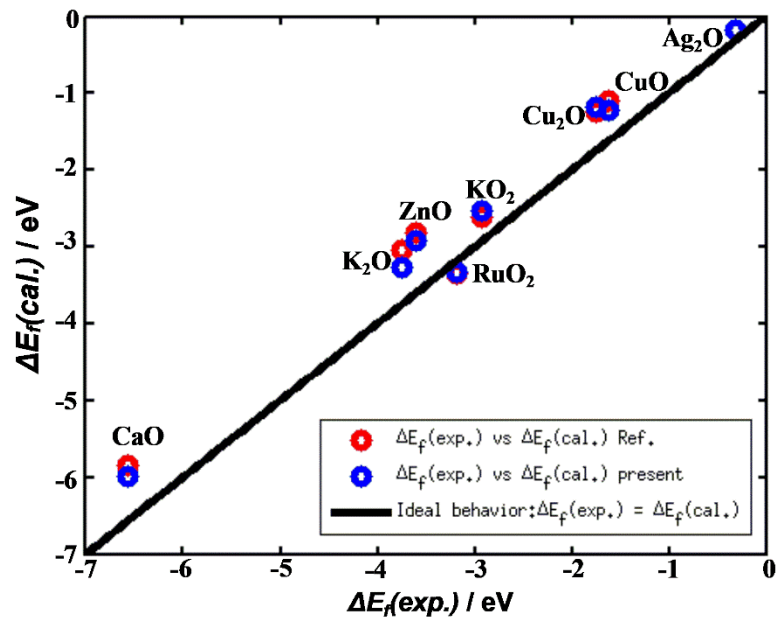
Figure 4.9 (Color online) The calculated heats of formation of metal oxides as a function of the experimental values obtained from reference. All calculated values are obtained using the DFT-GGA PBE functional.
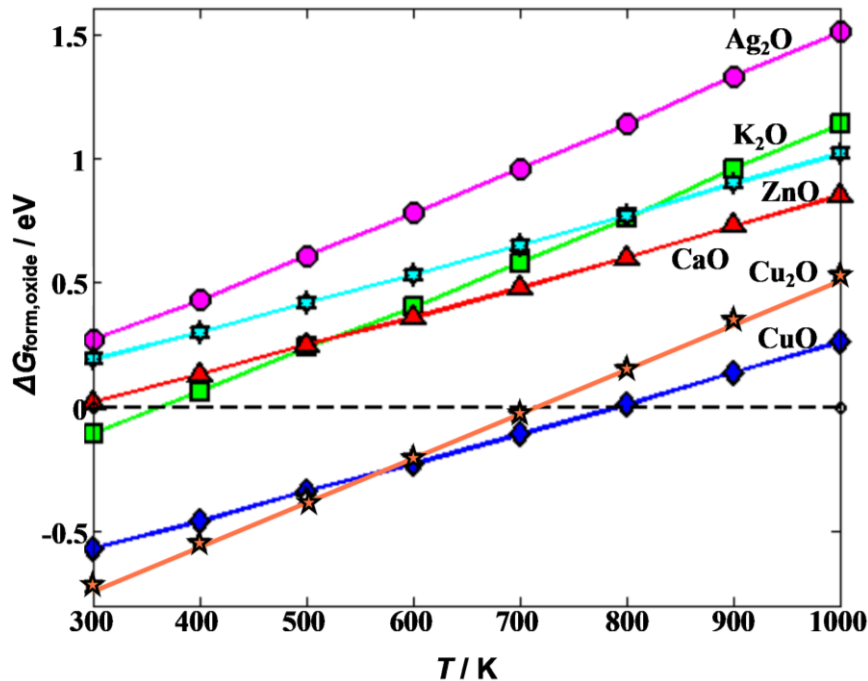

Figure 4.10 Formation energies $\Delta G_{form,oxide}$, eq. 4.4, at standard oxygen pressure and in the temperature range 300-1000 K. For the considered five dopants, only Cu exhibits a negative formation energy at the Deacon process temperatures, indicating a thermodynamic stability of this substitutional dopant against precipitation into the considered bulk oxide phases.

In conclusion, the primary screening approach with our two-dimensional descriptor based on kinetics suggests that Cu, Ag, Zn, K, and Ca exhibit a promising behavior, weakening the Cl adsorption, while showing significant preference to segregate to the surface. We also applied the combination of thermodynamics and DFT to derive a simple thermodynamic stability condition in order to evaluate the stability of the dopant in different doping concentrations and temperatures. Specifically, we carried out studies to judge whether the metal dopant is favorable to be dissolved into the $RuO_2(110)$ surface or be oxidized in rich oxygen condition. The bulk formation free energy demonstrates that Ag-doped $RuO_2(110)$ surface is unfavorable because of the endothermic formation energy, and K-doped $RuO_2(110)$ surface is greatly influenced by the doping concentration. Another thermochemistry stability term ($\Delta G_{form,oxide}$) confirmed that Cu is the most stable dopant dissolved into the $RuO_2(110)$ surface rather than be oxidized by itself under the oxygen-rich conditions. We therefore conclude that Cu is preferred as the most promising dopant over RuO_2 (110) surface as the Deacon catalyst on the basis of kinetics and thermodynamics studies.

However, the stability of the catalytic surface seems to be very sensitive to the temperature according to the $\Delta G_{form,metal}$ and $\Delta G_{form,oxide}$ calculations, and including Cu doping. Therefore, it would be a big challenge to control and keep the stability of the catalyst at very high temperature (> 800 K). The $RuO_2(110)$ surface is then easily chlorinated in the Deacon process to form the relatively stable $RuO_{2-x}Cl_x(110)$, which is self-limiting and suppresses the HCl oxidation.[3,4] Here, we hope that the Cu doping may break the stability of the $RuO_{2-x}Cl_x(110)$ structure, since Cu is more favorable to be chlorinated than Ru. The reason is that the thermodynamical formation energy of copper chloride is more negative than ruthenium chloride. At the same time, this does not rule out the formation of a very small amount of CuO, especially at high temperature (> 673 K) or long-term reaction. Therefore, the Cu-doped $RuO_2(110)$ surface could possibly consist of the binary catalyst system $CuO/CuCl_2$, which can accelerate the release of Cl_2 products[118,119], rather than to form the $RuCl_{2-x}O_x$ structure to suppress the Deacon process. In conclusion, doping Cu into the Deacon catalyst can change the state of chlorination on the $RuO_2(110)$ surface, and perhaps bring a new inspiration to the design of novel Deacon catalyst.

4.4 Conclusion

We performed a DFT-based computational screening study that evaluated the suitability of 22 metal dopant atoms to improve the Deacon process over RuO_2 catalysts. All of the considered dopants lead to the desired weakening of the binding of central reaction intermediates, and specifically of adsorbed chlorine. In particular, Cu, Zn, Ag, Ca and K appear as the promising dopant in this respect, and induce stronger reductions of the Cl desorption energy that was used as a reactivity descriptor. Meeting stability requirements turn out to be much harder to achieve. In the oxygen-rich conditions of the high-temperature Deacon process particularly the precipitation of metal dopants to form separate bulk oxide phases of their own is critical. From the five promising metals, only Cu doping shows a corresponding stability on the basis of the calculated stability descriptor. This reveals the added value and necessity to conduct multi-descriptor screening studies that consider both reactivity and stability aspects of a catalytic process like Deacon. Other oxidation reactions like room temperature OER at RuO_2 electrodes might not pose such critical stability constraints. This could rationalize why for example Zn doping, which in our study is clearly unstable against oxide precipitation, was reported to favorably affect OER and chlorine evolution.[74,78,79]

A final intriguing result of our study is the quite local effect of the dopants on the surface binding. Instead of more global effects like shifting the Fermi level in semiconducting materials, the metallic screening in RuO_2 seems to restrict a significant influence of the dopant to its immediate coordination sphere. Thus effectively representing new types of active sites at the surface, doping RuO_2 could thus mechanistically be seen as opening up a possible bifunctional behavior between the different sites. However, in view of the recently identified generic restrictions to such bifunctionality[120,121], detailed microkinetic modeling at the kinetic Monte Carlo level[122] (explicitly accounting for the spatial distributions and the strong diffusion limitations at RuO_2) would be required to validate this notion. While we plan to conduct such simulations in the future, smaller RuO_2 nanoparticles could generally be of higher interest for doping. Not least due to the band gap opening, such nanoparticles could allow for longer-ranged doping effects than metallic RuO_2.

Chapter 5

A first-principles study for the Deacon Process over Cu-doped RuO₂(110)

5.1 Introduction

The Deacon process is currently the best strategy for converting waste HCl to high purity Cl_2, and with the only by-product being water, it is regarded as sustainable and "green". In recent years, the Deacon catalyst has been developed from the original $CuO/CuCl_2$ to the recent RuO_2-based catalyst, which has been identified as the best Deacon catalyst owing to its correspondingly higher catalytic activity and thermodynamic stability.[34,63,123] An important approach towards the industrial production of chlorine was made by Sumitomo Chemicals using RuO_2 catalyst coated on rutile TiO_2.[17,26] However, the calculations performed by I. C. Man et al. proved that the catalytic activity of a single RuO_2 catalyst may not be improved in that its oxygen dissociation energy already reaches the optimum.[38,76] Taking this aspect into account, we supposed that incorporation of RuO_2 catalyst with a small amount of non-precious additives or dopants on its surface would directly modify the structure of metal oxide and change its physicochemical properties. The catalytic activity and stability of RuO_2-based Deacon catalyst would be further improved if an appropriate doping process is achieved.[124]

In the last chapter, we have investigated 22 metals to be doped into the RuO_2(110) surface and compared both the reactivity and stability of the doped system. On the basis of the computational multi-descriptor screening we finally concluded on Cu to be the best dopant. Our calculations also confirmed that the Cu dopant atom located on the cus site shows higher activity and keeps basically the same stability than that at the br site. This intriguing result of doping RuO_2 could mechanistically be seen as

opening up a possible bifunctional behavior between the different sites, thus effectively representing new types of active sites at the Deacon catalyst surface.

In order to validate our notion about doping, a detailed microkinetic modeling for the Deacon process is required. As detailed in Chapter 3, the reaction mechanism on undoped RuO_2(110) was found in several works to fit a Langmuir-Hinshelwood - Hougen-Watson (LHHW) kinetic model with the recombination of the top-chlorine atoms together with O_2 dissociation as the rate-determining step. Our target in this chapter is to assess how this rate-determining step is affected by Cu doping. We employ first-principles calculations to determine the energy barriers of each elementary step. Moreover, by explicitly comparing the energy barriers on the pure RuO_2(110) surface to the those on the Cu-doped RuO_2(110) surface, we gain detailed insights into the Deacon reaction mechanism and theoretically investigate whether the catalytic activity of the Deacon catalyst is improved through the doping strategy.

5.2 Methodology

By calculating the rates of individual elementary steps in a catalytic cycle, DFT is widely used for material-specific modeling of chemical reactions at extended surfaces.[125,126] Estimating the potential energy surface (PES) allows identification of intermediary states, reactants, and products of the catalytic reaction which appear as local minima on the PES. The rate of getting from one configuration of atoms to another is calculated using transition state theory (TST) approximations.[64,65,125,127] Realizing the possible states and their rates offers a powerful description of the reaction network.

The ingredients of the modeling are the surface adsorption sites, namely the "active sites". The list of all elementary processes involve these sites as well as their corresponding rate constants. To provide predictive quality to our modeling, all rate constants are determined through first-principles density-functional theory (DFT). In the following section, we detail the lattice model and list of elementary reactions for the Deacon process at Cu-doped RuO_2(110), and then explain the working equations and computational details to determine the first-principles rate constants.

5.2.1 Reaction model

From both experimental and theoretical points of view, extensive previous work points at a prominent role of two undercoordinated sites at the pure RuO_2(110) surface.[65,66, 128,129] Figure 5.1 illustrates these two sites, denoted as "cus" and "br", as well as their trench-like arrangement at the RuO_2(110) surface. Here, we doped one Cu atom to replace one of the original Ru atoms at the cus site on the top layer (Figure 5.1, left). Due to the replacement of the doped Cu atoms, the effect of each br and cus active site on the chemical reaction is changed, and the original two active sites (br and cus) turn to four different active sites (br_1, br_2, Ru_{cus}, and Cu_{cus}), as shown in Figure 5.1 right. In this, we assume that the effect of doping is short-ranged, cf. Chapter 4, and that it only affects the reaction energetics at directly neighboring active sites.

Since only a small amount of Cu atoms are doped into the original RuO_2(110) surface, we can assume a diluted distribution of the changed four active sites (br_1, br_2, Ru_{cus}, and Cu_{cus}). As also noted in Chapter 4, the dopant concentration is one of the major factors which influence the reactivity. Here, we focus on the modified surface and mainly calculate the activation energy of each step based on the same mechanism as before, and then compared with the values of the energy barrier between pure and Cu-doped RuO_2 (110) surface.

To describe the kinetics of HCl oxidation, we consider all non-concerted elementary adsorption, desorption, reaction and diffusion steps involving these four sites. Specifically, these are the dissociative adsorption of reactants (HCl, O_2), which in the case of HCl occurs only through the formation of a surface hydroxyl group.[4] HCl or OH dissociation involving the formation of a H_{cus} species is not possible, as atomic hydrogen does not bind to an empty cus site.[130] In view of a calculated negligible Cl_2 binding energy to both br and cus sites, chlorine formation is modeled as associative desorption event. In contrast, disproportionation of adjacent hydroxyl groups leads first to the formation of molecularly adsorbed water as a stable reaction intermediate, which eventually desorbs as a product. Diffusion of all surface species (O, H, OH, Cl and H_2O) proceeds along and across the br and cus rows of the Cu-doped RuO_2(110) surface. Finally, this leads to the list of 68 elementary processes between br and cus sites summarized in Table 5.1. Here, considering that the original br and cus sites turn to

four different active sites due to the addition of doped Cu atoms, there is more than one expression for some certain elementary steps, and the corresponding potential energy would be also different.
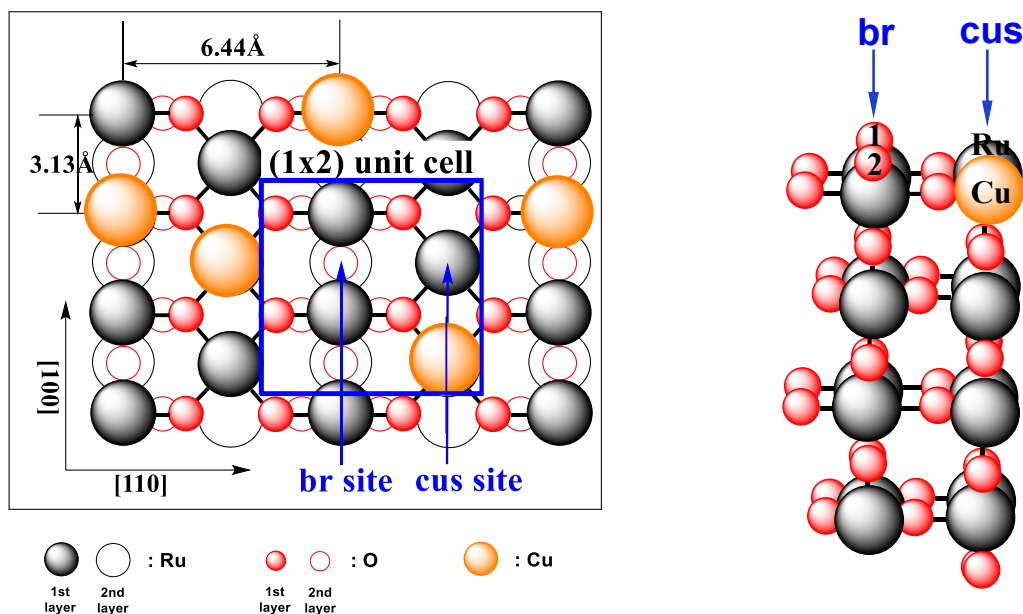

Figure 5.1 *Left*: Top view of the Cu-doped RuO_2 catalyst surface illustrating the (1x2) unit cell containing two br and cus sites. Orange yellow, large spheres: Cu (at first layer); Dark gray, large spheres: Ru (solid - at first layer; hollow - at second layer); red, small spheres: O (solid - at first layer; hollow - at second layer). *Right*: Side view of the RuO_2(110) surface model with four layers and one Cu atom exchanging one of the Ru atoms at the cus site on the top layer. Four top active sites are included: br_1, br_2, Ru_{cus}, and Cu_{cus}.

5.2.2 First-principles rate constants

As also introduced in Chapter 3, the first-principles rate constants for every elementary process are calculated following the approach by Reuter and Scheffler,[65] which relies on kinetic gas theory and detailed balance for adsorption and desorption processes, as well as harmonic TST for diffusion processes. For non-activated adsorption processes, a sticking coefficient of unity is assumed. The further required binding energies and energy barriers are obtained from density-functional theory (DFT) calculations as implemented in the plane-wave code CASTEP[68] and using library ultrasoft

pseudopotentials. The revised generalized gradient approximation (GGA) functional by Perdew, Becke, and Ernzerhof (RPBE)[48] is employed to treat electronic exchange and correlation effects. The periodic boundary condition calculations are performed using a supercell containing a slab consisting of four O_2-RuO_2-O_2 trilayers and a (1x2) surface unit cell. A vacuum region of about 30 Å ensures the decoupling of the periodic slab images. Adsorption is on one side of the slab, and the atomic positions of the two topmost trilayers are allowed to fully relax until residual forces fall below 50 meV/Å. Convergence tests for the binding energies demonstrate a numerical convergence within 50 meV at the employed energy cut-off of 450 eV and a Brillouin zone (BZ) integration with a (6x6x1) Monkhorst-Pack grid with 18 k-points. The energy barriers are determined using the nudged-elastic band (NEB)[131] and the linear and quadratic synchronous transit (LST/QST)[60] methods.

Table 5.1 summarizes the DFT binding energies (E_b) of all stable surface species at 1/2 monolayer (ML) coverage at a (1x2) stoichiometric Cu-doped RuO_2(110) slab, which are also compared with pure and modified RuO_2(110). The binding energies at the pure RuO_2(110) surface are in very good agreement with existing literature values, except one value with respect to H_2O binding energy (H_2O_{cus}) reported by Hess et al.[37] The calculated H_2O_{br} binding energy is fully consistent with the value obtained by Sun et al.[128] using a full-potential DFT approach. Furthermore, the large binding energy of water reported by Hess et al.[37] is completely inconsistent with the experimentally found desorption temperature of water from this surface at around and above 400 K.[63,70] When Cu atoms are doped into RuO_2(110) surface, the binding energies (E_b) of most surface species become less negative, except the E_b of H@O. In particular, the E_b of H_2O exhibits the biggest change. This shows that the modified RuO_2(110) surface has a stronger binding to OH species, while the binding force toward water molecules is greatly weakened, which is more conducive to the removal of water molecules from the surface into the gas phase, thus accelerating the formation of the product water. For the O and Cl species, the binding forces on the doped surface are reduced; however, compared to the cus site, the br site of the surface still shows a stronger binding force.

Table 5.1 DFT binding energies (E_b) of different surface species involved in HCl oxidation. Shown are values for adsorption on br and cus sites and at 1/2 monolayer (ML) coverage at a (1x2) stoichiometric RuO_2(110) slab where the br sites depicted in Figure 5.1 are all occupied by O. Hydrogen is adsorbed on top of oxygen at either br or cus site, denoted as $H@O_{br}$ and $H@O_{cus}$, respectively. In our model, attractive (binding) interactions are defined as negative, while repulsive interactions are defined as positive. Note: br_1 site means the bridge site neighbors to the Ru_{cus} site, and br_2 site means the bridge site neighbors to the Cu_{cus} site.

Surface Species	E_b (eV)			
	Cu-doped RuO$_2$(110)		Pure RuO$_2$(110)	
	O$_{rich}$	O$_{poor}$	Ours	Ref.
O$_{cus}$	-0.7(Ru$_{cus}$), 1.6(Cu$_{cus}$)	-1.1(Ru$_{cus}$), 1.4(Cu$_{cus}$)	-1.1	-1.1[65], -0.8[71], -1.5[29]
O$_{br}$	-1.3(br$_1$), -1.6(br$_2$)	-1.3(br$_1$), -1.6(br$_2$)	-2.3	-2.3[65], -2.2[71], -2.5[29]
H@O$_{cus}$	-3.0(Ru$_{cus}$), -2.2(Cu$_{cus}$)	-3.3(Ru$_{cus}$), -2.4(Cu$_{cus}$)	-1.3	-2.6[29]
H@O$_{br}$	-2.5(Ru$_{cus}$), -2.3(Cu$_{cus}$)	-2.5(Ru$_{cus}$), -2.3(Cu$_{cus}$)	-1.0	-0.9[132], -3.2[29]
Cl$_{cus}$	-1.2(Ru$_{cus}$), -0.6(Cu$_{cus}$)	-1.2(Ru$_{cus}$), -0.6(Cu$_{cus}$)	-1.4	-1.6[35], -1.8[29]
Cl$_{br}$	-1.5(br$_1$), -1.8(br$_2$)	-1.5(br$_1$), -1.7(br$_2$)	-2.2	-2.3[37], -2.4[29]
H$_2$O$_{cus}$	-0.4(Ru$_{cus}$), -0.1(Cu$_{cus}$)	-0.2(Ru$_{cus}$), 0.0(Cu$_{cus}$)	-1.1	-4.2[37], -3.0[29]
H$_2$O$_{br}$	-0.1(br$_1$), -0.4(br$_2$)	-0.1(br$_1$), -0.4(br$_2$)	-1.0	-1.0[130], -4.2[37], -2.9[29]

Table 5.2 compiles the resulting forward and backward energy barriers for the individual elementary processes (including adsorption, desorption, diffusion and recombination processes). The differences of the energy barrier for each step of the Deacon reaction between pure RuO_2(110) and Cu-doped RuO_2(110) surfaces are described in detail below, and Figures 5.4-5.6 are plotted for specific comparative analysis. The DFT values for the forward and backward reactions have been carefully checked and in parts slightly adjusted (within 0.1 eV), so that the microkinetic model fulfills the thermodynamic constraints

$$\Delta E_{forw}(i) = \Delta E_{backw}(i) - \Delta H(i) \qquad (5.1)$$

where ΔH(i) is the reaction enthalpy of elementary process *i* as approximated by the corresponding total energy difference (ΔE). Such adjustments are necessary, whenever gas-phase and surface properties are merged that are calculated under different approximations.[61] The recipe used was to fix the surface reaction properties through the adsorption/desorption processes, for which the forward and backward kinetic parameters are related to the change in the Gibbs free energy of the reaction. The corresponding Gibbs free energy is then used to check for the thermodynamic consistency of the diffusion processes of the surface intermediates.

Table 5.2 Elementary steps considered in the Deacon reaction with the DFT calculated activation barriers, ΔE_{forw} / ΔE_{backw}, for the forward and backward reactions, respectively. In the case of Cl involving reactions, the barriers shown correspond to configurations without nearby Cl species.

Process	ΔE_{forw} / ΔE_{backw}(eV)		
	Cu-doped RuO$_2$(110) (GGA-RPBE)	Pure RuO$_2$(110) (GGA-PBE)[133]	Ref.
Reactant adsorption/desorption:			
1 HCl + O$_{br}$ + *$_{cus}$ ↔ Cl$_{cus}$ + OH$_{br}$	0.0/1.5 (Cl_Ru$_{cus}$ - OH_br); 0.0/0.9 (Cl_Cu$_{cus}$ - OH_br)	0.0/1.5	0.0/1.0[4]
2 HCl + O$_{cus}$ + *$_{cus}$ ↔ Cl$_{cus}$ + OH$_{Rucus}$	0.0/0.4 (Cl_Cu$_{cus}$ - OH_Ru$_{cus}$); 0.0/2.4 (Cl_Ru$_{cus}$ - OH_Cu$_{cus}$)	0.0/1.8	0.0/-[4]
3 HCl + O$_{br}$ + *$_{br}$ ↔ Cl$_{br}$ + OH$_{br}$	0.0/1.7 (Cl_br$_1$ - OH_br$_2$); 0.0/2.1 (Cl_br$_2$ - OH_br$_1$)	0.0/2.3	
4 HCl + O$_{cus}$ + *$_{br}$ ↔ Cl$_{br}$ + OH$_{cus}$	0.0/1.8 (Cl_br - OH_Ru$_{cus}$); 0.0/3.3 (Cl_br - OH_Cu$_{cus}$)	0.0/2.6	
5 O$_2$ + *$_{cus}$ + *$_{cus}$ ↔ O$_{cus}$ + O$_{cus}$	0.0/1.2	0.0/2.0	0.2/2.1[72]; 0.0/2.0[67]
6 O$_2$ + *$_{br}$ + *$_{cus}$ ↔ O$_{br}$ + O$_{cus}$	0.0/2.5 (O_br - O_Ru$_{cus}$); 0.0/0.2 (O_br - O_Cu$_{cus}$)	0.0/3.3	0.0/3.3[67]
7 O$_2$ + *$_{br}$ + *$_{br}$ ↔ O$_{br}$ + O$_{br}$	0.0/3.2	0.0/4.6	0.0/4.6[67]
Product formation/desorption/re-adsorption:			
8 Cl$_{cus}$ + Cl$_{cus}$ ↔ Cl$_2$ + *$_{cus}$ + *$_{cus}$	1.4/0.0 (O$_{rich}$,Cl_cus + Cl_cus)	2.4/0.0	1.6/-[4]; 2.4/0.0[29]
9 Cl$_{br}$ + Cl$_{cus}$ ↔ Cl$_2$ + *$_{br}$ + *$_{cus}$	2.9/0.0 (Cl_br + Cl_Ru$_{cus}$); 2.2/0.0 (Cl_br + Cl_Cu$_{cus}$)	3.4/0.0	3.2/-[4]
10 Cl$_{br}$ + Cl$_{br}$ ↔ Cl$_2$ + *$_{br}$ + *$_{br}$	3.2/0.0 (Cl_br$_1$ - Cl_br$_2$)	4.2/0.0	
11 OH$_{cus}$ + OH$_{cus}$ ↔ O$_{cus}$ + H$_2$O$_{cus}$	0.2/0.2 (O_Ru$_{cus}$ + H$_2$O_Cu$_{cus}$) 2.3/0.2 (O_Cu$_{cus}$ + H$_2$O_Ru$_{cus}$)	0.3/0.3	0.6/-0.1[72]; 0.2/-[4]
12 OH$_{br}$ + OH$_{br}$ ↔ O$_{br}$ + H$_2$O$_{br}$	2.1/0.3 (O_br$_1$ H$_2$O_br$_2$) 3.5/0.5 (O_br$_2$ H$_2$O_br$_1$)	2.0/1.0	1.5/0.4[72]
13 OH$_{cus}$ + OH$_{br}$ ↔ O$_{cus}$ + H$_2$O$_{br}$	2.0/0.3 (O_Cu$_{cus}$ + H$_2$O_br); 2.5/0.3 (O_Ru$_{cus}$ + H$_2$O_br)	1.5/0.2	1.9/0.4[72]
14 OH$_{cus}$ + OH$_{br}$ ↔ O$_{br}$ + H$_2$O$_{cus}$	2.2/0.3 (H$_2$O_cus + O_br$_1$) 1.3/0.3 (H$_2$O_cus + O_br$_2$)	0.3/0.6	0.5/0.1[72]; 0.4/-[4]
15 H$_2$O$_{cus}$ ↔ H$_2$O + *$_{cus}$	0.4/0.0 (Ru$_{cus}$); 0.1/0.0 (Cu$_{cus}$)	1.1/0.0	0.9/-[4]; 1.1/0.0[29]
16 H$_2$O$_{br}$ ↔ H$_2$O + *$_{br}$	0.4/0.0 (br$_2$); 0.1/0.0 (br$_1$)	0.8/0.0	
Surface diffusion:			
17 Cl$_{cus}$ + *$_{br}$ ↔ *$_{cus}$ + Cl$_{br}$	0.7/1.2 (br-Ru$_{cus}$); 0.2/1.3 (br-Cu$_{cus}$)	0.6/1.4	0.6/1.2[72]
18 Cl$_{Cucus}$ + *$_{Rucus}$ ↔ *$_{Cucus}$ + Cl$_{Rucus}$	0.4/0.9	0.6/0.6	0.6/0.6[72]

Reaction			
19 $Cl_{br} + *_{br} \leftrightarrow *_{br} + Cl_{br}$	0.4/0.6	1.0/1.0	0.8/0.8[72]
20 $O_{cus} + *_{br} \leftrightarrow *_{cus} + O_{br}$	0.8/1.0	0.8/2.1	0.5/1.5[72]; 1.0/2.3[65]
21 $O_{cus} + *_{cus} \leftrightarrow *_{cus} + O_{cus}$	1.6/1.6	1.6/1.6	1.2/1.2[72]; 1.6/1.6[65]
22 $O_{1br} + *_{2br} \leftrightarrow *_{1br} + O_{2br}$	0.4/0.7	0.8/0.8	1.0/1.0[72]; 0.7/0.7[65]
23 $OH_{cus} + *_{br} \leftrightarrow *_{cus} + OH_{br}$	0.7/1.1 ($Ru_{cus} \rightarrow br_1$) 0.4/2.0 ($Cu_{cus} \rightarrow br_2$)	0.9/1.9	1.0/1.7[72]; 0.7/2.1[70]
24 $OH_{Cucus} + *_{Rucus} \leftrightarrow *_{Cucus} + OH_{Rucus}$	0.7/1.5	1.3/1.3	1.2/1.2[72]; 0.5/0.5[70]
25 $OH_{br} + *_{br} \leftrightarrow *_{br} + OH_{br}$	2.3/2.5	0.9/0.9	1.0/1.0[72]; 0.9/0.9[70]
26 $OH_{cus} + O_{br} \leftrightarrow O_{cus} + OH_{br}$	0.5/0.3	0.6/0.3	0.8/0.5[72]; 0.5/0.5[4]
27 $OH_{cus} + O_{cus} \leftrightarrow O_{cus} + OH_{cus}$	1.9/0.4 ($OH\_Cu_{cus}\,O\_Ru_{cus} \rightarrow$ $OH\_Ru_{cus}\,O\_Cu_{cus}$)	2.6/2.6	0.5/0.5[72]
28 $OH_{br} + O_{br} \leftrightarrow O_{br} + OH_{br}$	2.3/2.5	1.2/1.2	2.1/2.1[72]
29 $H_2O_{cus} + *_{br} \leftrightarrow *_{cus} + H_2O_{br}$	0.6/0.8 ($Cu_{cus} \rightarrow br$) 0.6/0.7 ($Ru_{cus} \rightarrow br$)	0.8 / 0.5	0.7/0.5[72]
30 $H_2O_{cus} + *_{cus} \leftrightarrow *_{cus} + H_2O_{cus}$	0.9/0.5 ($Ru_{cus} \rightarrow Cu_{cus}$)	0.7 / 0.7	1.2/1.2[72]
31 $H_2O_{2br} + *_{1br} \leftrightarrow *_{2br} + H_2O_{1br}$	0.4/0.1	0.8 / 0.8	1.0/1.0[72]
32 $H_2O_{cus} + OH_{br} \leftrightarrow OH_{cus} + H_2O_{br}$	1.1/0.5 ($H_2O\_cus + OH\_br_1$) 1.4/0.4 ($H_2O\_cus + OH\_br_2$)	1.6 / 0.3	1.5/0.7[72]
33 $H_2O_{cus} + OH_{cus} \leftrightarrow OH_{cus} + H_2O_{cus}$	0.3/0.8 ($H_2O\_Ru_{cus} + OH\_Cu_{cus}$)	0.3 / 0.3	1.5/0.7[72]
34 $H_2O_{br} + OH_{br} \leftrightarrow OH_{br} + H_2O_{br}$	0.4/0.4	0.4 / 0.4	0.3/0.3[72]

5.3 Results and discussion

5.3.1 Reaction mechanism of Deacon over Cu-doped RuO$_2$(110)

According to Chapter 3, the reaction mechanism of the Deacon process over the pure RuO$_2$(110) surface can be structured into five elementary steps,[4,15,38] which can be seen in Table 3.1. In our reaction model, we assume that the reaction mechanism of the Deacon process over Cu-doped RuO$_2$(110) surface can be also summarized into these five processes, as shown in Figure 5.2: (i) surface re-oxidation; (ii) hydrogen abstraction from hydrogen chloride; (iii) water formation; (iv) water desorption; (v) and chlorine recombination and desorption.
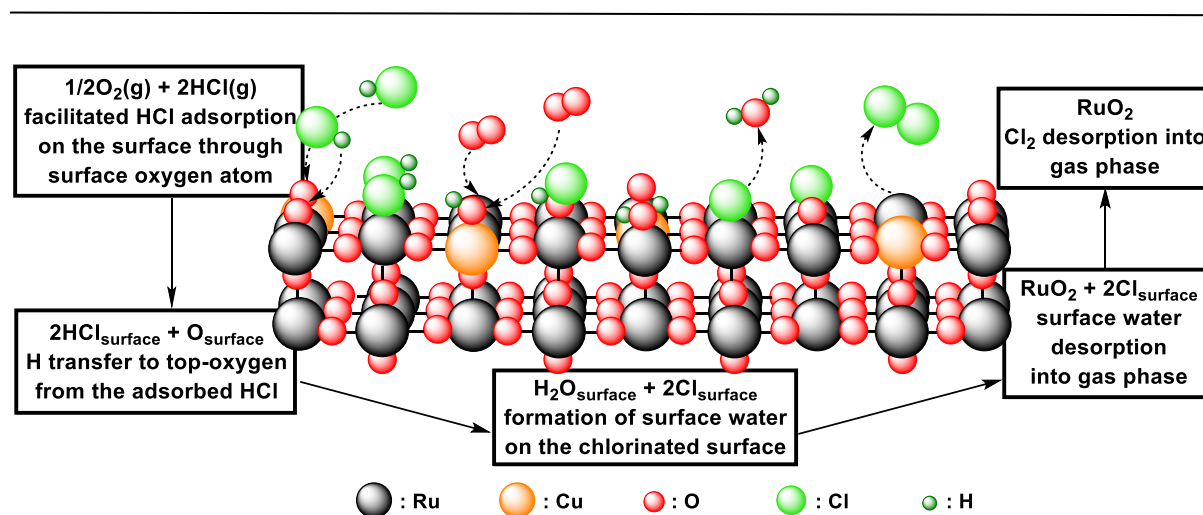

Figure 5.2 The mechanism of the Deacon process over the Cu-doped RuO$_2$(110) surface. Yellow, large spheres: Cu; dark gray, large spheres: Ru; red, small spheres: O; light green, large spheres: Cl; dark green, small spheres: H.

Recently, DFT calculations have been extensively used in the theoretical mechanistic study of HCl oxidation over RuO$_2$ based catalysts.[4,35,38] In our research work, the exploration about the mechanism of Deacon process over Cu-doped RuO$_2$(110) surface was performed using DFT calculations, which was also compared with the Deacon process over the pure RuO$_2$(110) surface. Here, the first adsorption process of O$_2$ and HCl onto the 1f-cus position was taken as an example to illustrate the reaction

mechanism of Deacon process over pure RuO_2(110) surface as well as over Cu-doped RuO_2(110) surface. The briefly summarized mechanisms were shown in Figure 5.3 (a) and (b), respectively, and the corresponding energy diagram along the reaction coordinate is depicted in Figure 5.4.
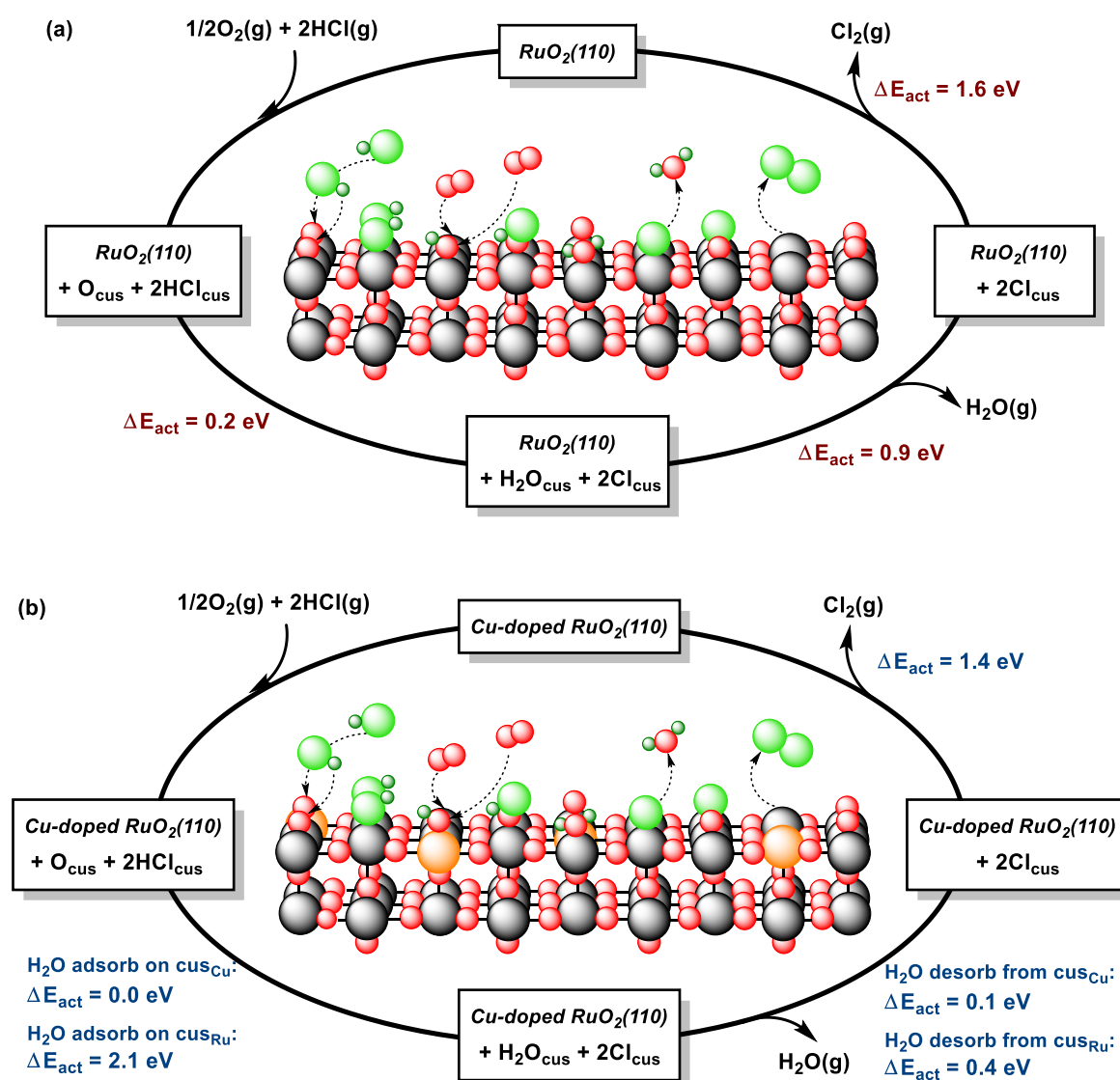

Figure 5.3 Catalytic cycle of the Deacon process (a) over the pure RuO_2(110) model catalyst[35] and (b) over Cu-doped RuO_2(110) model catalyst. The activation energies ΔE_{act} are determined by DFT calculations.

As described in Figure 5.3, both of the reactants O_2 and HCl are first adsorbed onto the 1f-cus Ru sites. O_2 dissociates to form adsorbed O, and then H abstracted from HCl leads to the adsorbed Cl_{cus} and $O_{cus}H$ species in terminal positions. Through H-transfer among the $O_{cus}H$ species, H_2O can be formed by the recombination with surface hydroxyl groups and be subsequently released from the surface around 400 K. Neighboring on-top Cl_{cus} atoms recombine to form Cl_2, which is immediately liberated into the gas phase. The Langmuir type kinetics of the Deacon process over RuO_2 (110) is shown to be governed by the adsorption energies of the reaction intermediates (water: 0.9 eV; and on-top Cl_{cus}: 1.6 eV against Cl_2). According to Figure 5.3 (a), the elementary process with the highest activation energy is identified with the association of two Cl_{cus} to generate Cl_2, which is in good agreement with previous work that regards the chlorine recombination process as the most energetically demanding step in the proposed Deacon scheme.[33,35,36,63]

However, the addition of copper significantly changes the reactivity of its adjacent sites. Accordingly, the adsorption energies of reaction intermediates in the Deacon process are different. It can be seen from Figure 5.3 (b) that chlorine recombination no longer represents the most energetically demanding step in the Deacon process, while the rate-determine step is greatly dependent on the cus site of the absorbed H_2O molecule formed by two $O_{cus}H$ species associated with H-transfer. When the formed water molecule locates at the Cu_{cus} site, the reaction cycle in Figure 5.3 (b) shows that the activation energy required for chlorine recombination is still the highest (water: 0.1 eV; and on-top Cl_{cus}: 1.4 eV against Cl_2). In contrast, when the water molecule formed locates at the Ru_{cus} site, the association of two $O_{cus}H$ species to generate a water molecule requires a relatively higher activation energy of 2.1 eV in comparison to the associative desorption of Cl_2 (1.4 eV). This observation is also consistent with the Hess and Over's conclusion that H_2O formation, rather than O_2 adsorption, determines the rate of Cl_2 production under certain reaction conditions.[72]

5.3.2 Comparison with the Deacon process over pure RuO$_2$(110)

Considering the activity difference between the br and cus site on RuO$_2$(110), we can classify the dissociation of O$_2$ into three different cases. Case-1: The O$_2$ molecule decomposes into two O species, and both of them are adsorbed on the br site; Case-2: The O$_2$ molecule decomposes into two O species, and both of them are adsorbed on the cus site; Case-3: The O$_2$ molecule dissociates to form two adsorbed O species. One of the oxygen atoms is adsorbed on the br site, and the other is on the cus site. In this work, we separately computed the activation energy of elementary processes in each case by DFT calculation, and compared it with the corresponding activation energy on pure RuO$_2$(110) surface. Three energy diagrams are thus plotted, which are shown in Figure 5.4-5.6 respectively.

As can be seen from Figure 5.4 (case-1), the dissociative adsorption of O$_2$ forms the atomic O at two neighboring br sites (O$_{br}$). The step is activated by an energy of 3.2 eV, which is higher than the data calculated by D. Teschner et al. (1.2 eV),[36] but lower than 4.6 eV calculated by F. Sotoodeh et al. (also see Table 5.2).[133] HCl molecules are dissociated with Cl sitting on-top of a 1f-cus Ru site (Ru$_{cus}$), and the H atom transfers to bridging O (O$_{br}$), forming a hydroxyl group. This process occurs without any obvious activation barrier and is exothermic by 1.50 eV. The exothermic energy of this step is the same as the value of that occurring on the pure RuO$_2$(110) surface. Next, another HCl molecule forms a second Cl species and is combined with O to form the second hydroxyl group. For pure RuO$_2$(110) surface, since the cus and br active sites in the energy diagram of D. Teschner et al.[36] are not that distinguished, it can be concluded that the step can even exothermically release 1.55 eV, while the calculation result by F. Sotoodeh et al. [133] is 1.50 eV. However, when the catalyst surface is doped with Cu atoms, we can find that, for the same step of HCl dissociative adsorption with Cl atom sitting on the cus site and H-transfer to O forming a hydroxyl group, will release less energy (0.9 eV) if the atomic Cl is adsorbed on the Cu$_{cus}$ site.

The formation of surface water can occur via a H transfer between neighboring OH groups, which is an endothermic process. On the pure RuO$_2$(110) surface, without distinguishing the cus and br active sites, the process determined by D. Teschner et al. is endothermic by only 0.2 eV, while two adjacent OH$_{br}$ recombined to form the

adsorbed H_2O molecules in F. Sotoodeh's work require 1.0 eV to activate the process. In our study, the dopant Cu to replace the Ru_{cus} atom can change the activity of br active site. From Figure 5.4, it can be found that the step of the formed water molecule sitting on br_2 site (i.e. neighboring Cu_{cus} site) needs an endothermic 1.8 eV, and the atomic water molecule adsorbed on br_1 site (i.e. neighboring Ru_{cus} site) requires a higher activation energy of 3.0 eV. Surface water desorption on pure $RuO_2(110)$ is endothermic by 0.85 eV[36] and 0.80 eV[133], while the step reacting over Cu-doped $RuO_2(110)$ only needs 0.1 eV and 0.4 eV to be desorbed from br_1 and br_2 sites, respectively.

At last, the recombination of two Cl species is also an endothermic step. This step is endothermic by more than 2.0 eV on the pure $RuO_2(110)$, while this endothermicity is decreased to 1.4 eV with the addition of Cu dopant atoms. This is less than the activation energy of two hydroxyl groups recombining to form one surface water. That means, in our case, the recombination of chlorine is no longer the most demanding step. Instead, the recombination of hydroxyl groups to form surface water molecules becomes the reaction rate-determining step.
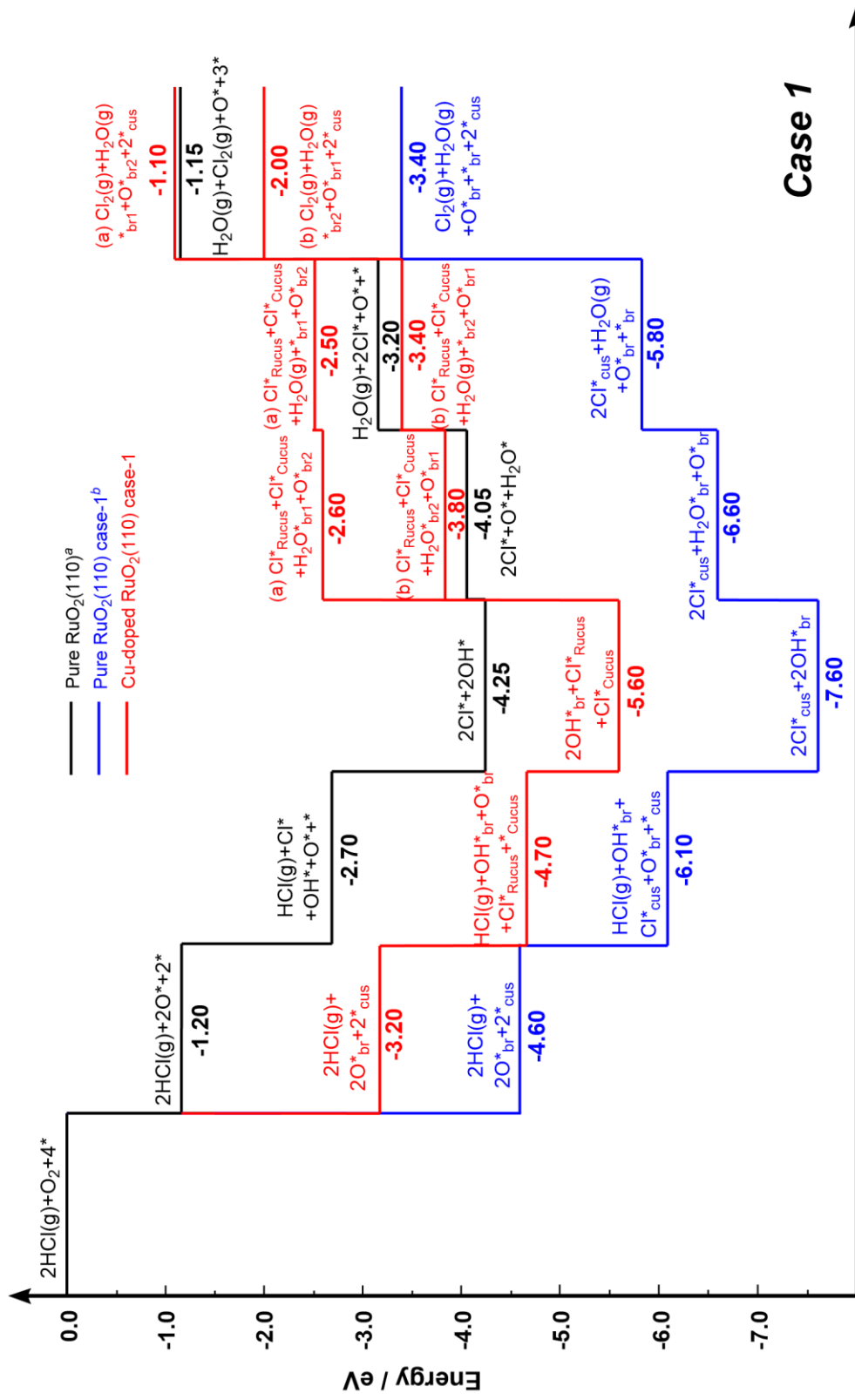
Figure 5.4 Energy diagram for Deacon process over pure $RuO_2(110)$ and Cu-doped $RuO_2(110)$ catalyst surface. The profiles correspond to the reaction $2HCl + O_2 \rightarrow Cl_2 + H_2O + O^*$ leaving an oxygen atom on the surface and involving four active sites. Hence, not the whole catalytic cycle is depicted. The energies of missing steps are the repetition of the shown ones, and the other energy barriers can be found in Table 5.2. The blue and red lines show the case that dissociation of O_2 molecule generates two O species, both of which are adsorbed on the br site, called Case-1. [a] Reference 36; [b] Reference 133.

Figure 5.5 shows that the reaction begins with O_2 dissociation to form two adsorbed O species both at the cus sites. It indicates that, in comparison with the adsorbed O species both at the br sites, the activation energy of this step has reduced no matter on pure RuO_2(110) or on the modified RuO_2(110), with an energy of 2.0 eV [36,67] and 1.2 eV, respectively. Then, HCl molecules are adsorbed onto the surface and decomposed into the adsorbed Cl and OH species. It can be seen that the released energies are all higher than 1.5 eV.[36] On the doped surface, this activation energy is slightly increased to 1.8 eV with the formed hydroxyl group adsorbing on the Ru_{cus} site. This energy is smaller than the 2.6 eV calculated by F. Sotoodeh et al.[133] If the adsorbed OH species sits on the Cu_{cus} site, it will even be an exothermic 3.3 eV.

Subsequently, the dissociative adsorption of another HCl molecule leads to a second Cl and OH surface species pair, the activation energy of which is the same as above. The two hydroxyl groups are recombined to yield an O atom with the formed surface water molecule located at the cus site. For this, only minimal (e.g. 0.2eV [36]) or no heat of adsorption is required. However, there is an exception if the formed water molecules sits on the Ru_{cus} site, with the reaction occurring on the doped catalyst surface. The process under this condition is endothermic (2.1 eV).

The process of water desorption in case-2 for water molecules sitting on the cus site at the pure RuO_2(110) surface is endothermic by 1.10 eV, higher than 0.80 eV[127] by that on the br site. In contrast, the water molecules that locate on the cus site over Cu-doped RuO_2(110) are more readily desorbed to the gas phase, with slightly endothermic energies of 0.4 eV and 0.1 eV for H_2O molecule sitting at Ru_{cus} and Cu_{cus} sites, respectively.

At the final step of the production of chlorine gas, it can be found that the heat of adsorption required for Cl_{cus}-Cl_{cus} recombination to generate Cl_2 gas is much higher than that required for two adjacent Cl_{br} atoms to produce chlorine gas (4.2 eV > 2.4 eV, 3.2 eV > 1.4 eV), regardless of the addition of dopant Cu or not. However, with the addition of doped Cu, the heat absorption of Cl recombination is decreased to 3.2 eV, which is less than the 4.2eV at the pure RuO_2(110) surface, suggesting that the addition of the dopant Cu is favorable to Cl_{cus}-Cl_{cus} recombination and Cl_2 desorption. It can also be seen from Figure 5.5 that, under T = 573 K in case-2, the chlorine recombination step still keeps the highest energetic barrier, and determines the reaction rate.
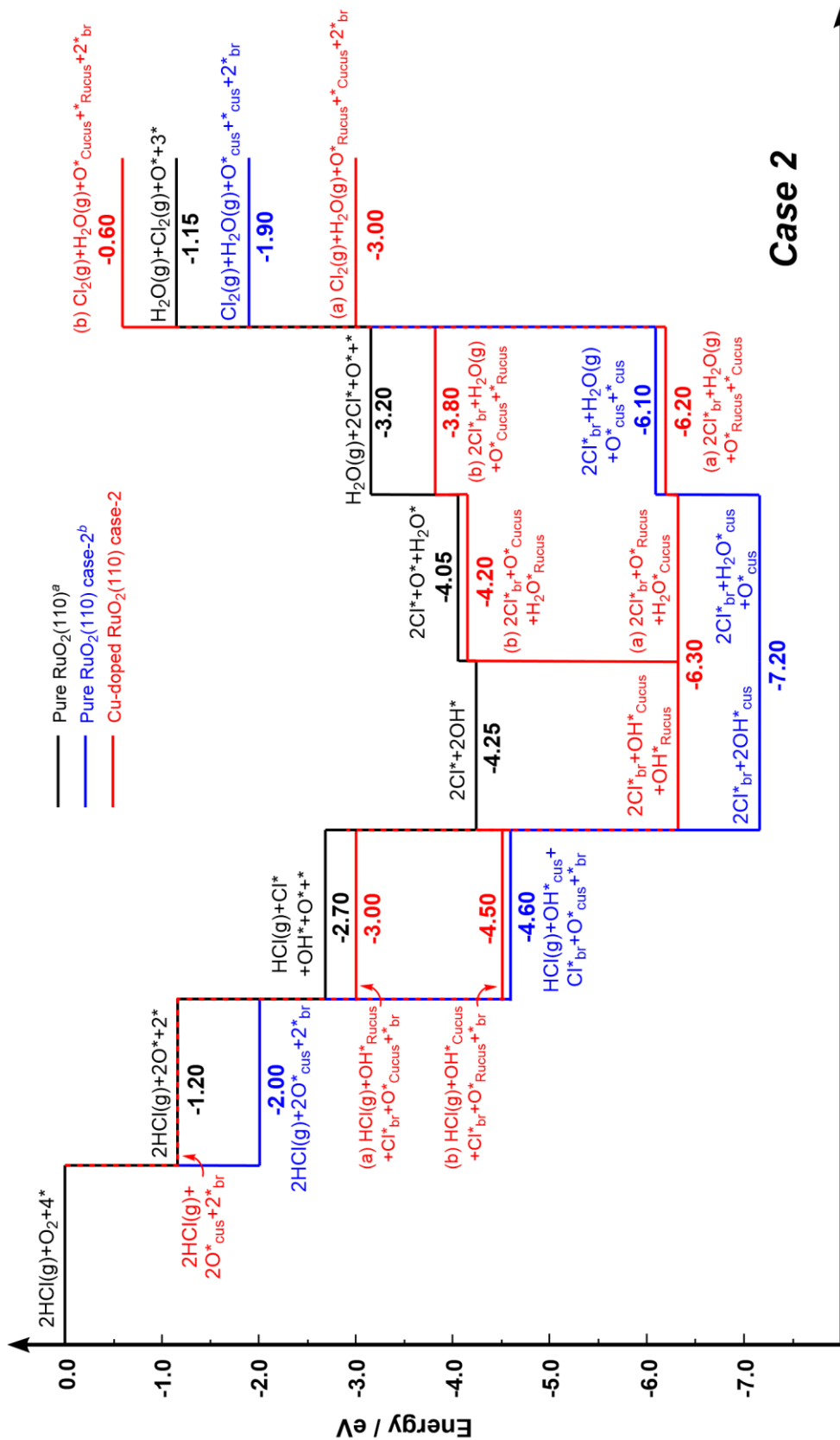
Figure 5.5 Energy diagram for Deacon process over pure $RuO_2(110)$ and Cu-doped $RuO_2(110)$ catalyst surface. The profiles correspond to the reaction $2HCl + O_2 \rightarrow Cl_2 + H_2O + O^*$ leaving an oxygen atom on the surface and involving four active sites. Hence, not the whole catalytic cycle is depicted. The energies of missing steps are the repetition of the shown ones, and the other energy barriers can be found in Table 5.2. The blue and red lines show the case that dissociation of O_2 molecule generates two O species, both of which are adsorbed on the cus site, called Case-2. [a] Reference 36; [b] Reference 133.

In Figure 5.6 (case-3), the dissociative adsorption of an O_2 molecule generates an atomic O_{br} and an O_{cus} species. The data at pure $RuO_2(110)$ shows that the exothermicity of this process increases to 3.3 eV.[67,133] In contrast, the value of activation energy for the process over Cu-doped $RuO_2(110)$ is affected by the specific cus site. It releases only 0.2 eV heat when the O_2 molecule is dissociated at br and Cu_{cus} sites. In comparison, it is exothermic by the quite high heat of 2.5 eV when the O species sits on br and Ru_{cus} sites. But both of the released heats are lower than that on pure $RuO_2(110)$ (3.3 eV).[133]

In the following two steps, a HCl molecule is adsorbed and decomposed into surface-adsorbed Cl and OH species. The activation energy of the process can be changed due to the respective location of the Cl and OH species. If HCl molecules on pure $RuO_2(110)$ surface are adsorbed and decomposed into OH_{br} and Cl_{cus}, the exothermicity is 1.5 eV, which is consistent with the result of D. Teschner et al.. If the HCl molecule is dissociated into OH_{cus} and Cl_{br}, the released heat increases to 2.6 eV.

The adsorption of HCl molecules and hydrogen abstraction to form Cl and OH species become much more complicated at the Cu-doped $RuO_2(110)$ surface. Besides the correlation between the adsorption sites of the OH and Cl species on the surface, the order of the two OHs formed at the Ru_{cus} or Cu_{cus} sites also leads to a change of heat release. For the Deacon reaction on the modified surface, Figure 5.6 only displays the data when the surface Cl species is first located at the br site (Cl_{br}), and H is transferred to the exact O_{cus} site adjacent to Cl_{br} to form $O_{cus}H$, namely, "$Cl_{br1}+OH_{Rucus}$" and "$OH_{br2}+OH_{Cucus}$". The DFT calculations show that, when the surface OH species are located at a specific cus site (Cu_{cus} and Ru_{cus}), the atomic Cl located at br site (br_1 or br_2) leads a negligible difference in the activation energy of the step. In Figure 5.6, the first HCl molecule on the Cu-doped $RuO_2(110)$ surface is decomposed into "$OH_{Rucus}+Cl_{br}$", which is exothermic by 1.8 eV. In comparison, the formation of "$OH_{Cucus}+Cl_{br}$" releases 3.3 eV, suggesting that H abstraction from the HCl molecule, in this case, is more easy to O_{Cucus}, thus forming OH_{Cucus}. Accordingly, the adsorption of the second HCl molecule on the doped surface forms "$OH_{Rucus}+Cl_{br}$" and "$OH_{Cucus}+Cl_{br}$" species, which is exothermic by 1.5 eV and 0.9 eV, respectively.

Subsequently, the recombination of two hydroxyl groups goes through a second H transfer to generate an adsorbed surface water molecule with the remaining surface

oxygen atom. On the pure RuO_2(110) surface, if the water molecules are generated and adsorbed on the br site during the reaction, this would need 1.30 eV to activate, while only 0.30 eV would be required if the generated water molecules are adsorbed at the cus site. The latter value is very close to the 0.2 eV determined by D. Teschner et al.,[36] reflecting that the cus site is more conducive to the adsorption of water than the br site.

On the Cu-doped RuO_2(110) surface, in consideration of the location of the adsorbed water species as well as the sites of the remaining atomic oxygen, four different cases for water formation are obtained from Figure 5.6: 1) $H_2O_{br1}+O_{Rucus}$, endothermic by 2.20 eV (a1); 2) $H_2O_{Rucus}+O_{br1}$, endothermic by 1.90 eV (a2); 3) $H_2O_{br2}+O_{Cucus}$, endothermic by 1.70 eV (b1); 4) $H_2O_{Cucus}+O_{br2}$, endothermic by 1.00 eV (b2). It can be seen that, except for the fourth case, the endothermicity for the other cases is higher than that of the process reacting on the pure RuO_2(110).

For pure RuO_2(110), the water molecules are subsequently desorbed from the surface. For the removal of water molecules from the br site, this is endothermic by 0.80 eV[36] or 0.85 eV[133]. The adsorbed heat increases to 1.10eV[133] for water molecules desorbed from the cus site. When a Cu substituted a Ru atom at the cus site of RuO_2(110) catalyst surface, it can be seen that the endothermicity of water desorption is quite low, with only 0.1ev or 0.4ev required to activate the process. It means that H_2O adsorption becomes weaker along with the change of the catalyst surface.

The final Cl recombination to generate chlorine gas was determined as the energetically most demanding step in previous work.[4,36,133] According to Figure 5.6, we realize that Cl recombination on the pure RuO_2(110) is endothermic by 2.05 eV[36] and 3.40 eV[133], respectively. In contrast, on the doped RuO_2(110), the process requires a heat of 2.2 eV to form "$Cl_{br} + Cl_{Cucus}$" and 2.9 eV to form "$Cl_{br} + Cl_{Rucus}$", indicating that in case-3 Cl-Cl recombination is still the step with the highest energy requirement, thus becoming the rate-controlling step.

Figure 5.6 Energy diagram for Deacon process over pure $RuO_2(110)$ and Cu-doped $RuO_2(110)$ catalyst surface. The profiles correspond to the reaction $2HCl + O_2 \rightarrow Cl_2 + H_2O + O^*$ leaving an oxygen atom on the surface. Hence, not the whole catalytic cycle is depicted. The energies of missing steps are the repetition of the shown ones, and the other energy barriers can be found in Table 5.2. The blue and red lines show the case that dissociation of O_2 molecule generates two O species. One is adsorbed on the br site, and the other on the cus site. We called it as Case-3. [a] Reference 36; [b] Reference 133.

When comprehensively comparing the above three energy diagrams, O_2 molecules are easier to be dissociatively adsorbed at the br site, releasing more heat (3.2 eV) than in the other two cases. For the Cl recombination, the activation energy required for two adjacent Cl_{cus} species located at the cus site is lower than the energy required for the other two cases (i.e. Cl_{br}-Cl_{br}, Cl_{cus}-Cl_{br}). It is thus more facile to generate the Cl_2 product and have it desorb into the gas phase. Furthermore, in previous studies on the $RuO_2(110)$ surface, the process of Cl-Cl recombination has been identified as the step with the highest energy requirement in the mechanism. The above three energy diagrams demonstrate that, in most cases, the process is indeed the most energy requiring step. However, in Figure 5.4, when the O_2 molecules are dissociated into two atomic O species sitting on the br site of the doped surface, the formation of water molecules, that is, two hydroxyl groups recombined to generate water molecules through H transfer, is the most energetic step. It can then be expected that, when the Deacon reaction occurs over the Cu-doped $RuO_2(110)$ catalyst surface under appropriate conditions, the formation of water molecules requires higher heat than the Cl recombination and might become the rate controlling step. Moreover, the water molecules on the doped surface are more easily released to the gas phase than that on the pure $RuO_2(110)$ surface, indicating that the adsorption of water molecules on the modified catalyst surface is very weak. In conclusion, the recombination of chlorine might not be the rate-determining step under certain conditions since the recombination of OH to form absorbed water molecules requires more energy than Cl-Cl recombination. And it is more favorable for the desorption of the water molecules on Cu-doped $RuO_2(110)$ than that on the pure $RuO_2(110)$ catalyst surface.

Finally, it should be emphasized that the required energies for the endothermic steps on doped $RuO_2(110)$ surface are all much lower than the corresponding steps on pure $RuO_2(110)$, except for the water formation in case-1 and case-3 as well as HCl adsorption to generate the surface Cl_{br} and $O_{Cucus}H$ in case-2 (i.e. H atom is abstracted from the HCl molecule and transferred to on-top O_{Cucus} to form Cl_{br} and $O_{Cucus}H$ species).

5.3.3 Sensitivity analysis of the active site over Cu-doped RuO_2(110)

As mentioned above, due to the addition of the dopant Cu atoms, the two prominent active sites (cus and br) on pure RuO_2 (110) surface become four different active sites, named as Ru_{cus}, Cu_{cus}, br_1, and br_2, respectively (see Figure 5.1, right). Different activities of these sites in the elementary process of the Deacon reaction have been fully demonstrated in the above parts 5.2.1 and 5.2.2. In order to specifically evaluate the reactivity of these four active sites, namely the sensitivity of the sites, DFT calculations were carried out to compute the energy barrier of each elementary process of the Deacon reaction using the RPBE exchange-correlation function.[61] 34 basic steps were contained in the Deacon process mechanism, as compiled in table 5.2. Here, we have also taken into account all possible forms of the reaction process at each step, such as Process (12) $OH_{br} + OH_{br} \leftrightarrow O_{br} + H_2O_{br}$, which involves two possible forms: $OH_{br1} + OH_{br2} \leftrightarrow O_{br1} + H_2O_{br2}$, and $OH_{br1} + OH_{br2} \leftrightarrow O_{br2} + H_2O_{br1}$. It can also be seen in Table 5.2 that some specific processes involving similar or identical calculated energy barriers are classified into one type. For example, the products formed in process (1) with "Cl_Ru_{cus} and OH_br" may stand for "Cl_Ru_{cus} and OH_br_1" and "Cl_Ru_{cus} and OH_br_2". Since the calculated energy barriers of the two cases are almost the same, we regard it as one case, namely "Cl_Ru_{cus} and OH_br". Herein, the diffusion process of each surface species on the modified catalyst surface is analyzed, all as shown in Figure 5.7.

Figure 5.7 indicates that, on the pure RuO_2(110) surface, there is no significant energy barrier for the diffusion of each surface species (Cl, O, OH, H_2O) between two br sites or between two cus sites (also see Table 5.1). A substantial energy barrier only exists for the diffusion between one cus and one br site, no matter which specific cus or br site, because the energy barrier from cus to br_1 is the same as that from cus to br_2. The activity of both the cus and br sites in the same category keeps the same over the pure RuO_2(110). However, the activity of each site is changed if the dopant Cu atoms are added, and the energy barrier of the diffusion process between each adjacent active site becomes different, as demonstrated in Figure 5.7.
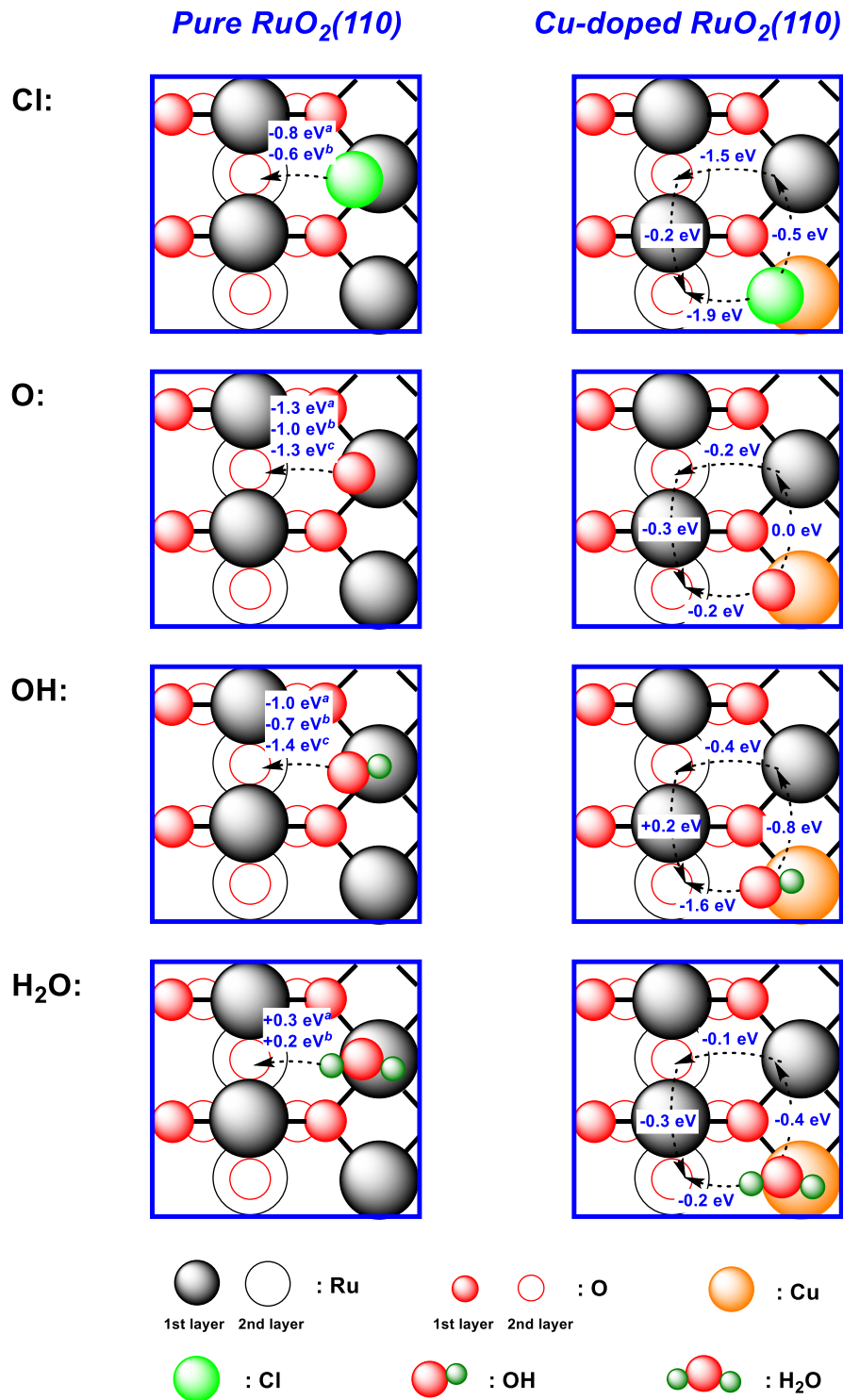
Figure 5.7 Comparison diagram: energy barriers for diffusion steps of surface species (Cl, O, OH, H₂O) in the Deacon reaction over pure RuO₂(110) and Cu-doped RuO₂(110) surface. [a] Ref. 133; [b] Ref. 72; [c] Ref. 65.

As shown in Figure 5.7, the calculated energy barriers for the diffusion process of Cl, O, OH (except H_2O) species over the pure RuO_2(110) catalyst surface from cus site to br site are all negative, indicating that Cl, O and OH tend to diffuse from cus site to br site. Thus, surface adsorption of these three species may occur at br sites rather than at cus sites. If copper is doped at the catalyst surface, assuming that the Cu atom replaces Ru on the cus site, it can be found that the activation energies of diffusion for all surface species including water from cus to br show negative values. So in this case, all the atoms also tend to be adsorbed at the br site.

For the diffusion on the Cu-doped RuO_2(110), except for O species, the activation energies of diffusion between cus and cus sites are lower than those between br and br sites, indicating that the activity of cus sites is significantly affected by the addition of dopants, but the activity of br site is less affected. It can also be found that energy barriers exist between the two cus sites or between the two br sites, except for the diffusion of O atoms between the two cus sites (whose diffusion value is almost 0.0 eV). Although some values are close to zero, between the two cus sites it shows the tendency of diffusion from Cu_{cus} to Ru_{cus} site; between the two br sites it shows the tendency of diffusion from br_1 to br_2 site. Only one exception exists – between the two br sites, OH species tends to diffuse from br_2 to br_1. This very intriguing finding indicates that centered at the Cu_{cus} site, all the surface species prefer to spread from Cu_{cus} site to other sites. It also illustrates that the Cu_{cus} site where the dopant Cu atoms are located has very high activity and is not conducive to be adsorbed by surface species, which is beneficial to its adjacent sites to be adsorbed so that we can maintain Cu_{cus} sites idle and keep them highly active. This function of Cu dopants promotes the release of surface species from Cu_{cus} and facilitates adsorption to their adjacent sites, thus accelerating the reaction rate. Perhaps it can be called as the "selectivity" of the active site on the doped surface. Therefore, we can conclude that cus sites show a much higher sensitivity to the activity than br site on the Cu-doped RuO_2(110) catalyst surface, especially the Cu_{cus} site is the most sensitive for the reaction activity.

In addition, comparing the activation energy values of diffusion for the surface species from cus site to br site, it can be found that through doping Cu into the RuO_2(110) catalyst surface, the activation energy values of diffusion from Cu_{cus} to br_2 is lower than

those from Ru_{cus} to br_1. Compared with Cl diffusion on the pure $RuO_2(110)$ surface, it is easier for Cl species to diffuse from cus to br site on the modified catalyst surface. As shown in Figure 5.7, its ΔE value is more negative than that on the pure $RuO_2(110)$ surface. For O species, the ΔE value of diffusion from cus to br on pure RuO_2 (110) is more negative, indicating that O species on pure RuO_2 (110) are more likely to diffuse, while on the doped catalyst surface the diffusion tendency of O species from cus to br is much weaker. For OH species spreading from cus to br site, it can be found that the ΔE value of diffusion from Cu_{cus} to br_2 is much lower than the ΔE value from Ru_{cus} to br_1. This result further confirms that the activity of each active site is affected by the Cu dopant, and cus and br sites show different activities. Especially, the Cu_{cus} site is supposed to be the most active site. Last, the ΔE value of surface-adsorbed H_2O species is also decreased. On the pure RuO_2 (110) surface, H_2O diffusion tends to spread from br to cus, while on the Cu-doped catalyst surface, H_2O diffusion slightly inclines to spread from cus to br.

5.4 Conclusion

In the last chapter, it was concluded that Cu is an optimal dopant that can be used for the $RuO_2(110)$ surface. In this chapter, when a Ru atom is substituted by a Cu atom at the cus site of $RuO_2(110)$, the reaction mechanism is greatly affected and the activity of the catalyst is indeed enhanced. DFT calculations reveal that the oxidation of HCl with molecular O_2, producing Cl_2 and the byproduct water, proceeds over Cu-doped $RuO_2(110)$ surfaces via a one-dimensional Langmuir-Hinshelwood-Hougen -Watson (LHHW) mechanism. Most of the activation barriers of the basic steps are determined by the adsorption energy of the reaction intermediates, such as water and chlorine. In the previous work,[4,29] either O_2 dissociation or Cl-Cl recombination (reactions 5-7 and reactions 8-10 in Table 5.2, respectively) was regarded to be the rate-determining step (r.d.s) in the Deacon reaction. In a Langmuir-Hinshelwood -based kinetic model proposed by F. Studt et al.,[38] both of these two processes were assumed to equally control the overall reaction rate.

The results here clearly show that, at T = 573K, the rate-limiting step of the Deacon process over the modified catalyst surface is still the Cl recombination process in most

cases (in contrast to what has been assumed in several preceding studies[4,29,38]). However, under certain conditions, when O_2 molecules are first adsorbed at both br sites to generate two O_{br} species, the formation of water molecules is identified to have the highest activation barrier (+3.0 eV or +1.8 eV) for this system. It thus becomes the step that determines the whole reaction rate.

Meanwhile, the results calculated by DFT indicate that the energy barriers of all endothermic steps on the doped surface are generally lower than those of the corresponding steps on the pure RuO_2(110) surface. This suggests that the reaction on the modified surface is greatly improved.

Sensitivity analysis of the active site in the Deacon reaction over Cu-doped RuO_2(110) revealed that the adjacent sites around the doped position are all affected. Compared with the br site, the effect on the cus site is more pronounced. Unlike the pure catalyst surface, the Cu_{cus} site shows the highest activity on the modified surface, and all surface species tend to diffuse from the Cu_{cus} site to other surrounding sites. All energy barriers in this direction are found to be negative, indicating that these all belong to exothermic reactions. The addition of a few dopants to the catalyst surface will bring this interesting "selectivity". In principle, it ensures that the active vacancies are not easily occupied while accelerating the reactivity of the surrounding sites.

Since no previous attempts have been made for the Deacon process to dope other metal atoms on the RuO_2(110) catalyst surface, few meaningful experimental data are available. However, our presented results demonstrate that the addition of dopants is a bold but worthwhile attempt to perfect the design of the Deacon catalyst and improve the reaction rate. Furthermore, the chlorination phenomenon during the Deacon reaction over the pure RuO_2(110) surface has been proven by experiments and theories.[29,72,123,134] How about the chlorination of the Deacon process on the Cu-doped RuO_2(110) surface doped with Cu? So far, this is still unknown. To fully assess the effects of chlorination on the Cu-doped catalyst surface and the reaction mechanism or rate, future work will have to establish a kinetic Monte Carlo (kMC) model based on the extensive set of first-principles data compiled in this chapter.

Chapter 6

Summary and outlook

The Deacon process, as a green recycling process, has been studied for a long time. In the Deacon reaction, HCl, a common waste by-product, can be transformed into chlorine gas with practical value, and the only by-product is environmentally friendly water. Both experimental and theoretical simulations have been committed to elaborating the reaction mechanism, and to improve the Deacon catalyst or finding better catalyst alternatives to enhance the reactivity. Our approach here focused on microscopic studies of the reaction mechanisms and the relationship between first-principles microkinetics and widely used empirical reaction-kinetic models

In this dissertation, our work proceeded in three stages. First of all, the Deacon reaction has been studied on the pure $RuO_2(110)$ surface. We established reasonable reaction-kinetic models combined with limited available experimental data, and carried out direct data fitting as well as first-principles calculations to determine the rate constants. We compared the established microkinetic models (empirical vs. first-principles) in terms of the predicted surface coverages, and in terms of the predicted reaction rate and surface species ratio when effectively widening the range of operating conditions (both the reactant HCl and O_2 partial pressure ranges are effectively enlarged from 0.01 bar to 100 bar). Despite some differences and ambiguities, the models generally agree on the Cl_2 recombination step as the rate-determining step on the pure $RuO_2(110)$ surface.

With this understanding, we screened for suitable dopant atoms to increase the activity of the Deacon process. Specifically, we considered a doped $RuO_2(110)$ surface in which we replaced one Ru atom at the cus site with another metal atom. We tested 22 metal species that can be used as possible dopants. By calculating the Cl desorption energy (assuming the Cl-Cl recombination process as the rate-determining step) and the dopant segregation energy, we first identified several potential metal atoms with

high reactivity and relatively good stability. Later, by calculating and comparing the formation free energy of these chosen atoms and their corresponding metal oxides in the oxygen-rich environment of the Deacon process, we finally determinend Cu as the optimal dopant.

In a final chapter, we then established an extensive energetic data set for the elementary Deacon processes at a Cu-doped $RuO_2(110)$ surface. We calculated first-principles rate constants by determining the energetic barriers through the LST/QST methods and then applying transition state theory. Systematically analyzing the derived data set and comparing it to the corresponding data for the pure $RuO_2(110)$ surface, we arrived at some first insight into the effect of such Cu doping. As expected, adsorption at the more noble Cu atoms is weaker as compared to Ru. The induced changes seem to be large enough to possibly lead to a change of the rate-determining step away from the Cl-Cl recombination and desorption under appropriate conditions. A full verification of this assessment will now require detailed microkinetic simulations on the basis of the here calculated energetic data set. To appropriately capture the localized effect of the surface Cu dopant atoms, this will have to be kinetic Monte Carlo simulations that fully resolve the spatial distribution of the reaction intermediates at the trench-like surface structure of $RuO_2(110)$. The present data nevertheless already indicate the viability of a doping strategy involving Cu. We plan to conduct such simulations in the future. Also smaller RuO_2 nanoparticles could be particularly interesting for doping strategies. Especially because of a gap opening, the nanoparticles perhaps allow for longer-ranged doping effects than the otherwise metallic RuO_2.

Chapter 7

Appendix

A. The LHHW microkinetic models

The Deacon Process can be written as follows:

$$HCl + O_2 \xleftarrow{\quad Catalyst \quad} Cl_2 + H_2O$$

The mechanism of the above Deacon Process over $RuO_2(110)$ surface has been studied with a LHHW model, and its elementary steps are summarized in Table 3.1. Based on the previous assumptions, the two steps in Table 3.1 might determine the reaction rate, namely the dissociative adsorption of oxygen or recombination of surface chlorine atoms to yield Cl_2 gas. In addition, both of the two steps are assumed to have the same effect to control reaction rate, so in this case, both of these two steps can be the rate-determining step simultaneously. Therefore, we can obtain three different LHHW microkinetic models (see Chapter 3).

A.1. O₂-diss. Model

The first LHHW microkinetic model is O_2 dissociation model. In this LHHW model, O_2 dissociation process is proposed to be rate controlling, which is named as O_2 dissociation model and abbreviated as "O₂-diss. Model". Each elementary process and the corresponding constant can be written as the following Table A.1.

Where * denotes the vacant site over the $RuO_2(110)$ surface or a surface site. K_i represents the equilibrium constants of the step i (i = 1, 2, 3, 4). k represents the forward rate constant. C_T represents the total concentration of surface site, often nearly 1.

Table A.1. Elementary steps in Deacon process in the 1st LHHW model (O_2-diss. model).

Step	Surface Reaction	Constant
1	HCl + O* + * $\rightleftharpoons$ Cl* + OH*	K_1
2	OH* + OH* $\rightleftharpoons$ H_2O* + O*	K_2
3	Cl* + Cl* $\rightleftharpoons$ Cl_2 + 2*	K_3
4	H_2O* $\rightleftharpoons$ H_2O + *	K_4
5	O_2 + 2* $\rightarrow$ 2O* (r.d.s.)	k

Since step (5) is proposed to be rate-limit, it is the slowest step of the whole reaction, with other steps being equilibrated and reversible. To generalize the reversible surface reaction, we consider an equilibrium elementary reaction of the adsorbed molecules A and B to yield C and D:

$$v_A \, \text{A*} + v_B \text{B*} \underset{k_-}{\overset{k_+}{\rightleftharpoons}} v_P \, \text{P*} + v_Q \, \text{Q*} \qquad (A.1)$$
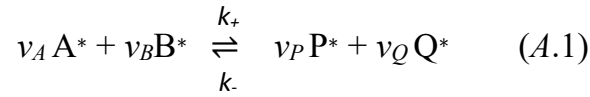
where k_+ and k_- are the forward and reverse rate constants, respectively.

According to the reaction *A*.1, the rate of the forward reaction, $r_{forward}$, can be written as

$$r_{forward} = k_+ \left[A^*\right]^{v_A} \left[B^*\right]^{v_B} \qquad (A.2)$$

Here $[X^*]$ represents the concentration of the surface species X^*, which can also be normalized to the number of active sites and v_i is the stoichiometric factor.

Similarly, we can obtain the rate of the reverse reaction, $r_{reverse}$, as the below *A*.3.

$$r_{reverse} = k_- \left[C^*\right]^{v_C} \left[D^*\right]^{v_D} \qquad (A.3)$$

At the equilibrium constant, the rate of the forward reaction is equal to that of the

reverse reaction, i.e., $r_{forward} = r_{reverse}$. Therefore, we can get the following expression

$$k_+ [A^*]^{\nu_A} [B^*]^{\nu_B} = k_- [C^*]^{\nu_C} [D^*]^{\nu_D} \qquad (A.4)$$

The equilibrium constant for this reaction can be expressed as

$$K = \frac{k_+}{k_-} = \frac{[C^*]^{\nu_C} [D^*]^{\nu_D}}{[A^*]^{\nu_A} [B^*]^{\nu_B}} \qquad (A.5)$$

Therefore, the balanced reaction rate is obtained:

$$r = k_+ [A^*]^{\nu_A} [B^*]^{\nu_B} - k_- [C^*]^{\nu_C} [D^*]^{\nu_D} \qquad (A.6)$$

According to $A.5$, we can obtain the equilibrium constants of the four reverse steps in

Table A.1, which can be shown as follows:

$$K_1 = \frac{k_1}{k_{-1}} = \frac{\theta_{Cl}\theta_{OH}}{p_{HCl}\theta_O\theta_v} \qquad (A.7)$$

$$K_2 = \frac{k_2}{k_{-2}} = \frac{\theta_{H_2O}\theta_O}{\theta_{OH}^2} \qquad (A.8)$$

$$K_3 = \frac{k_3}{k_{-3}} = \frac{p_{Cl_2}\theta_v^2}{\theta_{Cl}^2} \qquad (A.9)$$

$$K_4 = \frac{k_4}{k_{-4}} = \frac{p_{H_2O}\theta_v}{\theta_{H_2O}} \qquad (A.10)$$

Where θ_{Cl}, θ_{OH}, θ_O, θ_{H2O} and θ_v represents the concentration of Cl^*, OH^*, O^*, H_2O^* atoms

and the vacant site on the surface, respectively.

Based on equation $A.9$, we can get that

$$K_3 = \frac{p_{Cl_2}\theta_v^2}{\theta_{Cl}^2} \Rightarrow \theta_{Cl}^2 = \frac{p_{Cl_2}\theta_v^2}{K_3} \Rightarrow \theta_{Cl} = \sqrt{\frac{p_{Cl_2}\theta_v^2}{K_3}} = K_3^{-0.5} p_{Cl_2}^{0.5} \theta_v = K_{Cl} p_{Cl_2}^{0.5} \theta_v$$

$$\theta_{Cl} = K_3^{-0.5} p_{Cl_2}^{0.5} \theta_v = K_{Cl} p_{Cl_2}^{0.5} \theta_v \qquad \left(K_{Cl} = K_3^{-0.5}\right) \qquad (A.11)$$

Based on equation *A*.10, we can get that

$$K_4 = \frac{p_{H_2O}\theta_v}{\theta_{H_2O}} \Rightarrow \theta_{H_2O} = \frac{p_{H_2O}\theta_v}{K_4} = K_{H_2O} p_{H_2O} \theta_v$$

$$\theta_{H_2O} = K_{H_2O} p_{H_2O} \theta_v \qquad \left(K_{H_2O} = K_4^{-1}\right) \qquad (A.12)$$

Then we used equation *A*.7 to multiply equation *A*.8, so

$$K_1 \cdot K_2 = \frac{\theta_{Cl}\theta_{OH}}{p_{HCl}\theta_O\theta_v} \cdot \frac{\theta_{H_2O}\theta_O}{\theta_{OH}^2} = \frac{\theta_{Cl}\theta_{H_2O}}{p_{HCl}\theta_{OH}\theta_v} \Rightarrow \theta_{OH} = \frac{\theta_{Cl}\theta_{H_2O}}{K_1 K_2 p_{HCl}\theta_v} \qquad (A.13)$$

We combined it with the above equations *A*.11 and *A*.12, and get

$$\theta_{OH} = \frac{\theta_{Cl}\theta_{H_2O}}{K_1 K_2 p_{HCl}\theta_v} = \frac{K_{Cl} p_{Cl_2}^{0.5}\theta_v \cdot K_{H_2O} p_{H_2O}\theta_v}{K_1 K_2 p_{HCl}\theta_v} = \frac{K_{Cl} K_{H_2O} p_{Cl_2}^{0.5} p_{H_2O}\theta_v}{K_1 K_2 p_{HCl}} = K_{OH} p_{Cl_2}^{0.5} p_{H_2O} p_{HCl}^{-1}\theta_v$$

$$K_{OH} = \frac{K_{Cl} K_{H_2O}}{K_1 K_2} = \frac{K_3^{-0.5} K_4^{-1}}{K_1 K_2} = K_1^{-1} K_2^{-1} K_3^{-0.5} K_4^{-1}$$

$$\theta_{OH} = K_{OH} p_{HCl}^{-1} p_{Cl_2}^{0.5} p_{H_2O}\theta_v \qquad \left(K_{OH} = K_1^{-1} K_2^{-1} K_3^{-0.5} K_4^{-1}\right) \qquad (A.14)$$

Based on equation *A*.8, we can obtain the expression of θ_O. In addition, we combined equations *A*.12 and *A*.14.

$$\theta_O = \frac{K_2 \theta_{OH}^2}{\theta_{H_2O}} = \frac{K_2 \cdot \left(K_{OH} p_{Cl_2}^{0.5} p_{H_2O} p_{HCl}^{-1}\theta_v\right)^2}{K_{H_2O} p_{H_2O}\theta_v} = \frac{K_2 K_{OH}^2 p_{Cl_2}^1 p_{H_2O} p_{HCl}^{-2}\theta_v}{K_{H_2O}} = K_O p_{Cl_2} p_{H_2O} p_{HCl}^{-2}\theta_v$$

$$\theta_O = K_O p_{HCl}^{-2} p_{Cl_2} p_{H_2O}\theta_v \qquad \left(K_O = K_1^{-2} K_2^{-1} K_3^{-1} K_4^{-1}\right) \qquad (A.15)$$

$$K_O = \frac{K_2 K_{OH}^2}{K_{H_2O}} = \frac{K_2 \left(K_1^{-1} K_2^{-1} K_3^{-0.5} K_4^{-1} \right)^2}{K_4^{-1}} = K_2 K_1^{-2} K_2^{-2} K_3^{-1} K_4^{-1} = K_1^{-2} K_2^{-1} K_3^{-1} K_4^{-1}$$

Considering pseudo-steady state for the surface intermediates and neglecting concentrations of HCl, O_2 and Cl_2 gases, the balance of a total site can be obtained as

$$\theta_O + \theta_{OH} + \theta_{Cl} + \theta_{H_2O} + \theta_v = 1 \qquad (A.16)$$

According to equations of θ_{Cl}, θ_{OH}, θ_O and θ_{H2O}, we got the expression for θ_v as follows

$$1 = \theta_O + \theta_{OH} + \theta_{Cl} + \theta_{H_2O} + \theta_v$$
$$= K_O p_{Cl_2} p_{H_2O} p_{HCl}^{-2} \theta_v + K_{OH} p_{Cl_2}^{0.5} p_{H_2O} p_{HCl}^{-1} \theta_v + K_{Cl} p_{Cl_2}^{0.5} \theta_v + K_{H_2O} p_{H_2O} \theta_v + \theta_v$$
$$= (K_O p_{Cl_2} p_{H_2O} p_{HCl}^{-2} + K_{OH} p_{Cl_2}^{0.5} p_{H_2O} p_{HCl}^{-1} + K_{Cl} p_{Cl_2}^{0.5} + K_{H_2O} p_{H_2O} + 1) \theta_v$$

$$\Rightarrow \theta_v = (K_O p_{HCl}^{-2} p_{Cl_2} p_{H_2O} + K_{OH} p_{HCl}^{-1} p_{Cl_2}^{0.5} p_{H_2O} + K_{Cl} p_{Cl_2}^{0.5} + K_{H_2O} p_{H_2O} + 1)^{-1} \qquad (A.17)$$

Therefore, the 1st LHHW model can be written as

$$r = k \cdot p_{O_2} \cdot \theta_v^2 \Rightarrow$$

$$r = k p_{O_2} \left(K_O p_{HCl}^{-2} p_{Cl_2} p_{H_2O} + K_{OH} p_{HCl}^{-1} p_{Cl_2}^{0.5} p_{H_2O} + K_{Cl} p_{Cl_2}^{0.5} + K_{H_2O} p_{H_2O} + 1 \right)^{-2} \qquad (A.18)$$

Here,

$$K_O = K_1^{-2} K_2^{-1} K_3^{-1} K_4^{-1} \qquad K_{OH} = K_1^{-1} K_2^{-1} K_3^{-0.5} K_4^{-1}$$
$$K_{Cl} = K_3^{-0.5} \qquad K_{H_2O} = K_4^{-1}$$

A.2. Cl₂-recom. model

The second LHHW microkinetic model is Cl_2 recombination model. In this LHHW model, Cl_2 recombination process is proposed to be rate determining.[33] We named this model as Cl_2 recombination model and abbreviated as "Cl₂-recom. model". The below Table A.2 shows every elementary process and the corresponding constant.

It can be found that the recombination of two adjacent chlorine atoms on the surface generally needs the highest barrier, so the chlorine recombination is assumed to be rate-determining in the Deacon-like process. In Table A.2, only step (2) can be proposed to be rate limit, with other steps being equilibrated.

Table A.2. Elementary steps in Deacon process in the 2nd LHHW model (Cl_2-recom. model).

Step	Surface Reaction	Constant
1	HCl + O* + * ⇌ Cl* + OH*	K_1
2	OH* + OH* ⇌ H_2O* + O*	K_2
3	Cl* + Cl* → Cl_2 + 2* (r.d.s)	k
4	H_2O* ⇌ H_2O + *	K_4
5	O_2 + 2* ⇌ 2O*	K_5

In the same way, we can get the expressions for each equilibrium constant and the rate of the whole reaction.

$$K_1 = \frac{k_1}{k_{-1}} = \frac{\theta_{Cl}\theta_{OH}}{p_{HCl}\theta_O\theta_v} \qquad (A.19)$$

The rate of the reaction can be expressed as the follows

$$K_2 = \frac{k_2}{k_{-2}} = \frac{\theta_{H_2O}\theta_O}{\theta_{OH}^2} \qquad (A.20)$$

$$K_4 = \frac{k_4}{k_{-4}} = \frac{p_{H_2O}\theta_v}{\theta_{H_2O}} \qquad (A.21)$$

$$K_5 = \frac{k_5}{k_{-5}} = \frac{\theta_O^2}{p_{O_2}\theta_v^2} \qquad (A.22)$$

Based on equation *A*.22, we can get

$$K_5 = \frac{\theta_O^2}{p_{O_2}\theta_v^2} \Rightarrow \theta_O^2 = K_5 p_{O_2}\theta_v^2 \Rightarrow \theta_O = \sqrt{K_5 p_{O_2}\theta_v^2} = K_5^{0.5} p_{O_2}^{0.5}\theta_v = K_o p_{O_2}^{0.5}\theta_v$$

$$\theta_O = K_O p_{O_2}^{0.5}\theta_v \qquad \left(K_O = K_5^{0.5}\right) \qquad (A.23)$$

Similarly, based on equation *A.21*, we obtain

$$K_4 = \frac{p_{H_2O}\theta_v}{\theta_{H_2O}} \Rightarrow \theta_{H_2O} = \frac{p_{H_2O}\theta_v}{K_4} = K_4^{-1} p_{H_2O}\theta_v = K_{H_2O} p_{H_2O}\theta_v$$

$$\theta_{H_2O} = K_{H_2O} p_{H_2O}\theta_v \qquad \left(K_{H_2O} = K_4^{-1}\right) \qquad (A.24)$$

And according to equation *A.20*, we get

$$K_2 = \frac{\theta_{H_2O}\theta_O}{\theta_{OH}^2} \Rightarrow \theta_{OH}^2 = \frac{\theta_{H_2O}\theta_O}{K_2} \qquad (A.25)$$

Then we substituted the expressions of θ_O, θ_{H2O} into equation *A.25*, and got

$$\theta_{OH}^2 = \frac{\theta_{H_2O}\theta_O}{K_2} = \frac{K_{H_2O} p_{H_2O}\theta_v \cdot K_O p_{O_2}^{0.5}\theta_v}{K_2} = K_2^{-1} K_{H_2O} K_O p_{H_2O} p_{O_2}^{0.5}\theta_v^2$$

Next, put the expressions of K_{H_2O} and K_O into the above equation,

$$\theta_{OH}^2 = K_2^{-1} K_{H_2O} K_O p_{H_2O} p_{O_2}^{0.5}\theta_v^2 = K_2^{-1} K_4^{-1} K_5^{0.5} p_{H_2O} p_{O_2}^{0.5}\theta_v^2$$

$$\Rightarrow \theta_{OH} = \sqrt{K_2^{-1} K_4^{-1} K_5^{0.5} p_{H_2O} p_{O_2}^{0.5}\theta_v^2} = K_2^{-0.5} K_4^{-0.5} K_5^{0.25} p_{H_2O}^{0.5} p_{O_2}^{0.25}\theta_v = K_{OH} p_{H_2O}^{0.5} p_{O_2}^{0.25}\theta_v$$

$$\theta_{OH} = K_{OH} p_{O_2}^{0.25} p_{H_2O}^{0.5}\theta_v \qquad \left(K_{OH} = K_2^{-0.5} K_4^{-0.5} K_5^{0.25}\right) \qquad (A.26)$$

Then we got the expression of θ_{Cl} from *A.19*, and added it into the known expressions of θ_O, θ_{OH}.

$$K_1 = \frac{\theta_{Cl}\theta_{OH}}{p_{HCl}\theta_O\theta_v} \Rightarrow \theta_{Cl} = \frac{K_1 p_{HCl}\theta_O\theta_v}{\theta_{OH}} = \frac{K_1 p_{HCl} \cdot K_O p_{O_2}^{0.5}\theta_v \cdot \theta_v}{K_{OH} p_{H_2O}^{0.5} p_{O_2}^{0.25}\theta_v} = \frac{K_1 p_{HCl} K_O p_{O_2}^{0.25}\theta_v}{K_{OH} p_{H_2O}^{0.5}}$$

$$\Rightarrow \theta_{Cl} = K_1 K_O K_{OH}^{-1} p_{HCl} p_{O_2}^{0.25} p_{H_2O}^{-0.5}\theta_v = K_1 K_5^{0.5} K_2^{0.5} K_4^{0.5} K_5^{-0.25} p_{HCl} p_{O_2}^{0.25} p_{H_2O}^{-0.5}\theta_v$$

So we can got

$$\theta_{Cl} = K_{Cl} p_{HCl} p_{O_2}^{0.25} p_{H_2O}^{-0.5} \theta_v \qquad \left(K_{Cl} = K_1 K_2^{0.5} K_4^{0.5} K_5^{0.25} \right) \qquad (A.27)$$

We have known that the site balance exists

$$\theta_O + \theta_{OH} + \theta_{Cl} + \theta_{H_2O} + \theta_v = 1 \qquad (A.28)$$

Combining the above-mentioned expressions of the surface species, we can get

$$1 = \theta_O + \theta_{OH} + \theta_{Cl} + \theta_{H_2O} + \theta_v$$
$$= K_O p_{O_2}^{0.5} \theta_v + K_{OH} p_{O_2}^{0.25} p_{H_2O}^{0.5} \theta_v + K_{Cl} p_{HCl} p_{O_2}^{0.25} p_{H_2O}^{-0.5} \theta_v + K_{H_2O} p_{H_2O} \theta_v + \theta_v$$
$$= \left(K_O p_{O_2}^{0.5} + K_{OH} p_{O_2}^{0.25} p_{H_2O}^{0.5} + K_{Cl} p_{HCl} p_{O_2}^{0.25} p_{H_2O}^{-0.5} + K_{H_2O} p_{H_2O} + 1 \right) \theta_v$$

$$\theta_v = \left(K_O p_{O_2}^{0.5} + K_{OH} p_{O_2}^{0.25} p_{H_2O}^{0.5} + K_{Cl} p_{HCl} p_{O_2}^{0.25} p_{H_2O}^{-0.5} + K_{H_2O} p_{H_2O} + 1 \right)^{-1} \qquad (A.29)$$

For the second LHHW microkinetic model, the rate of Deacon process is

$$r = k \theta_{Cl}^2$$

Then substituting equation $A.27$ into the rate expression of this model

$$r = k \theta_{Cl}^2 = k \cdot (K_{Cl} p_{HCl} p_{O_2}^{0.25} p_{H_2O}^{-0.5} \theta_v)^2 = k K_{Cl}^2 p_{HCl}^2 p_{O_2}^{0.5} p_{H_2O}^{-1} \theta_v^2$$
$$= k (K_1 K_2^{0.5} K_4^{0.5} K_5^{0.25})^2 p_{HCl}^2 p_{O_2}^{0.5} p_{H_2O}^{-1} \theta_v^2 = k K_1^2 K_2 K_4 K_5^{0.5} p_{HCl}^2 p_{O_2}^{0.5} p_{H_2O}^{-1} \theta_v^2$$

$$r = k K_1^2 K_2 K_4 K_5^{0.5} p_{HCl}^2 p_{O_2}^{0.5} p_{H_2O}^{-1} \theta_v^2 \qquad (A.30)$$

Afterwards, if we added equation $A.29$ into the above equation $A.30$, we can get the below equation

$$r = k K_1^2 K_2 K_4 K_5^{0.5} p_{HCl}^2 p_{O_2}^{0.5} p_{H_2O}^{-1} \theta_v^2$$
$$= k K_1^2 K_2 K_4 K_5^{0.5} p_{HCl}^2 p_{O_2}^{0.5} p_{H_2O}^{-1} \left(K_O p_{O_2}^{0.5} + K_{OH} p_{O_2}^{0.25} p_{H_2O}^{0.5} + K_{Cl} p_{HCl} p_{O_2}^{0.25} p_{H_2O}^{-0.5} + K_{H_2O} p_{H_2O} + 1 \right)^{-2}$$

The simple k' to replace the pre-factor constants was used in the above equation.

Therefore, we can obtain

$$r = k'p_{HCl}^2 p_{O_2}^{0.5} p_{H_2O}^{-1} \left(K_O p_{O_2}^{0.5} + K_{OH} p_{O_2}^{0.25} p_{H_2O}^{0.5} + K_{Cl} p_{HCl} p_{O_2}^{0.25} p_{H_2O}^{-0.5} + K_{H_2O} p_{H_2O} + 1 \right)^{-2}$$

$$(k' = kK_1^2 K_2 K_4 K_5^{0.5}) \qquad (A.31)$$

Here,

$$K_O = K_5^{0.5} \qquad\qquad K_{OH} = K_2^{-0.5} K_4^{-0.5} K_5^{0.25}$$

$$K_{Cl} = K_1 K_2^{0.5} K_4^{0.5} K_5^{0.25} \qquad K_{H_2O} = K_4^{-1}$$

A.3. O$_2$-diss.＆Cl$_2$-recom. model

The third LHHW microkinetic model is O$_2$ dissociation and Cl$_2$ recombination model. In this LHHW model, both of O$_2$ dissociation and Cl$_2$ recombination processes are thought to be rate determining.[38] We named this model as O$_2$ dissociation&Cl$_2$ recombination model and noted as "O$_2$-diss.&Cl$_2$-recom. Model". Its elementary processes and the constants are shown in the below Table A.3.

Table A.3. Elementary steps in Deacon process in the 3rd LHHW model (O$_2$-diss.&Cl$_2$-recom. model).

Step	Surface Reaction	Constant
1	HCl + O* + * ⇌ Cl* + OH*	K_1
2	OH* + OH* ⇌ H$_2$O* + O*	K_2
3	Cl* + Cl* → Cl$_2$ + 2* (r.d.s)	k_3
4	H$_2$O* ⇌ H$_2$O + *	K_4
5	O$_2$ + 2* → 2O* (r.d.s.)	k_5

Some studies[4,38] point out that, whether the rate-controlled step of the Deacon process is chlorine recombination or oxygen dissociation, the reaction will be influenced by reaction conditions (e.g. partial pressure and temperature). The chlorine recombination step is the most energy demanding step, and it will poison the surface if Cl_2 cannot remove on a reasonable timescale, affecting the activity of the catalyst. The oxygen dissociation step usually needs two adjacent vacant sites, so it will be easily blocked by high surface coverages. Herein, we assumed that both of these two processes are rate-determining while other three steps are equilibrated.

According to Table A.1.3, we have

$$K_1 = \frac{k_1}{k_{-1}} = \frac{\theta_{Cl}\theta_{OH}}{p_{HCl}\theta_O\theta_v} \qquad (A.32)$$

$$K_2 = \frac{k_2}{k_{-2}} = \frac{\theta_{H_2O}\theta_O}{\theta_{OH}^2} \qquad (A.33)$$

$$K_4 = \frac{k_4}{k_{-4}} = \frac{p_{H_2O}\theta_v}{\theta_{H_2O}} \qquad (A.34)$$

In addition, there are two expressions for the reaction rate based on our assumption. According to the step (3) as the r.d.s., we can have the first one

$$r = k_3\theta_{Cl}^2 \qquad (A.35)$$

And we can get the other rate expression based on step (5) being r.d.s.

$$r = k_5 p_{O_2}\theta_v^2 \qquad (A.36)$$

From A.34, we can obtain

$$K_4 = \frac{k_4}{k_{-4}} = \frac{p_{H_2O}\theta_v}{\theta_{H_2O}} \Rightarrow \theta_{H_2O} = K_4^{-1}p_{H_2O}\theta_v$$

$$\boxed{\theta_{H_2O} = K_{H_2O}p_{H_2O}\theta_v \qquad \left(K_{H_2O} = K_4^{-1}\right) \qquad (A.37)}$$

Since *A*.35 and *A*.36 are both the expression for the rate, it can be equal to each other

$$r = k_3\theta_{Cl}^2 = k_5 p_{O_2}\theta_v^2 \Rightarrow \theta_{Cl}^2 = k_3^{-1}k_5 p_{O_2}\theta_v^2 \Rightarrow \theta_{Cl} = k_3^{-0.5}k_5^{0.5} p_{O_2}^{0.5}\theta_v$$

$$\boxed{\theta_{Cl} = K_{Cl} p_{O_2}^{0.5}\theta_v \qquad \left(K_{Cl} = k_3^{-0.5}k_5^{0.5}\right) \qquad (A.38)}$$

Next, we can get the equation below by mutipling equation *A*.32 and *A*.33,

$$K_1 = \frac{k_1}{k_{-1}} = \frac{\theta_{Cl}\theta_{OH}}{p_{HCl}\theta_O\theta_v} \qquad (A.32)$$

$$K_2 = \frac{k_2}{k_{-2}} = \frac{\theta_{H_2O}\theta_O}{\theta_{OH}^2} \qquad (A.33)$$

$$K_1 \cdot K_2 = \frac{\theta_{Cl}\theta_{OH}}{p_{HCl}\theta_O\theta_v} \cdot \frac{\theta_{H_2O}\theta_O}{\theta_{OH}^2} \Rightarrow K_1 K_2 = \frac{\theta_{Cl}\theta_{H_2O}}{p_{HCl}\theta_{OH}\theta_v}$$

So we can further get

$$\theta_{OH} = \frac{\theta_{Cl}\theta_{H_2O}}{K_1 K_2 p_{HCl}\theta_v} \qquad (A.39)$$

Next, we substituted the expressions of θ_{Cl} and θ_{H2O} into the above equation *A*.39 and can get

$$\theta_{OH} = \frac{\theta_{Cl}\theta_{H_2O}}{K_1 K_2 p_{HCl}\theta_v} = \frac{K_{Cl} p_{O_2}^{0.5}\theta_v \cdot K_{H_2O} p_{H_2O}\theta_v}{K_1 K_2 p_{HCl}\theta_v} = \frac{k_3^{-0.5}k_5^{0.5} p_{O_2}^{0.5} K_4^{-1} p_{H_2O}\theta_v}{K_1 K_2 p_{HCl}}$$

$$= K_1^{-1}K_2^{-1}k_3^{-0.5}K_4^{-1}k_5^{0.5} p_{HCl}^{-1} p_{O_2}^{0.5} p_{H_2O}\theta_v$$

$$\boxed{\theta_{OH} = K_{OH} p_{HCl}^{-1} p_{O_2}^{0.5} p_{H_2O}\theta_v \qquad \left(K_{OH} = K_1^{-1}K_2^{-1}k_3^{-0.5}K_4^{-1}k_5^{0.5}\right) \qquad (A.40)}$$

From equation *A*.32, we can get the expression of θ_O,

$$K_1 = \frac{k_1}{k_{-1}} = \frac{\theta_{Cl}\theta_{OH}}{p_{HCl}\theta_O\theta_v} \Rightarrow \theta_O = \frac{\theta_{Cl}\theta_{OH}}{K_1 p_{HCl}\theta_v}$$

Use equations *A*.38 and *A*.40 to replace θ_{Cl} and θ_{OH}, respectively.

$$\theta_O = \frac{\theta_{Cl}\theta_{OH}}{K_1 p_{HCl}\theta_v} = \frac{K_{Cl} p_{O_2}^{0.5}\theta_v \cdot K_{OH} p_{HCl}^{-1} p_{O_2}^{0.5} p_{H_2O}\theta_v}{K_1 p_{HCl}\theta_v} = K_1^{-1} K_{Cl} K_{OH} p_{HCl}^{-2} p_{O_2}^1 p_{H_2O}\theta_v$$

$$= K_1^{-1}(k_3^{-0.5} k_5^{0.5}) \cdot (K_1^{-1} K_2^{-1} k_3^{-0.5} K_4^{-1} k_5^{0.5}) p_{HCl}^{-2} p_{O_2}^1 p_{H_2O}\theta_v$$

$$= K_1^{-2} K_2^{-1} k_3^{-1} K_4^{-1} k_5 p_{HCl}^{-2} p_{O_2} p_{H_2O}\theta_v$$

$$\therefore \qquad \boxed{\theta_O = K_O p_{HCl}^{-2} p_{O_2} p_{H_2O}\theta_v \qquad \left(K_O = K_1^{-2} K_2^{-1} k_3^{-1} K_4^{-1} k_5\right) \qquad (A.41)}$$

Due to the site balance, the sum of fractional concentrations set to 1.

$$\theta_O + \theta_{OH} + \theta_{Cl} + \theta_{H_2O} + \theta_v = 1 \qquad (A.42)$$

By substituting the expressions of the concentrations of the five surface species into equation *A.42*, we can get

$$1 = \theta_O + \theta_{OH} + \theta_{Cl} + \theta_{H_2O} + \theta_v$$

$$= K_O p_{HCl}^{-2} p_{O_2} p_{H_2O}\theta_v + K_{OH} p_{HCl}^{-1} p_{O_2}^{0.5} p_{H_2O}\theta_v + K_{Cl} p_{O_2}^{0.5}\theta_v + K_{H_2O} p_{H_2O}\theta_v + \theta_v$$

$$= (K_O p_{HCl}^{-2} p_{O_2} p_{H_2O} + K_{OH} p_{HCl}^{-1} p_{O_2}^{0.5} p_{H_2O} + K_{Cl} p_{O_2}^{0.5} + K_{H_2O} p_{H_2O} + 1)\theta_v$$

$$\theta_v = (K_O p_{HCl}^{-2} p_{O_2} p_{H_2O} + K_{OH} p_{HCl}^{-1} p_{O_2}^{0.5} p_{H_2O} + K_{Cl} p_{O_2}^{0.5} + K_{H_2O} p_{H_2O} + 1)^{-1} \qquad (A.43)$$

Last, we put A.43 into A.36, we can obtain the rate of the reaction. The 3rd LHHW microkinetic model can be expressed as the follows.

$$\boxed{\begin{aligned} r &= k_5 p_{O_2}\theta_v^2 \Rightarrow \\ r &= k_5 p_{O_2}(K_O p_{HCl}^{-2} p_{O_2} p_{H_2O} + K_{OH} p_{HCl}^{-1} p_{O_2}^{0.5} p_{H_2O} + K_{Cl} p_{O_2}^{0.5} + K_{H_2O} p_{H_2O} + 1)^{-2} \qquad (A.44) \end{aligned}}$$

Here,

$$\boxed{\begin{aligned} K_O &= K_1^{-2} K_2^{-1} k_3^{-1} K_4^{-1} k_5 & K_{OH} &= K_1^{-1} K_2^{-1} k_3^{-0.5} K_4^{-1} k_5^{0.5} \\ K_{Cl} &= k_3^{-0.5} k_5^{0.5} & K_{H_2O} &= K_4^{-1} \end{aligned}}$$

B. Build ODE equations

We have obtained three LHHW microkinetic models of the Deacon process based on whether the adjacent chlorine recombination process or the dissociative oxygen adsorption process is rate controlling. Until now, there are very few experimental data values available for the Deacon process over RuO_2(110) surface, especially the exact input value of reactants and the corresponding rate of gas-phase chlorine in details. At present, we applied these values from D. Teschner et al's work[36] through the fitting to evaluate the reaction parameters (the forward constant of the r.d.s. and the equilibrium constants of other steps).

For the 1st LHHW microkinetic model, we assumed that the dissociative oxygen adsorption is the rate-determining step, affording

$$r = kp_{O_2} \left(K_O p_{HCl}^{-2} p_{Cl_2} p_{H_2O} + K_{OH} p_{HCl}^{-1} p_{Cl_2}^{0.5} p_{H_2O} + K_{Cl} p_{Cl_2}^{0.5} + K_{H_2O} p_{H_2O} + 1 \right)^{-2} \qquad (A.18)$$

$$K_O = K_1^{-2} K_2^{-1} K_3^{-1} K_4^{-1} \qquad K_{OH} = K_1^{-1} K_2^{-1} K_3^{-0.5} K_4^{-1}$$

$$K_{Cl} = K_3^{-0.5} \qquad K_{H_2O} = K_4^{-1}$$

Besides, the rate can be also expressed as the change in concentration of a substance divided by the time interval during which this change is observed. Here we mainly study our target product - chlorine gas. The rate can be written as

$$r = \frac{d[Cl_2]}{dt} \qquad (B.1)$$

We just know the initial condition is the feed of O_2 and HCl in a molecular ratio of 1:1.[36] Assuming in the ideal gas state, A is the initial partial pressure of O_2 (p_{O2}), i.e. A = p_{O2}(0). And B is the initial partial pressure of HCl [p_{HCl}(0) = B]. According to Deacon process, we have

Table B.1. Initial partial pressure of the Deacon process.

Reaction	2HCl	+	1/2O₂	↔	Cl₂	+	H₂O
Molar Ratio	2		0.5		1		1
Initial Values	A		B		0		0
Reaction Values	$2p_{Cl2}$		$0.5p_{Cl2}$		p_{Cl2}		p_{Cl2}
Final Values	$A-2p_{Cl2}$		$B-0.5p_{Cl2}$		p_{Cl2}		p_{Cl2}

Based on stoichiometry and the ideal gas law pV = nRT,

$$p_{HCl} = A - 2p_{Cl_2} \qquad p_{O_2} = B - 0.5p_{Cl_2} \qquad p_{H_2O} = p_{Cl_2} \qquad (B.2)$$

So the rate power equation can be written as

$$r = \frac{d[Cl_2]}{dt} = \frac{d\left[\frac{n_{Cl_2}}{V}\right]}{dt} = \frac{d\left[\frac{p_{Cl_2}}{RT}\right]}{dt} = \frac{d[p_{Cl_2}]}{dt} \qquad (B.3)$$

Substituting equation *B*.2 into equation *A*.18,

$$r = kp_{O_2}\left(K_O p_{HCl}^{-2} p_{Cl_2} p_{H_2O} + K_{OH} p_{HCl}^{-1} p_{Cl_2}^{0.5} p_{H_2O} + K_{Cl} p_{Cl_2}^{0.5} + K_{H_2O} p_{H_2O} + 1\right)^{-2}$$

$$= k\left(B - 0.5p_{Cl_2}\right)\left[K_O\left(A - 2p_{Cl_2}\right)^{-2} p_{Cl_2} p_{Cl_2} + K_{OH}\left(A - 2p_{Cl_2}\right)^{-1} p_{Cl_2}^{0.5} p_{Cl_2} + K_{Cl} p_{Cl_2}^{0.5} + K_{H_2O} p_{Cl_2} + 1\right]^{-2}$$

$$= k\left(B - 0.5p_{Cl_2}\right)\left[K_O\left(A - 2p_{Cl_2}\right)^{-2} p_{Cl_2}^2 + K_{OH}\left(A - 2p_{Cl_2}\right)^{-1} p_{Cl_2}^{1.5} + K_{Cl} p_{Cl_2}^{0.5} + K_{H_2O} p_{Cl_2} + 1\right]^{-2} \qquad (B.4)$$

Combining equations *B*.3 and *B*.4, we can get

$$\frac{d[p_{Cl_2}]}{dt} = k\left(B - 0.5p_{Cl_2}\right)\left[K_O\left(A - 2p_{Cl_2}\right)^{-2} p_{Cl_2}^2 + K_{OH}\left(A - 2p_{Cl_2}\right)^{-1} p_{Cl_2}^{1.5} + K_{Cl} p_{Cl_2}^{0.5} + K_{H_2O} p_{Cl_2} + 1\right]^{-2} (B.5)$$

In the above equation, the yield of Cl₂ is increased along with the reaction proceeding, i.e., p_{Cl2} is variable, and its corresponding value can be found in D. Teschner et al.'s paper.[36] Meanwhile, the initial values of reactants HCl and O₂ are fixed, which means A and B are constant values.

Assuming $p_{Cl2} = y$, the initial partial pressure of HCl and O_2 are A and B, respectively. We can get ODE for the 1st LHHW microkinetic model (O2-diss. model) as follows

$$\frac{dy}{dt} = k(B - 0.5y)\left[K_O(A-2y)^{-2}y^2 + K_{OH}(A-2y)^{-1}y^{1.5} + K_{Cl}y^{0.5} + K_{H_2O}y + 1\right]^{-2} \quad (B.6)$$

Here, the specific expression of the constant K is as follows

$$K_O = K_1^{-2}K_2^{-1}K_3^{-1}K_4^{-1} \qquad K_{OH} = K_1^{-1}K_2^{-1}K_3^{-0.5}K_4^{-1}$$
$$K_{Cl} = K_3^{-0.5} \qquad K_{H_2O} = K_4^{-1}$$

Where *k* represents the forward rate constant of the dissociative oxygen adsorption step, K_i represents the equilibrium constants of the elementary step *i* (*i* = 1, 2, 3, 4), respectively.

In the same way, we can easily get ODE for the 2nd LHHW microkinetic model (Cl2-recom. model) from equation *A.31*.

$$r = k'p_{HCl}^2 p_{O_2}^{0.5} p_{H_2O}^{-1}\left(K_O p_{O_2}^{0.5} + K_{OH}p_{O_2}^{0.25}p_{H_2O}^{0.5} + K_{Cl}p_{HCl}p_{O_2}^{0.25}p_{H_2O}^{-0.5} + K_{H_2O}p_{H_2O} + 1\right)^{-2}$$
$$(k' = kK_1^2 K_2 K_4 K_5^{0.5}) \qquad (A.1.31)$$
$$\Rightarrow r = \frac{dp_{Cl_2}}{dt} = k'p_{HCl}^2 p_{O_2}^{0.5} p_{H_2O}^{-1}\left(K_O p_{O_2}^{0.5} + K_{OH}p_{O_2}^{0.25}p_{H_2O}^{0.5} + K_{Cl}p_{HCl}p_{O_2}^{0.25}p_{H_2O}^{-0.5} + K_{H_2O}p_{H_2O} + 1\right)^{-2}$$

By assuming $p_{Cl2} = y$ and putting equation *B.2* into the above equation, we can get

$$\frac{dp_{Cl_2}}{dt} = \frac{k'(A - 2p_{Cl_2})^2(B - 0.5p_{Cl_2})^{0.5}p_{Cl_2}^{-1}}{\left[K_O(B - 0.5p_{Cl_2})^{0.5} + K_{OH}(B - 0.5p_{Cl_2})^{0.25}p_{Cl_2}^{0.5} + K_{Cl}(A - 2p_{Cl_2})(B - 0.5p_{Cl_2})^{0.25}p_{Cl_2}^{-0.5} + K_{H_2O}p_{Cl_2} + 1\right]^2}$$

Finally, we obtained

$$\frac{dy}{dt} = \frac{k'(A - 2y)^2(B - 0.5y)^{0.5}}{y\left[K_O(B - 0.5y)^{0.5} + K_{OH}(B - 0.5y)^{0.25}y^{0.5} + K_{Cl}(A - 2y)(B - 0.5y)^{0.25}y^{-0.5} + K_{H_2O}y + 1\right]^2} \quad (B.7)$$

In the above equation (B.7)

$$k' = kK_1^2 K_2 K_4 K_5^{0.5} \qquad K_O = K_5^{0.5} \qquad K_{H_2O} = K_4^{-1}$$

$$K_{OH} = K_2^{-0.5} K_4^{-0.5} K_5^{0.25} \qquad K_{Cl} = K_1 K_2^{0.5} K_4^{0.5} K_5^{0.25}$$

Where k denotes the forward rate constant of the adjacent chlorine recombination step, K_i denotes the equilibrium constants of the elementary step i (i = 1, 2, 4, 5), respectively.

And for the 3rd LHHW microkinetic model (O_2-diss.&Cl_2-recom. model), we can also easily get the corresponding ODE in accordance with the equation A.44.

$$r = k_5 p_{O_2} (K_O p_{HCl}^{-2} p_{O_2} p_{H_2O} + K_{OH} p_{HCl}^{-1} p_{O_2}^{0.5} p_{H_2O} + K_{Cl} p_{O_2}^{0.5} + K_{H_2O} p_{H_2O} + 1)^{-2} \qquad (A.44)$$

Combining the equations B.2 and B.3, the above equation can be changed to

$$\frac{dp_{Cl_2}}{dt} = \frac{k_5(B - 0.5 p_{Cl_2})}{\left[K_O(A - 2p_{Cl_2})^{-2}(B - 0.5p_{Cl_2})p_{Cl_2} + K_{OH}(A - 2p_{Cl_2})^{-1}(B - 0.5p_{Cl_2})^{0.5}p_{Cl_2} + K_{Cl}(B - 0.5p_{Cl_2})^{0.5} + K_{H_2O}p_{Cl_2} + 1\right]^2}$$

$$\frac{dy}{dt} = \frac{k_5(B - 0.5y)}{\left[K_O(A - 2y)^{-2}(B - 0.5y)y + K_{OH}(A - 2y)^{-1}(B - 0.5y)^{0.5}y + K_{Cl}(B - 0.5y)^{0.5} + K_{H_2O}y + 1\right]^2} \qquad (B.8)$$

The constants in above equation B.8 specifically refer to the following

$$K_O = K_1^{-2} K_2^{-1} k_3^{-1} K_4^{-1} k_5 \qquad K_{OH} = K_1^{-1} K_2^{-1} k_3^{-0.5} K_4^{-1} k_5^{0.5}$$

$$K_{Cl} = k_3^{-0.5} k_5^{0.5} \qquad K_{H_2O} = K_4^{-1}$$

Where k_3 and k_5 represent the forward rate constant of the chlorine recombination step and the oxygen dissociation step, respectively. K_i represents the equilibrium constants of the elementary step i (i = 1, 2, 4), respectively.

From the experimental data,[36] we know that the initial conditions are as follows: the initial partial pressure of HCl is 0.521 bar, and according to stoichiometry the initial partial pressure of O_2 is 0.130 bar. Furthermore, the equilibrium constant or rate constant contained in the equations set to be parameters in the ODE, e.g. *k(i)*, *i* = 1, 2, 3, 4, 5.

So firstly, the ODE for the O_2-diss. model can be written as below

$$\frac{dy}{dt} = k(0.130 - 0.5y)\left[K_O(0.521 - 2y)^{-2}y^2 + K_{OH}(0.521 - 2y)^{-1}y^{1.5} + K_{Cl}y^{0.5} + K_{H_2O}y + 1\right]^{-2} \qquad (B.9)$$

Then, using *k(i)* to denote the above equilibrium constant or forward reaction rate constant in equation B.9, it can be obtained

$$\frac{dy}{dt} = k(1)(0.130 - 0.5y)\left[k(2)(0.521 - 2y)^{-2}y^2 + k(3)(0.521 - 2y)^{-1}y^{1.5} + k(4)y^{0.5} + k(5)y + 1\right]^{-2} \qquad (B.10)$$

Where

$$k(1) = k \qquad k(2) = K_O \qquad k(3) = K_{OH}$$
$$k(4) = K_{Cl} \qquad k(5) = K_{H_2O}$$

Secondly, for the Cl_2-recom. model, we can get the ODE by the same way.

$$\frac{dy}{dt} = \frac{k'(0.521 - 2y)^2(0.130 - 0.5y)^{0.5}}{y\left[K_O(0.130 - 0.5y)^{0.5} + K_{OH}(0.130 - 0.5y)^{0.25}y^{0.5} + K_{Cl}(0.521 - 2y)(0.130 - 0.5y)^{0.25}y^{-0.5} + K_{H_2O}y + 1\right]^2} \qquad (B.11)$$

Similarly, we used the parameters *k(i)* (*i* = 1,2,3,4,5) to exchange the equilibrium constant or the forward rate constant in the above equation *B*.11.

$$\frac{dy}{dt} = \frac{k(1)(0.521 - 2y)^2(0.130 - 0.5y)^{0.5}}{y\left[k(2)(0.130 - 0.5y)^{0.5} + k(3)(0.130 - 0.5y)^{0.25}y^{0.5} + k(4)(0.521 - 2y)(0.130 - 0.5y)^{0.25}y^{-0.5} + k(5)y + 1\right]^2} \qquad (B.12)$$

Where

$$k(1) = k' \qquad k(2) = K_O \qquad k(3) = K_{OH}$$
$$k(4) = K_{Cl} \qquad k(5) = K_{H_2O}$$

Last, we also got the ODE for the O_2-diss.&Cl_2-recom. Model as follows

$$\frac{dy}{dt} = \frac{k(1)(0.130 - 0.5y)}{\left[k(2)(0.521 - 2y)^{-2}(0.130 - 0.5y)y + k(3)(0.521 - 2y)^{-1}(0.130 - 0.5y)^{0.5}y + k(4)(0.130 - 0.5y)^{0.5} + k(5)y + 1\right]^2} \qquad (B.13)$$

Where

$$k(1)=k_5 \qquad k(2)=K_O \qquad k(3)=K_{OH}$$
$$k(4)=K_{Cl} \qquad k(5)=K_{H_2O}$$

C. ODE in the wide-range prediction

Surface coverages (θ) of the reaction species in the LHHW microkinetic model were calculated based on the reaction mechanism summarized in Table 3.1 using the rate equations below. k_i and k_{-i} denote the corresponding intrinsic rates for the forward and backward reactions, respectively, as enumerated in Table 3.2. Here, we did not distinguish for br and cus site coverages separately. θ_i stands for the fraction of the species sites (i = Cl, O, H_2O, OH, and vacant site *), calculated by normalizing the total coverages of the five species sites to 1.

Taking O_2-diss. Model for example, the equations of the surface coverages and total rate of Cl_2 are as follows:

(1) Coverage of the empty site *

$$d\theta_*/dt = [1+(k_1^2 k_2 k_3 k_4)^{-1} p_{HCl}(t)^{-2} p_{Cl_2}(t) p_{H_2O}(t) + (k_1 k_2 k_3^{0.5} k_4)^{-1} p_{HCl}(t)^{-1}$$
$$p_{Cl_2}(t)^{0.5} p_{H_2O}(t) + k_3^{-0.5} p_{Cl_2}(t)^{0.5} + k_4^{-1} p_{H_2O}(t)]^{-1} \qquad (C.1)$$

(2) Coverage of the oxygen O

$$d\theta_O / dt = k_1^{-2} k_2^{-1} k_3^{-1} k_4^{-1} p_{HCl}(t)^{-2} p_{Cl_2}(t) p_{H_2O}(t)(d\theta_* / dt) \qquad (C.2)$$

(3) Coverage of hydroxide OH

$$d\theta_{OH} / dt = k_1^{-1} k_2^{-1} k_3^{-0.5} k_4^{-1} p_{HCl}(t)^{-1} p_{Cl_2}(t)^{0.5} p_{H_2O}(t)(d\theta_* / dt) \qquad (C.3)$$

(4) Coverage of chlorine Cl

$$d\theta_{Cl} / dt = k_3^{-0.5} p_{Cl_2}(t)^{0.5}(d\theta_* / dt) \qquad (C.4)$$

(5) Coverage of water H_2O

$$d\theta_{H_2O} / dt = k_4^{-1} p_{H_2O}(t)(d\theta_* / dt) \qquad (C.5)$$

(6) Total rate of chlorine (Cl_2)

$$dp_{Cl_2} / dt = k_5 p_{O_2}(t)(d\theta_* / dt)^2 \qquad (C.6)$$

List of publications

[1] Sotoodeh, F.; **Yao, Z.**; Reuter, K. From Macro to Micro: Kinetics of HCl Oxidation (Deacon Process) on RuO_2 Catalyst. *Manuscript in preparation.*

[2] **Yao, Z.**; Reuter, K. First-Principles Computational Screening of Dopants to Improve the Deacon Process over RuO_2. *CatChemCat.* **2018**, *10*, 465-469.

References

[1]   www.eurochlor.org.

[2]   Perez-Ramirez, J.; Mondelli, C.; Schmidt, T.; Schluter, O. F. K.; Wolf, A.; Mleczko, L.; Dreier, T. Sustainable Chlorine Recycling Via Catalysed HCl Oxidation: From Fundamentals to Implementation. *Energy. Environ. Sci.* **2011**, *4*, 4786-4799.

[3]   Pan, H. Y.; Minet, R. G.; Benson, S. W.; Tsotsis, T. T. Process for Converting Hydrogen Chloride to Chlorine. *Ind. Eng. Chem. Res.* **1994**, *33*, 2996-3003.

[4]   López, N.; Gómez-Segura, J.; Marín, R. P.; Pérez-Ramírez, J. Mechanism of HCl Oxidation (Deacon Process) Over RuO_2. *J. Catal.* **2008**, *255*, 29-39.

[5]   Motupally, S.; Mah, D. T.; Freire, F. J.; Weidner, J. W. Recycling Chlorine from Hydrogen Chloride. *Electrochem. Soc. Interface* **1998**, *7*, 32-36.

[6]   www.chlorineinstitute.org .

[7]   Hine, F.; Nozaki, M.; Kurata, Y. Bench Scale Experiment of Recovery of Chlorine from Waste Gas. *J. Electrochem. Soc.* **1984**, *131*, 2834.

[8]   Johnson, J.; Winnick, J. Electrochemical Membrane Separation of Chlorine from Gaseous Hydrogen Chloride Waste. *Sep. Purif. Technol.* **1999**, *15*, 223-229.

[9]   Mohammadi, F.; Ashrafizadeh, S. N.; Sattari, A. Aqueous HCl Electrolysis Utilizing a Reducing Cathode. *Chem. Eng. J.* **2009**, *155*, 757-762.

[10]   Versar, i. In *A Survey of Potential Chlorine Production Processes;* Springfield: VA, **1979**.

[11]   Sconce, J. S. In *Chlorine, Its Manufacture, Properties and Uses;* Reinhold Pub. Corp.: New York, **1962**, pp 901.

[12]   Deacon, H. U.S. Patent 165,802, **1875**.

[13]   Wattimena, F.; Sachtler, W. M. H. Catalyst Research for the Shell Chlorine Process. **1981**, *7*, 816-827.

[14]   Itoh, H.; Kono, Y.; Ajioka, M.; Takenaka, S.; Kataita, M. U.S. Patent 4,803,065, **1989**.

[15]   Amrute, A. P.; Mondelli, C.; Hevia, M. A. G.; Perez-Ramirez, J. Mechanism-Performance Relationships of Metal Oxides in Catalyzed HCl Oxidation. *ACS Catal.* **2011**, *1*, 583-590.

[16]   Wolf, A.; Mleczko, L.; Schluter, O. F.; Schubert, S. U.S. patent 0274897, **2007**.

[17]   Abekawa, H.; Ito, Y.; Hibi, T. U.S. Patent 5,908,607, **1999**.

[18]   Deacon, H. U.S. Patent 85,370, **1868**.

[19]   Deacon, H. U.S. Patent 118,209, **1871**.

[10]   Deacon, H. U.S. Patent 141,333, **1875**.

[21]   Cherniavsky, A. J.; Johnson, A. J. U.S. Patent 2,542,961, **1951**.

[22]   Engel, W. F.; Wattimena, F. U.S. Patent 3,210,158, **1965**.

[23]   Mortensen, M.; Minet, R. G.; Tsotsis, T. T.; Benson, S. W. The development of a dual fluidized-bed reactor system for the conversion of hydrogen chloride to chlorine. *Chem. Eng. Sci.* **1999**, *54*, 2131-2139.

[24]   Kiyoura, T.; Kogure, Y.; Nagayama, T.; Kanaya, K. U.S. Patent 4,822,589, **1989**.

[25]   Seki, K. Development of RuO_2/Rutile-TiO_2 Catalyst for Industrial HCl Oxidation Process. *Catal. Surv. Asia* **2010**, *14*, 168-175.

[26]   Hibi, T.; Nishida, H.; Abekawa, H. U.S. Patent 5,871,707, **1999**.

[27]   Wolf, A.; Kintrup, J.; Schluter, O. F.; Mleczko, L. U.S. patent 0292336, **2007**.

[28]   Wolf, A.; Mleczko, L.; Schubert, S.; Schluter, O. F. U.S. patent 0274901, **2007**.

[29]   Over, H. Atomic-Scale Understanding of the HCl Oxidation Over RuO_2, A Novel Deacon Process. *J. Phys. Chem. C* **2012**, *116*, 6779-6792.

[30]   Moussallem, I.; Jörissen, J.; Kunz, U.; Pinnow, S.; Turek, T. Chlor-alkali Electrolysis with Oxygen Depolarized Cathodes: History, Present Status and Future Prospects. *J. Appl. Electrochem.* **2008**, *38*, 1177-1194.

[31]   Weber, R.; Kintrup, J.; Bulan, A.; Kamper, F. U.S. patent 0029404, **2008**.

[32]   Sumitomo Chemical Co., Ltd. The Development of Improved Hydrogen Chloride Oxidation Process. *Sumitomo Kagaku* **2004**, *I*, 1-11.

[33]   Seitsonen, A. P.; Over, H. Oxidation of HCl Over TiO_2-Supported RuO_2: A Density Functional Theory Study. *J. Phys. Chem. C* **2010**, *114*, 22624-22629.

[34]   Crihan, D.; Knapp, M.; Zweidinger, S.; Lundgren, E.; Weststrate, C. J.; Andersen, J. N.; Seitsonen, A. P.; Over, H. Stable Deacon Process for HCl Oxidation Over RuO_2. *Angew. Chem. Int. Ed.* **2008**, *47*, 2131-2134.

[35]   Zweidinger, S.; Crihan, D.; Knapp, M.; Hofmann, J. P.; Seitsonen, A. P.; Weststrate, C. J.; Lundgren, E.; Andersen, J. N.; Over, H. Reaction Mechanism of the Oxidation of HCl Over RuO_2(110). *J. Phys. Chem. C* **2008**, *112*, 9966-9969.

[36]   Teschner, D.; Farra, R.; Yao, L.; Schlögl, R.; Soerijanto, H.; Schomäcker, R.; Schmidt, T.; Szentmiklósi, L.; Amrute, A. P.; Mondelli, C.; Pérez-Ramírez, J.; Novell-Leruth, G.; López, N. An Integrated Approach to Deacon Chemistry on RuO_2-Based Catalysts. *J. Catal.* **2012**, *285*, 273-284.

[37]   Hess, F.; Krause, P. P. T.; Rohrlack, S. F.; Hofmann, J. P.; Farkas, A.; Over, H. One-Dimensional Confinement in Heterogeneous Catalysis: Trapped Oxygen on RuO_2(110) Model Catalysts. *Surf. Sci.* **2012**, *606*, L69-L73.

[38]   Studt, F.; Abild-Pedersen, F.; Hansen, H. A.; Man, I. C.; Rossmeisl, J.; Bligaard, T. Volcano Relation for the Deacon Process Over Transition-Metal Oxides. *ChemCatChem* **2010**, *2*, 98-102.

[39]   Fernandez, E. M.; Moses, P. G.; Toftelund, A.; Hansen, H. A.; Martinez, J. I.; Abild-Pedersen, F.; Kleis, J.; Hinnemann, B.; Abild-Pedersen, F.; Bligaard, T.; Nørskov, J. K. Scaling Relationships for Adsorption Energies on Transition Metal Oxide, Sulfide, and Nitride Surfaces. *Angew. Chem. Int. Ed.* **2008**, *47*, 4683-4686.

[40]   Hagemeyer, A.; Trübenbach, P.; Rieker, C. W.; Wünsch, M.; Watzernberger, O. EP Patent 0761594-A1, **1997**.

[41]   Wolf, A.; Mleczko, L.; Schlüter, O. F.; Schubert, S. WO Patent 2010133313-A1, **2010**.

[42]   Lee, G.; Lee, S. W.; Sohn, I.; Kwon, Y. C.; Song, J.; Son, C.-S. WO Patent 2009035234-A2, **2009**.

[43]   Amrute, A. P.; Mondelli, C.; Moser, M.; Novell-Leruth, G.; López, N.; Rosenthal, D.; Farra, R.; Schuster, M. E.; Teschner, D.; Schmidt, T.; Pérez-Ramírez, J. Performance, Structure, and Mechanism of CeO_2 in HCl Oxidation to Cl_2. *J. Catal.* **2012**, *286*, 287-297.

[44] Hohenberg, P.; Kohn, W. Inhomogeneous Electron Gas. *Phys. Rev. B* **1964**, *136*, 864-871.

[45] Kohn, W.; Sham, L. J. Self-Consistent Equations Including Exchange and Correlation Effects. *Phys. Rev. A* **1965**, *140*, 1133-1138.

[46] Schrödinger, E. An Undulatory Theory of the Mechanics of Atoms and Molecules. *Phys. Rev.* **1926**, *28*, 1049-1070.

[47] Becke, A. D. Perspective: Fifty Years of Density-Functional Theory in Chemical Physics. *J. Chem. Phys.* **2014**, *140*, 18A301.

[48] Perdew, J. P.; Burke, K.; Ernzerhof, M. Generalized Gradient Approximation Made Simple. *Phys. Rev. Lett.* **1996**, *77*, 3865-3868.

[49] Hammer, B.; Hansen, L. B.; Nørskov, J. K. Improved Adsorption Energetics within Density-Functional Theory using Revised Perdew-Burke-Ernzerhof Functionals. *Phys. Rev. B* **1999**, *59*, 7413-7421.

[50] Laidler, K. J. *Theories of Chemical Reaction Rates.* New York: McGraw-Hill, **1969**.

[51] Laidler, K. J.; King, M. C. Development of Transition-State Theory. *J. Phys. Chem.* **1983**, *87*, 2657-2664.

[52] Laidler, K. J.; King, M. C, A Lifetime of Transition-State Theory. *The Chemical Intelligencer* **1998**, *4*, 39.

[53] Jónsson, H.; Mills, G.; Jacobsen, K. W. Nudged Elastic Band Method for Finding Minimum Energy Paths of Transitions, in *Classical and Quantum Dynamics in Condensed Phase Simulations.* Ed. Berne, B. J.; Ciccotti G.; Coker, D. F. World Scientific, pp 385, **1998**.

[54] Mills, G.; Jónsson, H. Quantum and Thermal Effects in H_2 Dissociative Adsorption: Evaluation of Free Energy Barriers in Multidimensional Quantum Systems. *Phys. Rev. Lett.* **1994**, *72*, 1124.

[55]   Mills, G.; Jónsson, H.; Schenter, G. K. Reversible Work Transition State Theory: Application to Dissociative Adsorption of Hydrogen. *Surf. Sci.* **1995**, *324*, 305-337.

[56]   Henkelman, G.; Jóhannesson, G.; Jónsson. H. Methods for Finding Saddle Points and Minimum Energy Paths, in *Theoretical Methods in Condensed Phase Chemistry*, Kluwer Academic Publishers, pp 269-302, **2000**.

[57]   Henkelman, G.; Jónsson, H. Improved Tangent Estimate in the Nudged Elastic Band Method for Finding Minimum Energy Paths and Saddle Points. *J. Chem. Phys.* **2000**, *113*, 9978-9985.

[58]   Baker, J. An Algorithm for the Location of Transition States. *J. Comp. Chem.* **1986**, *7*, 385-395.

[59]   Halgren, T. A.; Lipscomb, W. N. The Synchronous-Transit Method for Determining Reaction Pathways and Locating Molecular Transition States. *Chem. Phys. Lett.* **1977**, *49*, 225-232.

[60]   Govind, N.; Petersen, M.; Fitzgerald, G.; King-Smith, D.; Andzelm, J. A Generalized Synchronous Transit Method for Transition State Location. *Comput. Mater. Sci.* **2003**, *28*, 250-258.

[61]   Salciccioli, M.; Stamatakis, M.; Caratzoulas, S.; Vlachos, D. G. A Review of Multiscale Modeling of Metal-Catalyzed Reactions: Mechanism Development for Complexity and Emergent Behavior. *Chem. Eng. Sci.* **2011**, *66*, 4319-4355.

[62]   Ertl, G. *Reactions at Solid Surfaces*, John Wiley & Sons, **2010**.

[63]   Zweidinger, S.; Hofmann, J. P.; Balmes, O.; Lundgren, E.; Over, H. In situ Studies of the Oxidation of HCl over RuO_2 Model Catalysts: Stability and Reactivity. *J. Catal.* **2010**, *272*, 169-175.

[64]   Chorkendorff, I.; Niemantsverdriet, J. W. *Concepts of Modern Catalysis and Kinetics.* Wiley-VCH, **2007**.

[65]   Reuter, K.; Scheffler, M. First-Principles Kinetic Monte Carlo Simulations for Heterogeneous Catalysis: Application to the CO Oxidation at RuO$_2$(110). *Phys. Rev. B* **2006**, *73*, 045433.

[66]   Reuter, K.; Frenkel, D.; Scheffler, M. The Steady State of Heterogeneous Catalysis, Studied by First-Principles Statistical Mechanics. *Phys. Rev. Lett.* **2004**, *93*, 116105.

[67]   Temel, B.; Meskine, H.; Reuter, K.; Scheffler, M.; Metiu, H. Does Phenomenological Kinetics Provide an Adequate Description of Heterogeneous Catalytic Reactions? *J. Chem. Phys.* **2007**, *126*, 204711.

[68]   Clark, S. J.; Segall, M. D.; Pickard, C. J.; Hasnip, P. J.; Probert, M. I. J.; Refson, K.; Payne, M. C. First Principles Methods using CASTEP. *Z. Kristallogr. Cryst. Mater.* **2005**, *220*, 567-570.

[69]   Vanderbilt, D. Soft Self-Consistent Pseudopotentials in a Generalized Eigenvalue Formalism. *Phys. Rev. B* **1990**, *41*, 7892-7895.

[70]   Knapp, M.; Crihan, D.; Seitsonen, A. P.; Lundgren, E.; Resta, A.; Andersen, J. N.; Over, H. Complex Interaction of Hydrogen with the RuO$_2$(110) Surface. *J. Phys. Chem. C* **2007**, *111*, 5363-5373.

[71]   Kim, Y. D.; Seitsonen, A. P.; Wendt, S.; Wang, J.; Fan, C.; Jacobi, K.; Over, H.; Ertl, G. Characterization of Various Oxygen Species on an Oxide Surface: RuO$_2$(110). *J. Phys. Chem. B* **2001**, *105*, 3752-3758.

[72]   Hess, F.; Over, H. Rate-Determining Step or Rate-Determining Configuration? The Deacon Reaction over RuO$_2$(110) Studied by DFT-Based KMC Simulations. *ACS Catal.* **2017**, *7*, 128-138.

[73]   Lobo, A.; Conrad, H. Interaction of H$_2$O with the RuO$_2$(110) Surface Studied by HREELS and TDS. *Surf. Sci.* **2003**, *523*, 279-286.

[74]   Matera, S.; Meskine, H.; Reuter, K. Adlayer Inhomogeneity without Lateral Interactions: Rationalizing Correlation Effects in CO Oxidation at RuO$_2$(110) with First-Principles Kinetic Monte Carlo. *J. Chem. Phys.* **2011**, *134*, 064713.

[75]   Over, H.; Schomäcker, R. What Makes a Good Catalyst for the Deacon Process? *ACS Catal.* **2013**, *3*, 1034-1046.

[76]   Man, I. C.; Su, H.-Y.; Calle-Vallejo, F.; Hansen, H. A.; Martinez, J. I.; Inoglu, N. G.; Kitchin, J.; Jaramillo, T. F.; Nørskov, J. K.; Rossmeisl, J. Universality in Oxygen Evolution Electrocatalysis on Oxide Surfaces. *ChemCatChem* **2011**, *3*, 1159-1165.

[77]   González-Huerta, R. G.; Ramos-Sánchez, G.; Balbuena, P. B. Oxygen Evolution in Co-Doped RuO_2 and IrO_2: Experimental and Theoretical Insights to Diminish Electrolysis Overpotential. *J. Power Sources* **2014**, *268*, 69-76.

[78]   Macounová, K.; Makarova, M.; Franc, J.; Jirkovský, J.; Krtil, P. Influence of Oxygen on Reactivity of $Ru_{1-x}Fe_xO_{2-y}$-Doped Materials. *Electrochem. Solid ST.* **2008**, *11*, F27-F29.

[79]   Macounová, K.; Makarova, M.; Jirkovský, J.; Franc, J.; Krtil, P. Parallel Oxygen and Chlorine Evolution on $Ru_{1-x}Ni_xO_{2-y}$ Nanostructured Electrodes. *Electrochimi. Acta.* **2008**, *53*, 6126-6134.

[80]   Petrykin, V.; Macounova, K.; Franc, J.; Shlyakhtin, O.; Klementova, M.; Mukerjee, S.; Krtil, P. Zn-Doped RuO_2 Electrocatalyts for Selective Oxygen Evolution: Relationship between Local Structure and Electrocatalytic Behavior in Chloride Containing Media. *Chem. Mater.* **2011**, *23*, 200-207.

[81]   Zhuiykov, S. Morphology of Pt-Doped Nanofabricated RuO_2 Sensing Electrodes and Their Properties in Water Quality Monitoring Sensors. *Sensor Actuat B-Chem.* **2009**, *136*, 248-256.

[82]   White, J. A.; Bird, D. M. Implementation of Gradient-Corrected Exchange-Correlation Potentials in Car-Parrinello Total-Energy Calculations. *Phys. Rev. B* **1994**, *50*, 4954-4957.

[83]   Perdew, J. P.; Ruzsinszky, A.; Csonka, G.; Vydrov, O.; Scuseria, G.; Constantin, L.; Zhou, X.; Burke, K. Restoring the Density-Gradient Expansion for Exchange in Solids and Surfaces. *Phys. Rev. Lett.* **2008**, *100*, 136406.

[84]   Wang, T.; Jelic, J.; Rosenthal, D.; Reuter, K. Exploring Pretreatment-Morphology Relationships: Ab Initio Wulff Construction for RuO_2 Nanoparticles under Oxidising Conditions. *ChemCatChem* **2013**, *5*, 3398-3403.

[85]   García-Mota, M.; Vojvodic, A.; Metiu, H.; Man, I. C.; Su, H.-Y.; Rossmeisl, J.; Nørskov, J. K. Tailoring the Activity for Oxygen Evolution Electrocatalysis on Rutile TiO_2(110) by Transition-Metal Substitution. *ChemCatChem* **2011**, *3*, 1607-1611.

[86] Rogal, J.; Reuter, K. Ab Initio Atomistic Thermodynamics for Surfaces: A Primer. Max-Planck-Gesellschaft Zur Foerderung Der Wissenschaften e.V. Berlin (Germany FR) Fritz-Haber-Inst, **2006**.

[87] Stull, D. R.; Prophet, H. *JANAF Thermochemical Tables*, 2nd Ed., U.S. National Bureau of Standards (U.S. EPO, Washington, D.C., **1971**).

[88] Li, W. X.; Stampfl, C.; Scheffler, M. Insights into the Function of Silver as an Oxidation Catalyst by Ab Initio Atomistic Thermodynamics. *Phys. Rev. B* **2003**, *68*, 165412.

[89] Reuter, K.; Scheffler, M. Oxide Formation at the Surface of Late 4D Transition Metals: Insights from First-Principles Atomistic Thermodynamics. *Appl. Phys. A* **2004**, *78*, 793-798.

[90] Reuter, K.; Scheffler, M. Composition, Structure, and Stability of RuO_2(110) as a Function of Oxygen Pressure. *Phys. Rev. B* **2002**, *65*, 035406.

[91] Rogal, J.; Reuter, K.; Scheffler, M. Thermodynamic stability of PdO surfaces. *Phys. Rev. B* **2004**, *69*, 075421.

[92] Li, W. X.; Stampfl, C.; Scheffler, M. Why is a Noble Metal Catalytically Active? The Role of the O-Ag Interaction in the Function of Silver as an Oxidation Catalyst. *Phys. Rev. Lett.* **2003**, *90*, 256102.

[93] Wyckoff, R. W. G. *Crystal Structures*. Wiley, New York, **1964**.

[94] Wells, A. F. *Structural Inorganic Chemistry*, 5th Ed. Clarendon, Oxford, **1984**.

[95] Reuter, K.; Scheffler, M. First-Principles Atomistic Thermodynamics for Oxidation Catalysis: Surface Phase Diagrams and Catalytically Interesting Regions. *Phys. Rev. Lett.* **2003**, *90*, 046103; Composition and Structure of the RuO_2(110) Surface in an O_2 and CO Environment: Implications for the Catalytic Formation of CO_2. *Phys. Rev. B* **2003**, *68*, 045407.

[96] Reuter, K.; Plaisance, C. P.; Oberhofer, H.; Andersen, M. J. Perspective: On the Active Site Model in Computational Catalyst Screening. *J. Chem. Phys.* **2017**, *146*, 040901.

[97] Ponomareva, A. V.; Isaev, E. I.; Skorodumova, N. V.; Vekilov, Y. K.; Abrikosov, I. A. Surface Segregation Energy in bcc Fe-rich Fe-Cr Alloys. *Phys. Rev. B* **2007**, *75*, 245406.

[98]   Hugosson, H. W.; Eriksson, O.; Jansson, U.; Abrikosov, I. A. Surface Segregation of Transition Metal Impurities on the TiC(100) Surface. *Surf. Sci.* **2005**, *585*, 101-107.

[99]   Hrovat, M.; Holc, J.; Samardzija, Z.; Drazic, G. The Extent of Solid Solubility in the RuO_2-TiO_2 system. *J. Mater. Res.* **1996**, *11*, 727-732.

[100]   Jacob, K. T.; Subramanian, R. Phase Diagram for the System RuO_2-TiO_2 in Air. *J. Phase Equilib. Diffus.* **2008**, *29*, 136-140.

[101]   Erhart, P.; Klein, A.; Albe, K. First-Principles Study of the Structure and Stability of Oxygen Defects in Zinc Oxide. *Phys. Rev. B* **2005**, *72*, 085213.

[102]   Doll, K.; Harrison, N. M. Theoretical Study of Chlorine Adsorption on the Ag(111) Surface. *Phys. Rev. B* **2001**, *63*, 165410.

[103]   Jaffe, J. E.; Lin, Z.; Hess, A. C. Gaussian-Basis LDA and GGA Calculations for Alkali-Metal Equations of State. *Phys. Rev. B* **1998**, *57*, 11834.

[104]   Soon, A.; Todorova, M.; Delley, B.; Stampfl, C. Oxygen Adsorption and Stability of Surface Oxides on Cu(111): A First-Principles Investigation. *Phys. Rev. B* **2006**, *73*, 165424.

[105]   Stampfl, C.; Scheffler, M. Theoretical Study of O Adlayers on Ru(0001). *Phys. Rev. B* **1996**, *54*, 2868.

[106]   Mondelli, C.; Amrute, A. P.; Krumeich, F.; Schmidt, T.; Pérez-Ramírez, J. Shaped RuO_2/SnO_2–Al_2O_3 Catalyst for Large-Scale Stable Cl_2 Production by HCl Oxidation. *ChemCatChem* **2011**, *3*, 657-660.

[107]   Amrute, A. P.; Krumeich, F.; Mondelli, C.; Pérez-Ramírez, J. Depleted Uranium Catalysts for Chlorine Production. *Chem. Sci.* **2013**, *4*, 2209-2217.

[108]   CRC Handbook of Chemistry and Physics, edited by R. C. Weast (CRC Press, Cleveland, OH, **1974**), 55th ed.

[109]   de Leeuw, N. H.; Purton, J. A. Density-Functional Theory Calculations of the Interaction of Protons and Water with Low-Coordinated Surface Sites of Calcium Oxide. *Phys. Rev. B* **2001**, *63*, 195417.

[110]   Oba, F.; Togo, A.; Tanaka, I.; Paier, J.; Kresse, G. Defect Energetics in ZnO: A Hybrid Hartree-Fock Density Functional Study. *Phys. Rev. B* **2008**, *77*, 245202.

[111] Zhuravlev, Y. N.; Obolonskaya, O. S. Structure, Mechanical Stability, and Chemical Bond in Alkali Metal Oxides. *J. Struct. Chem.* **2010**, *51*, 1005-1013.

[112] Ziegler, M.; Rosenfeld, M.; Känzig, W.; Fischer, P. Strukturuntersuchungen an Alkalihyperoxiden. *Helv. Phys. Acta* **1976**, *49*, 57-90.

[113] Brese, N. E.; O'keeffe, M.; Ramakrishna, B. L.; Vondreele, R. B. Low-Temperature Structures of CuO and AgO and Their Relationships to those of MgO and PdO. *J. Solid State Chem.* **1990**, *89*, 184-190.

[114] Sun, S.; Li, C.; Zhang, D.; Wang, Y. Density Functional Theory Study of the Adsorption and Dissociation of O_2 on CuO(111) Surface. *Appl. Surf. Sci.* **2015**, *333*, 229-234.

[115] Kim, Y. D.; Seitsonen, A. P.; Over, H. Adsorption Characteristics of CO and N_2 on RuO_2(110). *Phys. Rev B* **2001**, *63*, 115419.

[116] Jauho, T. S.; Olsen, T.; Bligaard, T.; Thygesen, K. S. Improved Description of Metal Oxide Stability: Beyond the Random Phase Approximation with Renormalized Kernels. *Phys. Rev. B* **2015**, *92*, 115140.

[117] Raebiger, H.; Lany, S.; Zunger, A. Origins of the *p*-Type Nature and Cation Deficiency in Cu_2O and Related Materials. *Phys. Rev. B* **2007**, *76*, 045209.

[118] Hisham, M. W. M.; Benson, S. W. Thermochemistry of the Deacon Process. *J. Phys. Chem.* **1995**, *99*, 6194-6198.

[119] Allen, J. A. Energetic Criteria for Oxychlorination Catalysts. *J. Appl. Chem (London)* **1962**, *12*, 406-412.

[120] Andersen, M.; Medford, A. J.; Nørskov, J. K.; Reuter, K. Analyzing the Case for Bifunctional Catalysis. *Angew. Chem. Int. Ed.* **2016**, *55*, 5210-5214.

[121] Andersen, M.; Medford, A. J.; Nørskov, J. K.; Reuter, K. Scaling-Relation-Based Analysis of Bifunctional Catalysis: The Case for Homogeneous Bimetallic Alloys. *ACS Catal.* **2017**, *7*, 3960-3967.

[122] Reuter, K. Ab Initio Thermodynamics and First-Principles Microkinetics for Surface Catalysis. *Catal. Lett.* **2016**, *146*, 541-563.

[123] Hofmann, J. P.; Zweidinger, S.; Knapp, M.; Seitsonen, A. P.; Schulte, K.; Andersen, J. N.; Lundgren, E.; Over, H. Hydrogen-Promoted Chlorination of RuO_2(110). *J. Phys. Chem. C* **2010**, *114*, 10901-10909.

[124] Yao, Z.; Reuter, K. First-Principles Computational Screening of Dopants to Improve the Deacon Process over RuO_2. *CatChemCat.* **2018**, *10*, 465-469.

[125] Sabbe, M. K.; Reyniers, M. F.; Reuter, K. First-Principles Kinetic Modeling in Heterogeneous Catalysis: An Industrial Perspective on Best-Practice, Gaps and Needs. *Catal. Sci. Technol.* **2012**, *2*, 2010-2024.

[126] Santen, R. A. v.; Neurock, M. Concepts in Theoretical Heterogeneous Catalytic Reactivity. *Catal. Rev. Sci. Eng.* **1995**, *37*, 557-698.

[127] Reuter, K. *Modeling and Simulation of Heterogeneous Catalytic Reactions* (Ed.: O. Deutschmann), Wiley-VCH Verlag GmbH & Co. KGaA, **2011**, pp. 71-111.

[128] Wang, J.; Fan, C. Y.; Sun, Q.; Reuter, K.; Jacobi, K.; Scheffler, M.; Ertl, G. Surface Coordination Chemistry: Dihydrogen versus Hydride Complexes on RuO_2(110)* *Angew. Chem. Int. Ed.* **2003**, *42*, 2151-2154.

[129] Over, H. Surface Chemistry of Ruthenium Dioxide in Heterogeneous Catalysis and Electrocatalysis: From Fundamental to Applied Research. *Chem. Rev.* **2012**, *112*, 3356-3426.

[130] Sun, Q.; Reuter, R.; Scheffler, M. Effect of A Humid Environment on the Surface Structure of RuO_2(110). *Physical Review B* **2003**, *67*, 205424.

[131] Jónsson, H.; Mills, G.; Jacobsen, K. *Classical and Quantum Dynamics in Condensed Phase Simulations*. World Scientific, **1998**, pp. 385-404.

[132] Sun, Q.; Reuter, R.; Scheffler, M. Hydrogen Adsorption on RuO_2(110): Density-Functional Calculations. *Physical Review B* **2004**, *70*, 235402.

[133] Sotoodeh, F.; Yao, Z.; Reuter, K. From Macro to Micro: Kinetics of HCl Oxidation (Deacon Process) on RuO_2 Catalyst. *Unpublished result.*

[134] Rohrlack, S. *HCl-Oxidation über RuO$_2$-Modellkatalysatoren*. Ph.D. thesis, Justus-Liebig-
       Universität, Gießen, **2012**.

Acronyms

BZ	Brillouin zone
CER	chlorine evolution reaction
CG	conjugate gradient
DFT	density functional theory
GGA	generalized gradient approximation
HCl	hydrogen chloride
HER	hydrogen evolution reaction
H-K	Hohenberg-Kohn
HRCLS	high-resolution core level shift
HTST	harmonic transition state theory
kMC	kinetic Monte Carlo
KS-DFT	Kohn-Sham density functional theory
LDA	local density approximation
LEED	low-energy electron diffraction
LHHW	Langmuir-Hinshelwood-Hougen-Watson
LST	linear synchronous transit
MEP	minimum energy path
ML	monolayer
NEB	nudged elastic band
ODC	oxygen-depolarized cathodes
ODE	ordinary differential equation
OER	oxygen evolution reaction

PW	plane-wave
PBE	Perdew-Burke-Ernzerhof
PES	potential energy surface
QST	quadratic synchronous transit
r.d.s.	rate-determining step
RPBE	revised Perdew-Burke-Ernzerhof
TEM	transmission electron microscopy
TST	transition state theory
XC	exchange-correlation

Acknowledgement

In this special summer, I am so excited and proud to finish my doctoral thesis in the Institute of Theoretical Chemistry at the Technical University of Munich, as one of the most memorable stage and unforgettable memories in my life. At this point, I would like to thank all the people that supported and helped me along the whole way of my Ph.D. study.

First and foremost, I would like to express my great gratitude to my doctoral supervisor Prof. Karsten Reuter who offered me a great opportunity to study in this wonderful group. I am very inspired and impressed by Karsten, by his enthusiasm for chemistry, his sharing of great ideas, his kindness to help others, and his hard-working attitude. He always patiently and thoroughly answers all of my questions even if he is quite busy. I really benefit a lot from his guidance, advice and constant support. I would like to express my sincere gratitude to him, and I feel very fortunate to work under his guidance.

I would like to express my appreciation to my direct supervisors, Dr. Farnaz Sotoodeh, and Dr. Mie Andersen, who has been involved in discussions and guidance during my Ph.D. studies. Both of them always provide a lot of professional theoretical and technical support and help me. A special thank goes to Dr. Farnaz Sotoodeh who is my first direct supervisor at the beginning of my Ph.D. She gave me the first helpful guidance for my project. In addition, when it comes to CASTEP issues, I am highly indebted to Dr. Harald Oberhofer, Dr. Juan Manuel Lorenzi, Simon P. Rittmeyer, and Simone Köcher, from whom I enjoyed the intense scientific discussions and received lots of useful suggestions and ideas about the specific details or problems which encountered in the course of my study.

Furthermore, I want to particularly thank my office mates (CH62108) Dr. Juan Manuel Lorenzi and Dr. Stefan Ringe for making a very comfortable office time. They create a harmonious and nice atmosphere for our research work. Thanks to them for helping me solve many IT problems, and in particular, they always help me to install the software and check the program bugs. Besides, they usually give me a lot of good

suggestions and warm encouragements for my project and daily life.

Thanks go to the whole Reuter group. I am so glad that I have the precious opportunity to work together with all of the group members for several years. We shared many great experiences and happiness in many group exercises, such as academic conferences, short-term workshops, international evening dinners, sailings, Oktoberfests, group outing dinners, and so on. The lovely group traditions let me go through my whole Ph.D. life with lots of delicious cakes, which let me feel so warm and moved. All of these communications greatly broaden my scope in science and deepen our friendship with each other. Thanks in particular go to the IT-team around Christoph Scheurer for the huge effort they are spending to keep our computer infrastructure running as stable as it is.

A very big and special thank goes to my family, especially to my boyfriend, for their constant encouragement and infinite patience to support me through all difficult times.